Bio-based matrix photocatalysts for photodegradation of antibiotics

Nidia Maldonado-Carmona, Giusi Piccirillo, Jérémy Godard, Karine Heuzé, Emilie Genin, Nicolas Villandier, Mário Calvete, Stéphanie Leroy-Lhez

Bio-based matrix photocatalysts for photodegradation of antibiotics

Nidia Maldonado-Carmona[1] · Giusi Piccirillo[2] · Jérémy Godard[4] · Karine Heuzé[3] · Emilie Genin[3] · Nicolas Villandier[4] · Mário J. F. Calvete[2] · Stéphanie Leroy-Lhez[4]

Abstract

Antibiotics development during the last century permitted unprecedent medical advances. However, it is undeniable that there has been an abuse and misuse of antimicrobials in medicine and cosmetics, food production and food processing, in the last decades. The pay toll for human development and consumism is the emergence of extended antimicrobial resist-ance and omnipresent contamination of the biosphere. The One Health concept recognizes the interconnection of human, environmental and animal health, being impossible alter one without affecting the others. In this context, antibiotic decon-tamination from water-sources is of upmost importance, with new and more efficient strategies needed. In this framework, light-driven antibiotic degradation has gained interest in the last few years, strongly relying in semiconductor photocatalysts. To improve the semiconductor properties (i.e., efficiency, recovery, bandgap width, dispersibility, wavelength excitation, etc.), bio-based supporting material as photocatalysts matrices have been thoroughly studied, exploring synergetic effects as operating parameters that could improve the photodegradation of antibiotics. The present work describes some of the most relevant advances of the last 5 years on photodegradation of antibiotics and other antimicrobial molecules. It presents the conjugation of semiconductor photocatalysts to different organic scaffolds (biochar and biopolymers), then to describe hybrid systems based on g-C_3N_4 and finally addressing the emerging use of organic photocatalysts. These systems were developed for the degradation of several antibiotics and antimicrobials, and tested under different conditions, which are analyzed and thoroughly discussed along the work.

Graphical abstract

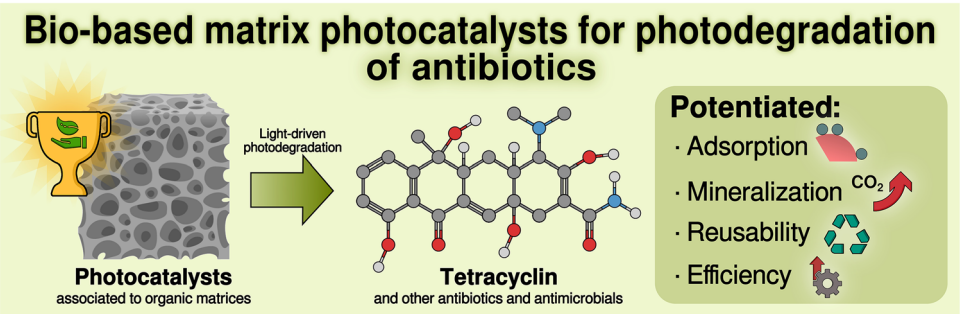

1 Introduction

Modern medicine has undoubtedly reached its golden age thanks to antibiotics development. However, if the benefits for controlling infectious diseases by antibiotics has always been considered to be more important than their toxicity, our societies are facing antibiotics' presence in the environment due to the abuse/misuse of antibiotics in human medicine as their overuse in food production for animal farming [1, 2]. This is even more problematic that it is also linked to the development of resistant bacteria against the actual available antibiotics [3, 4] concomitantly with damage of the health beneficial bacteria [5–8]. It has been estimated that about 30% of antibiotics prescribed to people are not necessary, implying, at the end, their over release into the environment. This data is clearly evidenced in the 2013 WHO

report, which states that 80% of total antibiotic consumption was attributed to veterinary use, in a total consumption of 200,000 tons/year [9]. Estimations state that, if no further actions are taken, by 2050, ten million people will yearly die worldwide due to infectious diseases caused by multi resistant bacteria [10]. Therefore, current political and scientific efforts are poured into (i) improving the use and decreasing the misuse of clinical antimicrobials, (ii) find new antimicrobial treatments, with less proneness to develop resistance, and (iii) limit the spread of antimicrobial molecules in the natural environment. The latest is of primordial importance, as antimicrobial resistance is likely to be selected from microbial communities in contact with residual antibiotics, as is the case of the emergence of colistin resistance in poultry farms [11]. Many techniques, such as membrane processes adsorption, electrochemical, and photodegradation, are already employed to remove antibiotics from water and active research is currently pursue in these domains [12]. In this framework, the advanced oxidation processes (AOP), initially relying on toxic and expensive oxidation systems, sometimes combined with metal semiconductor catalysts and largely used to eliminate general pollutants [2], are now investigated for antibiotic degradation [1]. However, effective degradation of antibiotics through photocatalysis often involves the use of composite catalysts in slurry form [13], as suspension [14] or as powered catalysts [15] that are difficult to remove from natural environment, and thus may generate a secondary pollution which significantly limits their use on a practical scale. In addition, a limitation of light absorption by the photocatalyst can also sometimes occur and decrease the photoinduced reactions efficiency, this being due to a shielding effect of the matrix [16, 17]. If composite photocatalysts are still a current research hotspot, to overcome those limitations, some researchers have suggested immobilizing photocatalytic nanoparticles (NPs) on biopolymers to create membranes or hydrogels that retain photoactive, antibacterial, and adsorbent properties.

Therefore, in line with a previous review on this hot topic [1], we focus here on the recent literature dealing with the use of a bio-based supporting material for heterogeneous photocatalysts in the removal of antimicrobials (Fig. 1) from water through AOP. To outline the plus value of those bio-based matrix and to judge the efficiency of any pharmaceuticals' photodegradation process, several parameters/factors must be analyzed. Those involving the utilization of bio-based supports, such as biochar, biopolymers (alginate, chitosan, cellulose, lignin) among others, include their post-synthetic physicochemical characteristics (e.g., preparation conditions, surface areas/volumes, hydrophobicity/hydrophilicity) and adsorption capability, besides other factors more related to the irradiation process (e.g., photocatalyst carrier generation/recombination and light intensity/range), or even concerning the degradation operational features, including drug/catalyst concentration, pH/temperature, degradation time and catalyst stability. These parametric analyses can be translated into degradation efficiency, reaction rate, mechanistic elucidation, catalyst reusability, drug mineralisability, and toxicity of degradation products to the environment and humans.

This review will analyze those parameters in the following sections with an entry by type of supporting materials used. Also, a focus on all organic systems (both supporting material and photosensitizer that will photodegrade antibiotics) have been done in the last part. The authors also encourage the reader that are interested in the description of the principles of heterogeneous photochemical mechanisms that implies AOP to refer to Calvete et al. [1].

This review will analyze the relevant parameters in the following sections, with entries by type of supporting materials used as matrices (biochar, alginate, chitosan, cellulose and other biopolymers extracted from plants). In addition, a section dedicated to fully organic systems (both supporting material and photosensitizer in antibiotics photodegradation) is presented in the last part. This review was not intended to focus on mechanistic aspects, as these have well covered in recent years [18–21]. The authors encourage the readers, who are interested in the description of the heterogeneous photochemical mechanistic principles involved in AOP, to read these reviews in addition.

2 Hybrid systems based on biochar matrix

Biochar is a carbon-enriched biomaterial that is produced from the thermochemical conversion of biomass, usually from waste origin. Its name derives from of biomass. Biochar is the lightweight black residue, made of carbon and ashes, being a form of charcoal. Its conversion can take place either in an oxygen-free environment (pyrolysis) or in presence of it (calcination). The physical and chemical properties of biochar, as determined by the feedstock, are broadly categorized in several respects, including proximate and elemental composition, pH, and porosity. The atomic ratios of biochar, including O/C and H/C, are correlated with properties relevant to organic content, e.g., polarity and aromaticity [22].

2.1 Catalyst preparation

As mentioned in introduction, several parameters must be considered and analysed to evaluate the photodegradation efficiency in a process. In particular, when biochar is used as a support or component in a photocatalytic composite, its preparation can actually influence the photocatalytic properties. Without giving synthetic details, which can be found in specific literature [23], the strategies for the preparation of

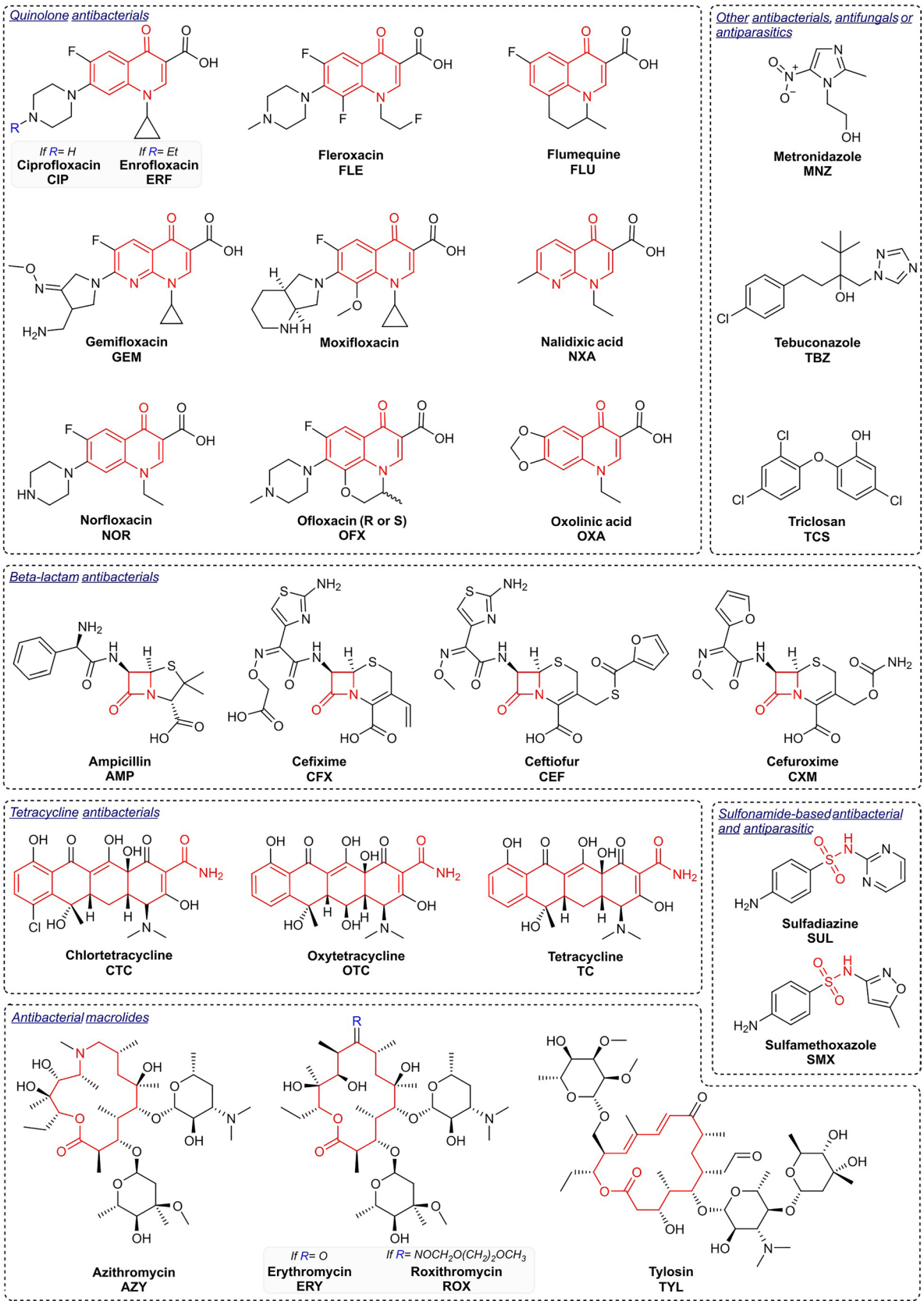

Fig. 1 Antimicrobials described in the present review, organized alphabetically and by structure family

carbonaceous biochar materials herein discussed is divided into pyrolysis, which is a decomposition in the absence of oxygen at high temperature [24–35]; calcination, which occurs usually in presence of air, at high temperature [35–43]; or even hydrothermal carbonization (HTC), which is a chemical process that promotes an aqueous carbonization at elevated temperature and pressure to yield structured carbon materials [44–46]. Reports studying the effect of these synthetic parameters are also scarce. Table 1 shows selected examples of biochar-based photocatalysts, summarizing some features regarding the preparation methodology, and its influence in the photocatalysis process.

Prior pyrolysis of biomass raw materials is preferred by most authors who chose this method, usually under temperatures between 450 and 700 °C [25] (entry 1, Table 1 and others, not shown in the table [24, 26, 28–30, 32, 34]). Other groups chose to increase the pyrolysis temperature, reporting the preparation of biochar (SC), by pyrolysis of spent coffee grounds at 1000 °C for 2 h (entry 2, Table 1) [27]. It has been suggested that raising the pyrolysis temperature of the biochar results in an increase in the surface area of the biochar while decreasing the amount of oxygen-containing functional groups on its surface [23]. This would theoretically imply a decrease in the adsorption capacity toward organic molecules such as antibiotics, but this property is not linearly applicable regarding photocatalyst efficiency (discussed below). A differing example is the work by Zhang, who prepared biochar (BC) by pyrolysis of *Brassica napa* polen at 350 °C for 2 h (entry 3, Table 1) [31]. This is considered a low temperature for biochar pyrolysis, but the photocatalyst prepared from it could still perform well.

Instead of using pyrolysis as synthetic method, other authors [37] synthesized photocatalyst TiO_2/AC(PSB), the biochar material (AC(PSB) being prepared by calcination of pistachio shell biowaste at 450 °C for 3 h prior to mechanical mixing with TiO_2 (entry 6, Table 1). This catalyst managed to degrade **ofloxacin** (**OFX**) in 82% after just 50 min irradiation, which suggests that calcination is a similarly effective synthetic method, when compared with pyrolysis.

To avoid speculative claims, and since the source of the biochar material is also important for its properties, it is advisable to study the effect of carbonization temperature on the synthesis optimization of biochar-based catalysts and consequently, on its activity toward the degradation of antibiotics, studied under the exact same conditions. This was delivered, for example, by Gonçalves [47], who prepared photocatalysts ZnO/SM and ZnO/SB (*Salvinia molesta* = SM and sugarcane bagasse = SB) in two steps, first by directly mixing the biomass (SM and SB) with ZnO precursor through precipitation method, and then performing the pyrolysis of the blended hybrid materials at mild temperatures of 350 °C and 450 °C (entry 4, Table 1). The authors concluded that the biomass origin was of negligible relevance, as the catalysts prepared thereof showed similar **sulfamethoxazole** (**SMX**) degradation rates, under UV-A irradiation (a 125 W high-pressure mercury vapor lamp (without protective bulb), being inserted into the solution by means of a glass bulb). On the other hand, raising the pyrolysis temperature has a positive effect on the degradation of **SMX** (pH 4, initial concentration of **SMX** being 5 mg L^{-1} in the presence of 0.1 g of composite), as 80% **SMX** was degraded after 45 min irradiation using both catalysts, prepared by pyrolysis at 350 °C, while 98% **SMX** degradation was achieved when using the catalysts prepared by pyrolysis at 450 °C (Fig. 2).

In an analogous study, Alfred [40] reported photocatalysts TiO_2/ZPS and TiO_2/ZPP, by mixing Na_2WO_4 with biomass from *Carica papaya* seeds (ZPS) and *Musa paradisiaca* peels (ZPP) and TiO_2 precursor through hydrothermal method followed by calcination of the blended hybrids at 350 °C and 500 °C. In this case, the materials prepared from *C. papaya* seeds (ZPS) showed similar performance when compared to the previous study, for both calcination temperatures (entry 7, Table 1). On the other hand, calcination at 500 °C was more influential on the degradation of **ampicillin** (**AMP**) (95% degradation) against 90% degradation for the material calcinated at 350 °C. For the photocatalysts prepared at the two different temperatures, this influence was nullified for the degradation of **SMX**, which reached 65% in both cases, which may suggest that, as expected, other factors such as the structure of the antibiotics, may play a role in the degradation process.

A different study was carried out by Li and collaborators [44], who synthesized photocatalyst TiO_2/Aloe, by mixing TiO_2 precursor and aloe vera biomass at room temperature, followed by either an hydrothermal reaction at 180 °C for 3 h or calcination at 500 °C for 3 h. A marked difference was obtained for the degradation of **ciprofloxacin** (**CIP**), with 90% degradation of **CIP** after 60 min (TiO_2/Aloe prepared by hydrothermal method) versus 50% degradation of **CIP** after 60 min (TiO_2/Aloe prepared by calcination) (entry 8, Table 1).

In another research group, Li [35] performed a thorough study for the synthetic optimization of the photocatalyst designated as S–C, which stands for sulfur-doped carbon, a material prepared by carbonization of lignosulfonate with subsequent sulphur doping. Among several parameters, the temperature of carbonization (entry 5, Table 1) and the type of carbonization (calcination in air or pyrolysis in N_2 atmosphere) were investigated for **TC** degradation under visible-light irradiation. Thus, the authors prepared the catalyst by pyrolysis for 12 h, at 270, 300, 330, 400 and 500 °C and concluded that the most suitable temperature was 300 °C, since the corresponding material provided the best **TC** degradation rate (81% degradation) after 300 min irradiation (Fig. 3a). When the type of carbonization was compared,

Table 1 Selected examples of the preparation of biochar-based photocatalysts, and their relation with degradation efficiency

Entry/references	Catalyst	Biochar preparation	Catalyst efficiency
1/[25]	TiO_2/pBC	pBC prepared by pyrolysis of reed straw at 500 °C for 6 h; HCl treatment	91% deg. **SMX** in deionized water; 66% in Yellow River water (both after 3 h)
2/[27]	Ag-TiO_2/SC	SC prepared by pyrolysis of spent coffee grounds at 1000 °C for 2 h; NaOH and AcOH treatment	99% **TC** deg. after 40 min and 96% NOR deg. after 50 min
3/[31]	Cu_2O/BC	BC prepared by pyrolysis of rapeseed polen at 350 °C for 2 h; H_2SO_4 treatment	85% **TC** deg. after 120 min
4/[47]	ZnO/SM and ZnO/SB	Pyrolysis of blended hybrid materials at 350 °C and 450 °C (salvinia molesta = SM and sugarcane bagasse = SB); NaOH treatment	98% **SMX** deg. after 45 min using ZnO/SB and ZnO/SM (pyrolysis at 450 °C)
			80% **SMX** deg. after 45 min using ZnO/SB and ZnO/SM (pyrolysis at 350 °C)
5/[35]	S doped Carbon (S–C–X–Y)	Calcination (in air) or pyrolysis (in N_2); Duration: 6, 12 or 24 h; Temperature: 270, 300, 330, 400 and 500 °C; no treatment	81% **TC** deg. after 300 min, with S-C-N2-12 (best material)
		X = air or N_2 (calcination or pyrolysis)	
		Y = duration of calcination/pyrolysis, in hours	
6/[37]	TiO_2/AC(PSB)	AC(PSB) prepared by calcination of pistachio shell biowaste at 450 °C for 3 h; KOH treatment	82% **OFX** deg. of in 50 min
7/[40]	TiO_2/ZPS and TiO_2/ZPP	Calcination of blended hybrids 350 °C and 500 °C (*Carica papaya* seeds = ZPS and *Musa paradisiaca* peels = ZPP); $ZnCl_2$/$NaWO_4$ treatment	> 95% deg. for **AMP**; 65% for **SMX**, in 60 min with TiO_2/ZPS (carbonized at 500 °C)
			90% deg. for **AMP**; 65% for **SMX**, in 60 min with TiO_2/ZPS (carbonized at 350 °C)
8/[44]	TiO_2/Aloe	Blended hybrids—Hydrothermal reaction at 180 °C for 3 h or calcination at 500 °C for 3 h; no treatment	90% deg. of **CIP** after 60 min (hydrothermal)
		Aloe = aloe vera biomass	50% deg. of **CIP** after 60 min (calcination)

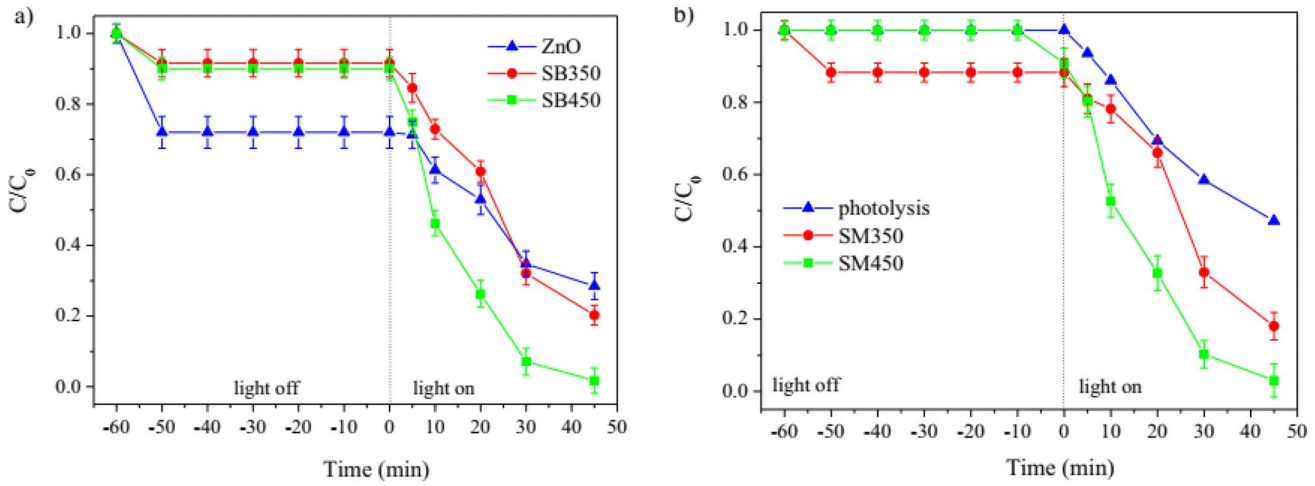

Fig. 2 **SMX** removal promoted by the composites produced using **a** SB-based catalyst, **b** SM-based catalyst (pH = 4; [**SMX**] = 5 mg L^{-1} in the presence of 0.1 g of composite; UV-A irradiation with a 125 W high-pressure mercury vapor lamp). Reproduced with permission from reference [47]

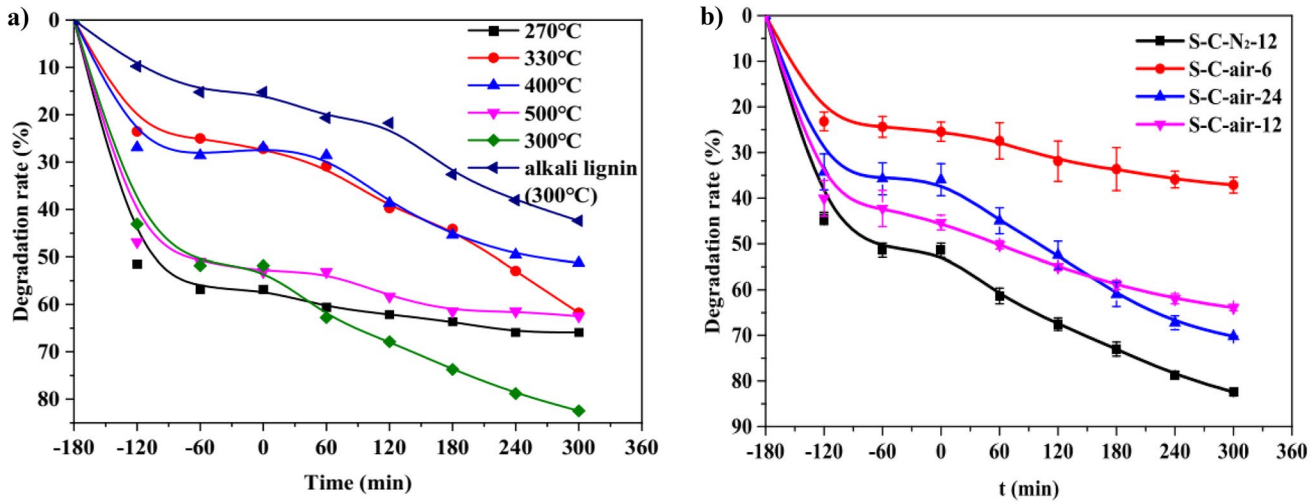

Fig. 3 **a** Degradation efficiency of tetracycline with different S–C catalysts, prepared by pyrolysis on N_2 at different temperatures; **b** Degradation process of **TC** over S–C catalysts, prepared by carbonization (air) and pyrolysis (N_2) at different reaction times (6, 12 and 24 h). Reproduced with permission from reference [35]

results showed that pyrolysis (at 300 °C) gave the best catalysts, while duration of the pyrolysis reaction was found optimal for a reaction time of 12 h (Fig. 3b).

A direct correlation between the temperature, the heating rate, the duration of pyrolysis/calcination and the efficiency of biochar as component of a photocatalyst could not be found within the works herein reviewed. Although carbonization is an important parameter in the preparation of a biochar-based photocatalyst, its sole consideration is not decisive, as it must be seen in combination with other parameters, such as the temperature of carbonization used to prepare the semiconducting metal oxides, which is suggested to be in the range of 400–600 °C to maximize its photocatalytic activity [48]. Furthermore, the ratios between biochar and the semiconducting sensitizers need optimization on a study-by-study basis when using binary or ternary hybrid photocatalysts as the biochar properties are not linear regarding its weight presence in the hybrid materials. For example, Alghamdi [37] prepared TiO_2/AC(PSB) from pistachio shell-derived biochar with several wt% of AC(PSB) (2.5, 5, 7.5, 10 wt%) on TiO_2. The authors preliminary concluded, through diffuse reflectance spectroscopy experiments, that the photocatalyst having 10 wt% of AC(PSB) on TiO_2 was the most suitable to proceed **OFX** photodegradation studies,

based on its lowest bandgap energy. In another example, Isa [41] prepared photocatalyst ZnO/P, where P stands for pullulan-based biochar. The authors introduced a Zn^{2+}:P molar ratio variation of 1:0, 4:1, 5:1 and 6:1, where the zinc concentration was varied from 0.17, 0.68, 0.85 and 1.02 M respectively. The photocatalyst having a 4:1 Zn^{2+}:P molar ratio presented the highest surface area (20 cm^2 g^{-1}) and one of the highest pore volumes (0.04 cm^3 g^{-1}). Preliminary photodegradation studies corroborated these predicates showing better degradation percentages and rates, reason why it was selected to pursue the study on the photodegradation of **amoxicillin** (**AMX**). Yahia [42] reported the synthesis of CuO/AC, where the activated carbon (AC) biochar was based on chemically activated Jujube nuts. The semiconductor was impregnated onto the activated carbon material in 10, 15 and 20% wt%. **AMX**-photodegradation experiments were carried out and the photocatalyst sample with 15 wt% CuO/AC behaved marginally better than the other samples reaching 93% removal/degradation, against ~ 80% for the other photocatalysts. In another work, $BiVO_4$/AC was prepared by Wang [45] by mixing fixed amounts (0.01 g, 0.05 g, 0.1 g and 0.2 g) of the activated carbon material (sodium lignosulfonate) to 1 mmol of $BIVO_4$ precursor during the hybrid catalysts preparation. The material incorporating 0.1 g AC showed the best performance, reaching 65% degradation of **oxytetracycline hydrochloride** (**OTC**). Photocatalyst $BiFeO_3$/BC, in which the biochar support (BC) was prepared from oil palm empty fruit bunches and integrated with $BiFeO_3$ by sol–gel method, was synthesized in $BiFeO_3$:BC 1:0.5, 1:1 and 1:2 w/w ratios [33]. The authors observed that the increase in biochar composition from 0.5 to 1.0 showed an increase in **CIP** removal efficiency from 67 to 72%. However, for the 1:2 composite, the removal efficiency of **CIP** decreased slightly to 71%. The authors also observed that the adsorption contribution was nearly 25% for all catalysts, which was ascribed to capacity of the biochar in adsorbing **CIP** without irradiation, while $BiFeO_3$ had little ability to adsorb **CIP** without light and synergized better when exposed to visible light. Lastly, the ternary hybrid catalyst WO_3/BiOCl/GSC, where the graphene-like sand composite biochar (GSC) was prepared from sucrose, was synthesized by varying the WO_3/BiOCl ratio, but keeping the GSC amount constant [43]. Samples containing 20, 40, 60 and 80 wt% of BiOCl and WO_3 were then mixed with a fixed amount of GSC. The photocatalytic degradation of **AMP** and **OTC** was tested and the 60% WO_3/BiOCl/GSC performed better than the other catalysts, reaching nearly 60% **AMP** and **OTC** degradation efficiencies.

A parameter that may affect the properties of activated biochar is the activation strategy used to prepare the biochar from biomass. Several activation techniques are used to prepare efficient biochar catalysts. Broadly, activation techniques for biochar modification are classified into two categories: (i) physical and (ii) chemical. In physical activation, porosity and surface area of biochar is increased by exposing it to the flow of gas agents, including CO_2, steam or mixtures at above 700 ◦C. Chemical activation involves the addition of activators, including bases (NaOH, KOH, etc.), acids (HCl, H_2SO_4, H_3PO_4, etc.) or oxidants (e.g., H_2O_2) during the course of carbonization (in situ) or added to pre formed biochar [49]. The vast majority of biochar-based catalyst here discussed use chemical activation techniques, namely using bases or acids (see Table 1). However, no comparisons were made by authors correlating the activation technique with the catalysts' efficiency, other than the fact that, usually, base activation favors adsorption of negatively charged molecules while acids favor the adsorption of negatively charged molecules.

2.2 Adsorption role in efficiency

In an antibiotics photodegradation process, adsorption of the substrates onto/into the surface of the photocatalyst may also occur and play a role in contaminant removal/degradation [20]. Determining whether adsorption and/or photocatalysis are the dominant factors in the removal/degradation of the pollutant without/with light irradiation is necessary to understand the remediation pathway of the contaminant drug. Adsorption interactions between organic contaminants and the biochar-based photocatalytic materials can occur via: (i) partitioning to the non-carbonized area (semiconductor surface); (ii) electrostatic attraction (cationic and anionic); (iii) surface precipitation and (iv) biochar physical adsorption, usually favored by the presence of e.g., carbonyl, carboxyl, hydroxyl and amine functional groups [50–52]. Also, the physicochemical characteristics of the photocatalysts, highly depend on the biochar surface chemical properties, its area and volume. It should be noted that adsorption occurs prior to light irradiation. The photocatalyst adsorption capacity can only influence the proximity of the pollutant to the catalysts surface, implying that the catalytic efficiency could benefit from the highest proximity. Nevertheless, it is commonly assumed that photodegradation is the main pathway for antibiotic removal, since light irradiation always takes place.

Table 2 shows selected examples of biochar-based photocatalysts, summarizing some features regarding the role of adsorption in the catalytic efficiency, especially the q_m (maximum adsorption capacity, expressed in mg g^{-1}) and q_e (amount of contaminant adsorbed per unit mass of adsorbent at equilibrium, in mg g^{-1}) values, which demonstrate the maximum adsorption capacity and the effective amount of contaminant adsorbed to the material, as the Langmuir constant (K_L) which indicates the extent of interaction between the adsorbate and the surface.

Table 2 Selected examples of the application of biochar-based photocatalysts, relating some structural physical properties with degradation efficiency

Entry/references	Catalyst	Catalyst surface areas (S_{area})/volumes (P_{vol})	Calculated adsorption parameters[a]	Efficiency
1/[24]	TiO_2/BC	$S_{area} = 383\ m^2\ g^{-1}$ (TiO_2/BC) $S_{area} = 134\ m^2\ g^{-1}$ (BC)	$q_m = 2.4\ mg\ g^{-1}$ $K_L = 0.63\ L\ mg^{-1}$ $q_e = 0.6 - 2.4\ mg\ g^{-1}$ **SMX**	($[\mathbf{SMX}]_i = 10\ mg\ L^{-1}$) 91% deg. SMX after 6 h
2/[25]	TiO_2/pBC	$S_{area} = 102\ m^2\ g^{-1}$ (TiO_2/pBC) $S_{area} = 221\ m^2\ g^{-1}$ (pBC)	$q_m = 6.6\ mg\ g^{-1}$ $K_L = 0.04\ L\ mg^{-1}$	($[\mathbf{SMX}]_i = 10\ mg\ L^{-1}$) 91% deg. **SMX** in deionized water; 66% in Yellow River water (both after 3 h)
3/[26]	Zn-TiO_2/pBC	$S_{area} = 69\ m^2\ g^{-1}$ (Zn-TiO_2/pBC) $S_{area} = 221\ m^2\ g^{-1}$ (pBC)	$q_m = 8.0\ mg\ g^{-1}$ $K_L = 0.10\ L\ mg^{-1}$	($[\mathbf{SMX}]_i = 10\ mg\ L^{-1}$) 81% deg. **SMX** in deionized water; 54% in Yellow River water (both after 3 h)
4/[36]	N,S-TiO_2/ASB	NR	NR	($[\mathbf{CIP}]_i = 30\ mg\ L^{-1}$) 86% deg. **CIP** after 2.5 h 45% adsorption after 45 min
5/[38]	TiO_2/TCT	$S_{area} = 102\ m^2\ g^{-1}$; $P_{vol} = 0.23\ cm^3\ g^{-1}$ (TiO_2/TCT)	NR	($[\mathbf{TC}\ HCl]_i = 10\ mg\ L^{-1}$) 99% deg. **TC** HCl after 0.5 h 40–55% adsorption after 60 min
6/[42]	CuO/AC	NR	$K_L = 0.02\ L\ mg^{-1}$	98% deg. **SMX** after 1.5 h 50% adsorption after 1 h
7/[43]	WO_3/BiOCl/GSC	NR	$q_e = 63\ mg\ g^{-1}$ **AMP** $q_e = 64\ mg\ g^{-1}$ **OTC**	99% deg. **AMP** 80% deg. **OTC** (both after 8 h) 40% adsorption for both antibiotics, after 2 h
8/[34]	I/WSP and I/OSR	$S_{area} = 37\ m^2\ g^{-1}$; $P_{vol} = 0.03\ cm^3\ g^{-1}$ (I/WSP) $S_{area} = 29\ m^2\ g^{-1}$; $P_{vol} = 0.02\ cm^3\ g^{-1}$ (I/OSR) $S_{area} = 3\ m^2\ g^{-1}$ (WSP) $S_{area} = 4\ m^2\ g^{-1}$ (OSR)	$q_e = 16\ mg\ g^{-1}$ for I/WSP and $q_e = 22\ mg\ g^{-1}$ for I/OSR	78% deg. **TC** after 2 h (both catalysts) 32% adsorption for I/WSP; 42% adsorption for I/OSR
9/[39]	TiO_2/PFB	$S_{area} = 64\ m^2\ g^{-1}$ (TiO_2/PFB) $S_{area} = 261\ m^2\ g^{-1}$ (PFB)	$q_e = 103\ mg\ g^{-1}$ **AMX**	($[\mathbf{AMX}]_i = 20\ mg\ L^{-1}$) 99% deg. **AMX** after 20 h 84% adsorption after 4 h

[a] q_m is the maximum adsorption capacity ($mg\ g^{-1}$), K_L is the Langmuir constant ($L\ mg^{-1}$) and q_e is the amount of contaminant adsorbed per unit mass of adsorbent at equilibrium ($mg\ g^{-1}$)

For example, Xie research group calculated q_m and K_L parameters in their studies [25, 26], allowing to compare two related photocatalysts, TiO_2/pBC and Zn-TiO_2/pBC, which differed in the presence of Zn in the constitution of the latter catalyst. Under very similar conditions, the authors observed that the presence of Zn was deleterious for the overall efficiency of the process (entries 2 and 3, Table 2). This is somewhat contradictive to the calculated adsorption parameters, which point to a higher adsorption capacity of Zn-TiO_2/pBC. One suggested reason may be the difference in the external surface area of both catalysts, which was much higher in the case of TiO_2/pBC, even if the other area/volume parameters were favorable to Zn-TiO_2/pBC. Also, no direct correlation between adsorption capacity and degradation efficiency can be underlined from another **SMX** degradation study (entry 1, Table 2) by a TiO_2 biochar system [24]. Indeed, if this system showed higher q_m and q_e values than those obtained for TiO_2/pBC, as well as higher surface area, the same degradation yield of **SMX** was reached (91%) after a longer time of irradiation (6 h versus 3 h). Moreover, if generally, the adsorption capacity of the catalysts varies between *ca* 30–55% [36, 38, 42, 43] (entries 4–8, Table 2), some authors investigated ways to improve it. Tianqi Wang et al. compared the adsorption capacity of iodine doped biochar (I/WSP, obtained from wheat straw pellets and I/OST, obtained from oil seed rape straw) in the degradation of **TC** (entry 8, Table 2) [34]. Figure 4a displays its photocatalytic degradation of **TC** by the pristine biochar and I-doped biochar catalysts. The adsorption capacity of I-doped biochar toward a large-sized pollutant such as **TC**, is slightly improved due to the limited formation of mesopores upon I-doping. As shown in Fig. 4 I/WSP and I/OSR showed ca. 19% and 4% increase in the adsorption amount of **TC** ($q_e = 16\ mg\ g^{-1}$ for I/WSP and $q_e = 22\ mg\ g^{-1}$

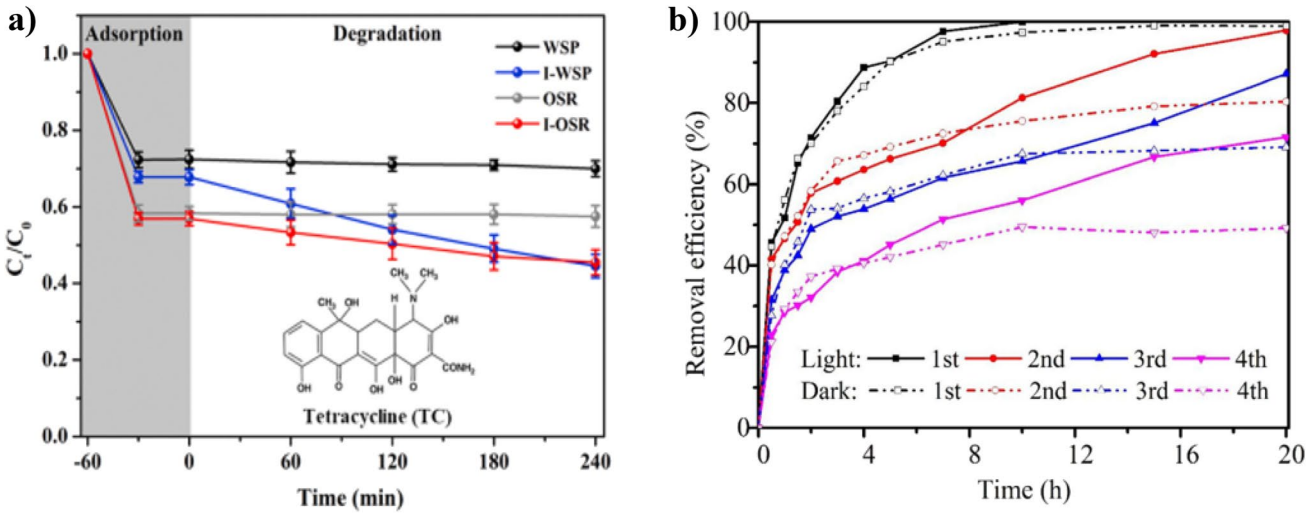

Fig. 4 **a** Photocatalytic degradation of **TC** by the pristine biochar (WSP and OST) and I-doped biochar (I/WSP and I/OST) under visible light (reproduced with permission from reference [34]); **b** reutilization cycles for the photocatalytic degradation of **AMX** using TiO_2/PFB under visible light (reproduced with permission from reference [39])

for I/OSR), respectively, when compared to the corresponding non-doped biochar samples. Although the improvement of **TC** adsorption is not substantial, the I-doped biochar samples still exhibited improved photocatalytic activity, where I/WSP compensates a lower adsorption capacity by and improved photocatalytic efficiency, when compared with I/OSR, reaching both catalysts to a 78% degradation.

An exception on the adsorption capacity was reported by [39] (entry 9, Table 2), who prepared photocatalyst TiO_2/PFB constituted by TiO_2 immobilized into biochar made from poultry feather (PFB). In particular, the PFB was achieved with self-crosslinking, due to its keratin component, being obtained as multi-layered PFB nanosheets, in a graphene-like structure. This material reached an impressive $q_e = 103$ mg g^{-1}, which permitted a 99% photodegradation of **AMX** with an adsorption being responsible for 84% removal after 4 h (first cycle). Although the adsorption capacity reduces gradually in the next recycles, the adsorption removing efficiencies (at the first 4 h) were still reaching 65%, 50% and 40% for the second, third and fourth cycle, respectively (Fig. 4b). The dropped efficiencies of adsorption from the 1st to 4th cycle was attributed to the competitive effects of photoproducts and adsorption functional sites' decreasing. Indeed, when a degradation process is more dependent on the adsorption capacity of a photocatalyst than on its ability to produce ROS for the aqueous media, catalyst reutilization is normally deficient, not allowing constant degradation rates.

At the opposite, combination of aloe vera plant extracts as biochar source with a TiO_2 precursor, to yield the photocatalyst named TiO_2/Aloe, already mentioned regarding the influence of pyrolysis temperature (Entry 4, Table 1) [44] was proved to create a 3D-tripyramidal structure thanks to a particular network with high specific surface area. Thus, this provided more active sites for the catalytic reactions. However, interestingly, adsorption did not play a significant role in the degradation of **CIP**, being responsible for less than 10% **CIP** removal. Under UV–vis light irradiation, 90% photodegradation of a low-concentration aqueous **CIP** solution was achieved after 60 min and a reaction rate of $k_1 = 0.0403$ min^{-1} (pseudo first order). The catalyst was also evaluated for its recyclability, with five reutilization cycles with a small loss of performance, confirming the low involvement of adsorption. If adsorption capacity plays a very important role in every heterogeneous-based photocatalyst degradation process, the photochemical process is also highly dependent on other parameters influencing the course and efficiency of photocatalytic degradation of antibiotics that are related to operational features, including drug/catalyst concentration, pH/temperature, irradiation, degradation time, catalyst stability. Direct parametrization of these factors allows to improve the overall efficiency of an antibiotic photodegradation process, ultimately aiming the best possible and sustainable degradation efficiencies, reaction rates, mechanistic elucidations, catalyst reusability and antibiotics mineralisation degrees.

2.3 Influence of operational parameters

The most common operational parameters that require attention and optimization are usually the substrate (antibiotic) concentration, catalyst loading, pH and temperature. Usually, partial or full combination of these factors is crucial to achieve a highly efficient catalytic system. Table 3 shows

Table 3 Selected examples of the application of biochar-based photocatalysts, summarizing some operational features

Entry/references	Catalyst loading range (g L^{-1})[a]	Antibiotic concentration range (mg L^{-1})[a]	pH and temperature[a]	Matrix	Antibiotic (AB)/catalyst (Cat) ratio	Efficiency
1/[24]	[TiO_2/BC] = 2.5–10 (**5**)	[**SMX**] = 10	pH = 4 *T* = 25 °C	Deionized water and in presence of HCO_3^-, NO_3^-	AB/Cat = 0.002	91% deg. **SMX** after 6 h
2/[25]	[TiO_2/pBC] = 1.25–2.5 (**1.25**)	[**SMX**] = 5–30 (**10**)	pH = 4 *T* = 25 °C	Deionized water, Yellow river and in presence of SO_4^{2-}, Cl^-, NO_3^-	AB/Cat = 0.008	91% deg. **SMX** in deionized water 66% in Yellow River water (both after 3 h)
3/[26]	[Zn-TiO_2/BC] = 1.25–2.5 (**1.25**)	[**SMX**] = 5–30 (**10**)	pH = 4 *T* = 25 °C	Deionized water, Yellow river and in presence of SO_4^{2-}, Cl^-, NO_3^-	AB/Cat = 0.008	81% deg. **SMX** in deionized water 54% in Yellow River water (both after 3 h)
4/[36]	[N,S-TiO_2/ASB] = 0.1–3.5 (**0.5**)	[**CIP**] = 5–50 (**30**)	pH = 3–11 (**5**) *T* = 25 °C	Deionized water	AB/Cat = 0.060	86% deg. **CIP** after 2.5 h
5/[30]	[Fe_3O_4-TiO_2/BC] = 0.25–1 (**0.35**)	[**MNZ**] = 10–40 (**20**)	pH = 3–11 (**7**) *T* = 25 °C	Deionized water, drinking water and hospital wastewater	AB/Cat = 0.060	100% deg. **MNZ** after 0.75 h
6/[29]	[Fe_3O_4-TiO_2/BC] = 0.25–1 (**0.35**)	[**TC**] = 10–40 (**10**)	pH = 3–11 (**7**) *T* = 25 °C	Deionized water, drinking water and hospital wastewater	AB/Cat = 0.030	97% deg. **TC** after 0.75 h
7/[41]	[ZnO/P] = 0.125–0.75 (**0.5**)	[**AMX**] = 15–60 (**30**)	pH = 5–11 (**9**) *T* = 25 °C	Deionized water	AB/Cat = 0.060	86% deg. **AMX** after 2 h
8/[32]	[Zn-Co-LDH/BC] = 0.15–0.75 (**0.75**)	[**GMF**] = 15–35 (**15**)	pH = 2.5–12.5 (**5.5**) *T* = 25 °C	Deionized water	AB/Cat = 0.020	93% deg. **GMF** after 2 h
9/[33]	[$BiFeO_3$/BC] = 0.5–2 (**1.5**)	[**CIP**] = 5–30 (**10**)	pH = not adjusted *T* = 25 °C	Deionized water	AB/Cat = 0.007	77% deg. **CIP** after 2 h
10/[46]	[UiO-66/wood] = 0.29–1.14 (**0.58**)	[**OFX**] = 4–20 (**10**)	pH = 6 *T* = 25 °C	Deionized water	AB/Cat = 0.020	80% deg **OFX** after 5 h
11/[28]	[TiO_2/KBC] = 0.25	[**ERF**] = 20–200 (**100**)	pH = 3–11 (**5**) *T* = 25 °C	Deionized water	Irradiation source evaluated (best results with UV light) AB/Cat = 0.400	85% deg. **ERF** after 2 h
12/[40]	[TiO_2/ZPS] = 0.05–0.25 (**0.05**)	[**AMP**] = [**SMX**] = 20–100 (**50**)	pH = 3–11 (**5**) *T* = 25 °C	Deionized water, several wastewaters and in presence of Cl^-, SO_4^{2-}, HCO_3^-, PO_4^{3-}	AB/Cat = 1.00	> 95% deg. for **AMP** 65% for **SMX**, both after 1 h
13/[31]	[Cu_2O/BC] = 0.2–1.6 (**0.6**)	[**TC**] = 10–50 (**20**)	pH = 4.3–10.5 (**6.5**) *T* = 10–50 °C (**40** °C)	Deionized water, several wastewaters and in presence of Cl^-, SO_4^{2-}, HCO_3^-, CO_3^{2-}, PO_4^{3-}	Temperature evaluated (best results at 40 °C) AB/Cat = 0.030	85% **TC** deg. after 2 h

[a]Best value in parenthesis bold

the summary of results of reports that experimentally evaluated at least one of these parameters in their studies [24–26, 29–33, 36, 37, 41].

The goal of optimizing operational parameters is, naturally, to find the best compromise between the maximum quantities of contaminant treated, using the lowest possible catalysts amount, under the most amenable pH and temperature conditions. Expectedly, the most adequate temperature is the ambient temperature (standard 25 °C, even if this temperature may vary according to latitude and season) and this was the temperature used in almost all cases (entries 1–12, Table 3), with exception of the work by Li and Jiang [31], who evaluated several operational temperatures (10, 20, 25, 30, 40 and 50 °C) and observed that, the higher temperatures favored the degradation of **TC** (entry 13, Table 3). Nevertheless, for convenience, the authors performed all further experiments at 20 °C, which was considers as ambient temperature in their case.

Regarding the pH parameter, neutral to slightly acidic values are seen as preferred, which meets the amenability requirements, since most real-life wastewaters show pH in the range 5–7, and the pH range mostly studied meets the range between 3 and 11. However, the optimal value mainly relies on the possible electrostatic interaction between the drug and the photocatalytic material, according to the acid base properties of both, and/or the improved solubility of the drug, depending in aqueous media, among others, of its charge. In this framework, Kim [24] Zhang [25] and Xie [26] adjusted their photocatalytic **SMX** oxidation experiments to pH 4 (entries 1–3, Table 3) to keep a non-ionic (neutral) **SMX** nature, based on its pKa [53]. Meanwhile Isa [41] made their **AMX**-photodegradation experiments at pH 9 (entry 7, Table 3), due to **AMX** pKa and improved solubility under basic conditions [54]. pH values in the 5–7 range were used in all the other reports on the photodegradation of several antibiotics, leaning on the conditions usually found in wastewater, tap water and lab deionized water. It should be mentioned that, in most cases, pH values were simply registered and not adjusted to any particular value, to mimic the natural conditions.

Also, independently of the adsorption capacity, higher substrate concentrations will implicitly decrease the amount of contaminant adsorbed; conversely, higher catalyst does will promote the amount of antibiotic adsorbed. This, adequate catalyst loadings and antibiotic concentrations are usually optimized from the compromise between the maximum amounts of contaminants treated using the lowest possible amount of catalyst. This is clearly the case in all the studies in Table 3. However, the antibiotic/catalyst w/w ratios (AB/Cat) are well below unity, indicating the need for extremely high catalyst loadings, together with reduced sustainability impacts. From this particular point of view, the "worst" cases have been observed by Kim [24] and Azan [33], with AB/Cat w/w ratios of 0.002 and 0.007, respectively, while the least "worst" examples were given by Wang (entry 11, Table 3) [28], and Alfred (entry 12, Table 3) [40], who reported AB/Cat ratios of 0.4 and 1, respectively.

2.4 Reusability and mineralisation

The most efficient and sustainable photodegradation processes are those that aim not only for the best degradation percentages and reaction rates, but also for the highest possible mineralisation input. In addition, the heterogeneous nature of the catalysts allows its reusability, conditioned by its stability.

Considering only the factors summarized in Table 4, photodegradability, mineralisability, and reaction rates are highly dependent on the nature of the antibiotic, besides other factors already focused. On the other hand, reusability is exclusively related to the stability of the catalyst. The successful optimization of these factors combined is indeed the pinnacle of an efficient and sustainable photodegradation system. Typically, photodegradation yields are superior to mineralisation yields because they represent the disappearance of the initial antibiotics and do not reflect the complete conversion of the contaminants to carbon dioxide, water, and small organic residues. These values are also used to assess the rate of the corresponding reaction and may be indicative of reaction efficiency.

The works here reviewed are exclusively laboratorial experiments and are only indicative of the efficiency and sustainability of a given system. As examples, the reports [29, 30, 38–40, 42, 43] reached values $\geq 95\%$ degradation (entries 4–8, 10 and 13, Table 4, respectively). Only some of them [29, 30, 42, 43] (entries 7, 8, 10 and 13, Table 4, respectively) managed to reach $\geq 80\%$ mineralisation. For instance, Kalantary reported a two-step procedure for the synthesis of Fe_3O_4-TiO_2/BC, a catalyst obtained by the combination of biochar obtained from rice husk by calcination and magnetic Fe_3O_4. Such blend was then mixed with freshly-prepared TiO_2 and calcinated at 450 °C to produce the desired hybrid catalyst. The system was tested in the photodegradation of **TC**, in presence of UV-light irradiation with a 16 W Hg lamp at 25 °C (Entry 7, Table 4) [30]. A pH of 7 proved most favorable, and 97% TC degradation and 80% mineralisation was observed, with a first order kinetics ($k_1 = 0.0437\ min^{-1}$) with $O_2^{\cdot -}$, $^{\cdot}OH$ radicals and h^+ as the mechanism enforcers. The authors further performed microbiology studies, to assess antibacterial activity of oxidation products. The antibacterial activity of the aqueous solution containing tetracycline antibiotic before and after the composite photocatalytic process were tested using *Staphylococcus aureus* bacteria, where the products had no toxicity to the bacteria used, meaning that they showed lower risk for

Table 4 Summarizes a selection of the processes that performed reusability and mineralisation experiments

Entry/references	Catalyst/light source	Photodegradation/mineralisation	Reaction rate/reusability
1/[24]	TiO_2/BC 15 W UV-C lamp	91% **SMX** deg. (6 h) 81% of mineralisation (6 h)	k_1: NR Reutilization: NR
2/[25]	TiO_2/pBC 50 W UV Xe lamp	91% **SMX** deg. in deionized water 66% in Yellow River water (3 h) 57% mineralisation (3 h)	$k_1 = 0.040\ min^{-1}$ 5 reuse cycles (~20% efficiency loss)
3/[26]	Zn-TiO_2/pBC 50 W UV Xe lamp	81% **SMX** deg. In deionized water, 54% in Yellow River water (3 h) 56% mineralisation (3 h)	$k_1 = 0.0085\ min^{-1}$ 5 reuse cycles with no negligible loss of activity (~8%)
4/[38]	TiO_2/TCT 300 W UV Xe lamp	99% **TH**•HCl deg. (0.5 h) 67% mineralisation (0.5 h)	$k_1 = 0.0128\ min^{-1}$ 4 reuse cycles with no loss of activity
5/[39]	TiO_2/PFB 500 W UV Xe lamp	99% **AMX** deg. (20 h) 74% mineralisation (20 h)	$k_2 = 0.0118\ g\ mg^{-1}\ min^{-1}$ 4 reuse cycles with reduction of catalyst activity (99 to 72%)
6/[40]	TiO_2/ZPS and TiO_2/ZPP Sunlight exposure	95% **AMP** and 65% **SMX** deg. with TiO_2/ZPS (1 h) 75% **AMP** and 50% **SMX** mineralisation (1 h)	$k_1 = 0.0315$ and $0.0227\ min^{-1}$ for **AMP** and **SMX**, respectively 5 reuse cycles with no loss of activity
7/[30]	Fe_3O_4-TiO_2/BC 16 W UV Hg lamp	100% **MTR** deg. (0.75 h) 80% mineralisation (0.75 h)	$k_1 = 0.0747\ min^{-1}$ 5 reuse cycles with no loss of activity
8/[29]	Fe_3O_4-TiO_2/BC 16 W UV Hg lamp	97% **TC** deg. (0.75 h) 80% mineralisation (0.75 h)	$k_1 = 0.0437\ min^{-1}$ for **TC** 5 reuse cycles with negligible activity loss
9/[41]	ZnO/P 9 W UV Hg lamp	86% **AMX** deg. (2 h) 80% mineralisation (3.5 h)	$k_1 = 0.047\ min^{-1}$ for **AMX** 5 reuse cycles with negligible loss of activity
10/[42]	CuO/AC 200 W UV W lamp	98% **AMX** deg. (1.5 h) 93% mineralisation (1.5 h)	$k_1 = 0.0220\ min^{-1}$ 4 reuse cycles with ~30% activity loss
11/[32]	Zn-Co-LDH/BC 10 W UV-B lamp	93% **GMF** deg. (2 h) 80% mineralisation (3.5 h)	$k_1 = 0.0257\ min^{-1}$ 5 reuse cycles with -10% activity loss
12/[33]	$BiFeO_3$/BC Sunlight exposure	77% **CIP** deg. (2 h) 14% mineralisation (2 h)	$k_1 = 0.0078\ min^{-1}$ Reutilization: NR
13/[43]	WO_3/BiOCl/GSC Sunlight simulator	80% **OTC** and ~99% **AMP** deg. (8 h) 99% AMP mineralisation (8 h)	$k_2 = 4.0 \times 10^{-6}\ mol\ dm^{-3}\ min^{-1}$.(OTC) and $(k_{obs}) = 5.3 \times 10^{-6}\ mol\ dm^{-3}\ min^{-1}$ (**AMP**) 4 reuse cycles with negligible loss of activity
14/[36]	N,S-TiO_2/ASB 500 W UV Hal lamp	86% **CIP** deg. (2.5 h) Mineralisation: NR	$k_1 = 0.0403\ min^{-1}$ 3 reutilization cycles with ~10% efficiency loss
15/[44]	TiO_2/Aloe 300 W UV Xe lamp	90% **CIP** deg. (1 h) Mineralisation: NR	$k_1 = 0.0403\ min^{-1}$ 5 reutilization cycles with a small loss performance
16/[28]	TiO_2/KBC 15 W UV lamp	85% **ERF** deg. (2 h) Mineralisation: NR	$k_1 = 0.0201\ min^{-1}$ 4 reutilization cycles with no loss of activity
17/[31]	Cu_2O/BC 250 W UV Xe lamp	85% **TC** deg. (2 h) Mineralisation: NR	$k_1 = 0.0160\ min^{-1}$ 4 reutilization cycles with no loss of activity
18/[45]	$BiVO_4$/AC 300 W UV Xe lamp	80% **OTC** deg. (1.5 h) Mineralisation: NR	$k_1 = 0.0112\ min^{-1}$ 4 reutilization cycles with negligible loss of activity

NR means non-reported

bacteria, not inhibiting their growth. The duration and the power of the light irradiation are usually very important for the efficiency of the photodegradation process, but, in the cases here considered, some of the best results were obtained with quite low irradiation power (16 W mercury [29, 30]) or even the most desirable sunlight exposure [43]. This suggests that several other factors must be taken into account when analyzing the processes. This is also reflected in the reaction rates, which are mostly fitted by pseudo first order kinetics, except two cases, were the best fitting model was a second order kinetics (see Table 4). Many of the works have included reutilization studies, to evaluate catalysts stability. This feature is very important when designing a real-world photodegradation system. Either four or five recycling cycles are commonly performed; however, this only gives an indication of the trend, as in a real-world situation only 4–5 recycling cycles would be insufficient for each catalytic process. Although time consuming, at least 10 cycles should be performed to allow a straightforward assessment of catalyst stability.

The mechanisms of photodegradation are based on the production of ROS, which are usually hydroxyl ($^{\cdot}OH$), and superoxide ($O_2^{\cdot-}$) radicals, as well as semiconductor holes (h^+). In most of the cases discussed here, these are responsible for the destruction of the bonds present in the antibiotic organic molecules. Thus, the photodegradation and mineralisation rate of antibiotics is highly dependent on their nature, i.e., their structural features. The study of antibiotic degradation pathways is therefore necessary to understand the mechanisms behind the desired complete transformation into CO_2, H_2O and other small organic/inorganic residues, but it is out of the scope of the review as the impact of the biochar-based supported matrix is not directly linked to this. However, a synergy effect between the semiconductor catalyst and the biochar supporting matrix is observed in several studies. For instance, Xie (Entry 2, Table 4) [25] studied the photodegradation of **SMX**, using TiO_2/pBC as catalyst and evaluated the photodegradation of SMX and mineralisation by measuring the COD (Chemical Oxygen Demand), under the irradiation of simulated sunlight or UV light (in absence of photocatalyst), and in presence of pristine TiO_2 and TiO_2/pBC, under UV light (Fig. 5).

Direct photolysis, with either simulated sunlight or UV light produced unsatisfactory results, regarding both degradation and mineralisation, while, in presence of pristine TiO_2 and TiO_2/pBC degradation rates (respectively 58 and 91%) and mineralisation (respectively 46% and 57%) were significantly enhanced, particularly for TiO_2/pBC, which proved the benefit of use of biochar as support. Similarly, mineralisation was also more improved when TiO_2/pBC, instead of pristine TiO_2, was used, which was attributed to the mechanism, where the photocatalyst's semiconductor h^+, in presence of water matrix, produced $^{\cdot}OH$ radicals, and

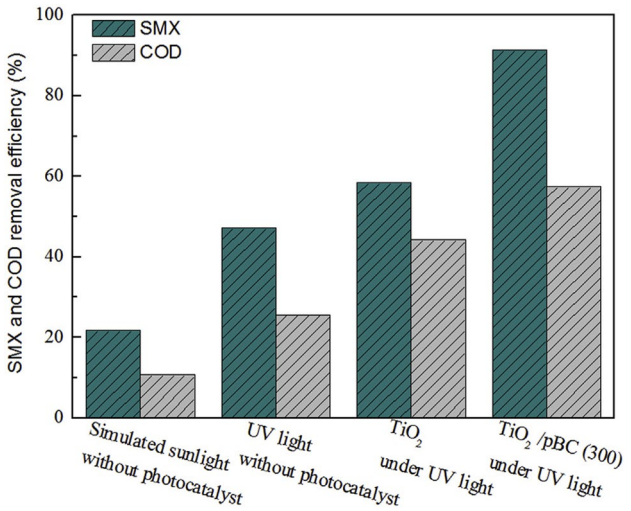

Fig. 5 Removal efficiency of **SMX** and COD under photolysis and photocatalysis. Reproduced with permission from reference [25]

then these radicals led to a high mineralisation. Reutilization studies were carried out for this catalyst, which showed a 20% decrease in efficiency. An additional experiment was performed, using water from the Yellow River at Lanzhou, China, as aqueous matrix, instead of deionized water. Inorganic anions present in the water matrix inhibited the photocatalytic capacity of TiO_2/pBC, by reacting with $^{\cdot}OH$ and h^+ generated, causing a decrease in **SMX**'s degradation efficiency to ~ 66%.

To conclude this part focused on biochar utilization, the system studied by Singh [43] must be underlined. Indeed, **OTC** and **AMP** antibiotics were photodegraded using a binary WO_3/BiOCl photocatalyst stacked to graphene sand composite (GSC) and chitosan (CT). A modified hydrolysis method was used to prepare the WO_3/BiOCl photocatalyst, which was then immobilized onto GSC, prepared from common sugar and river sand by carbonization, and onto CT, using the same method, to produce WO_3-BiOC/GSC and WO_3-BiOCl/CT nanocomposites. Under sunlight simulation for 8 h, the authors observed that, for **OTC** degradation, an 80% and 76% removal was obtained using WO_3-BiOC/GSC and WO_3-BiOCl/CT photocatalysts, respectively (entry 5, Table 1). Similarly, WO_3-BiOC/GSC was more efficient for **AMP** degradation, reaching 99% removal, against 92% by WO_3-BiOCl/CT. The authors also observed, using WO_3-BiOC/GSC, the mineralisation efficiency was complete for both antibiotics; however, reutilization proved complicated, with a 40% loss after 10 reuse cycles, mostly due to catalyst recovery problems. Other interesting findings allowed the authors to determine that that the long-term degradation did not involve simple pseudo first order kinetics. The degradation process tended to be slower with increased degradation time, which was attributed to the influence of adsorption onto the surface of photocatalyst, which degraded antibiotic's fragments. Under solar irradiation, the transition of electrons from conduction band of BiOCl to conduction band on WO_3 side resulted in generation of h^+ in valence band, along with the production of $O_2^{\cdot-}$ radicals.

3 Hybrid systems based on biopolymer matrices

The use of biopolymer matrices has been also investigated thoroughly to immobilize photocatalysts. It can be seen as an alternative strategy that enhances catalyst recyclability and enables the application of this process on a larger industrial scale, such as in water treatment. Especially, immobilizing photocatalysts within an adsorptive biomaterial improves their recovery and photodegradation properties by bringing pollutants closer to the active sites of the catalysts. Among biopolymer-based substrates, natural polymers like alginate, chitosan and cellulose have gained significant attention,

especially in the realm of 3D materials. They mitigate photocatalyst aggregation, exhibit strong adsorption capabilities, provide efficient mass transfer channels, and can be easily separated from the reaction solution. In addition, their mechanical strength and thermal stability make them attractive for water purification applications. Moreover, they can form floating materials, making them promising for water treatment. However, one of the challenges is designing and shaping suitable materials for immobilizing photocatalysts while preserving their photoactive properties. In subsequent studies, authors often develop a hybrid process that combines adsorption and photocatalytic degradation. It is important to note that the shielding effect of the matrix, which can limit light absorption by the photocatalyst and photoinduced reactions, can be overcome by immobilizing photocatalyst NPs in membranes or hydrogels made from biopolymers. Among the photocatalysts immobilized in these matrices, TiO_2 remains the most widely used due to its cost-effectiveness, non-toxicity, strong oxidizing potential, wide commercial availability, and high stability against photochemical corrosion. Recently, some authors have also explored effective bismuth or iron derivatives.

3.1 Alginate matrix

Alginate is a hydrophilic polymeric colloid composed of alternating (1 → 4)-linked β-D-mannuronate and α-L-guluronate residues. It exhibits good adsorption capacity due to the presence of numerous anchoring points provided by the abundance of oxygen-containing functional groups, including carboxyl and hydroxyl groups. Two types of alginates are available: sodium alginate, a natural biopolymer extracted from brown seaweed, and calcium alginate, which is synthesized from sodium alginate. Calcium alginate exhibits better thermal stability and mechanical strength compared to sodium alginate. However, both types are extensively utilized for their ability to adsorb pollutants. They can be shaped into porous NPs, either in dry form or as hydrogels. In the following sections, we will delve into recent advancements in the use of alginate as a biopolymer matrix for immobilizing various photocatalysts. The following sections are summarized in Table 5.

Table 5 Summary of Alginate based photocatalysts regarding their structural properties, photodegradation efficiency and reusability

Reference	Photocatalyst material light source	Porosity surface area (S_{area}), volumes (P_{vol})	Photodegradation ROS involved mineralisation	Recycling/activity/method
[12]	S–TiO_2/WS_2 beads 1–1.5 mm solar light irradiation	Porous macro-sized beads	93% **OTC** deg. (10 mg L^{-1}), pH = 6 in 4 h h^+, $O_2^{\cdot-}$ and $^{\cdot}OH$	79% **OTC** removal after five cycles Filtration
[55]	TiO_2/Polysulfone beads 1–6 mm UV-light irradiation	Micropores (4–8 µm) S_{area} = 7.9 m^2 g^{-1} suspended-to-floating interswitchable feature	100% **TCS** and **DCF** deg. (20 mg L^{-1}) in 40 min and 2 h $^{\cdot}OH$ 97% MB mineralisation (2 h)	100% **TCS** and **DCF** deg. after 25 cycles under batch and continuous modes Filtration
[56]	TiO_2/Ag_3PO_4/Polysulfone UV irradiation	Macrovoids pores (30–90 nm) S_{area} = 5.4 m^2 g^{-1} suspended or floating beads	100% **TCS** and **DCF** deg. (20 mg L^{-1}) in 80 min and 2 h $^{\cdot}OH$ and h^+	100% **TCS** and **DCF** deg. after multiple cycles Filtration of the floating form
[13]	Reduced Graphene Oxide-TiO_2 UV-light irradiation	Floatable aerogel beads	99% **SMX** deg. (10 mg L^{-1}) in 45–90 min $^{\cdot}OH$ 74% mineralisation	100% **SMX** deg. after five cycles Continuous flow
[57]	$Bi_4O_5I_2$/SPION Egg-box model Visible, UV, NIR and solar light irradiation	S_{area} = 44.3 m^2 g^{-1} bulk	98% **AZY** (10 mg L^{-1}) deg. in 90 min $^{\cdot}OH$ and $O_2^{\cdot-}$ 90% mineralisation under UV irradiation	100% **AZY** deg. after five cycles. Negligible leaching of I and Fe metal Magnetic recycling
[58]	$FeCl_3$/poly(vinyl alcohol) beads 5 mm Visible-light irradiation	Micropores (1.16 µm) Hydrogel beads	91% **TC** (20 mg L^{-1}) deg. (with H_2O_2 6 mM), in 1 h h^+, $^{\cdot}OH$ and $O_2^{\cdot-}$ 29% mineralisation	85% **TC** deg. after 5 cycles, leaching (20%) of Fe metal after 5 cycles Filtration
[59]	Fe_3O_4-ZnO Alg./CS. hybrid beads 1.6 mm UV-C light irradiation	P_{vol} = 1.9 × 10^{-2} cm^3 g^{-1} S_{area} = 1.08 m^2 g^{-1} beads	94% **CIP** and 93% of **SMX** deg. (10 mg L^{-1}) in 3 h $O_2^{\cdot-}$ and $^{\cdot}OH$ 80% mineralisation	50% **CIP** and **SMX** deg. after five cycles Filtration

NR means non-reported

3.1.1 Adsorption role in efficiency and recovery

As outlined in the previous part, optimizing the adsorption of both the photocatalyst and the organic pollutant is a major challenge in heterogeneous photocatalysis. The adsorption of contaminants near or on the photocatalyst must be optimal to achieve effective photodegradation. Furthermore, sometimes the use of a single polymer support does not efficiently attract both polar and nonpolar organic pollutants and bring them close to the photocatalysts. A combination of materials with complementary properties is sometimes necessary to produce an effective composite material for immobilizing both the pollutant and the photocatalysts. In addition, immobilizing photocatalytic NPs within suitable materials with high adsorption capacities for target pollutants offers several advantages. It not only simplifies catalyst recovery but also brings priority pollutants into close proximity to the catalyst sites, enhancing photocatalytic activity. They also offer numerous benefits such as durability, mechanical and thermal stability, easy availability, chemical inertness, nontoxicity, low density, and cost-effectiveness.

In their study, Kumar et al.[12] presented an adsorbent-photocatalyst integrated material based on sulfur-doped TiO_2/tungsten disulfide (S–TiO_2/WS_2/alginate) in the form of porous macro-sized beads (1–1.5 mm). This photocatalyst was synthesized by incorporating S–TiO_2/WS_2 NPs into modified calcium alginate. The hydrophobic and agglomerative nature of WS_2 was effectively addressed by its combination with alginate. The hydrophilic nature of alginate played a crucial role in facilitating the movement of pollutants within the photocatalyst's structure. The authors explained that the adsorption process involved the formation of hydrogen bonds, cation bridge bonding, and n–π electron donor–acceptor forces. These interactions were attributed to the presence of double bond benzene rings, oxygen and nitrogen, as well as sulfur-containing functional groups on **OTC** and S–TiO_2/WS_2/alginate beads. They also noted that within a span of 120 min, adsorption reached saturation, achieving a peak removal efficiency of 47% when the initial **OTC** concentration was 10 mg L^{-1}. Moreover, those porous macro-sized S–TiO_2/WS_2/alginate beads can be easily recovered by filtration once the reaction is complete. These beads demonstrated excellent sustainability in **OTC** removal, with an efficiency of approximately 79% even after undergoing five cycles.

The same kind of interaction have been evidenced by Nawaz et al. [13] who introduced a novel approach to create materials with a large surface area for adsorbing both pollutants and TiO_2 NPs. They synthesized a three-dimensional interconnected macroporous-aerogel based on reduced graphene oxide-TiO_2/sodium alginate (RGOT/SA). This material exhibited efficient charge partitioning and enhanced both chemical and physical adsorption of **SMX** on the aerogel's surface. The structure showed a uniform anchoring of TiO_2 nanoparticles (NPs) within the RGOT/SA aerogel. The high adsorption capacity for **SMX** (more than 50% removal in just 40 min) was attributed to several factors, including the high surface area, hydrogen bonding, and π-π interactions between **SMX** and the RGOT/SA aerogel. This floatable TiO_2-RGOT/SA aerogel was moreover utilized in five consecutive cycles, without removal, washing, or any treatment, and its degradation efficiency remained unaffected. Unlike TiO_2 NPs in slurry form, the TiO_2-RGOT/SA aerogel could be easily separated from the solution, preventing any secondary pollution that might occur due to the transfer of NPs into the secondary effluent. In addition, PVA/SA-$FeCl_3$ hydrogel beads [58] could be easily filtrated and recycled. Notably, the removal rate of **TC** by the PVA/SA-$FeCl_3$ hydrogel beads remained constant without any loss of photocatalytic activity even after five cycles. Furthermore, there was almost no change in the porous morphology and chemical structure before and after the repeated experiments. However, some leaching of Fe ions from SA (approximately 20% after five cycles) was observed. In [59], the feasibility of reusing Fe_3O_4-ZnO-CS/SA nanocomposite beads was explored by filtration. These beads were successfully recycled five times, although they experienced a fifty percent loss of photocatalytic activity after each recovery cycle. The authors hypothesized that the porous structure of the SA/CS matrix became blocked by intermediate products formed during the photocatalytic process. Indeed, the XRD pattern of the nanocomposite exhibited changes in the crystal phases of the nano-ZnO and Fe_3O_4 after recycling, suggesting a likely photo-oxidation reaction occurring on the composite surface.

In their study, Mehmood et al.[55] introduced amphiphilic porous polymer macro beads (3 mm) based on a modified polysulfone-alginate (PSF/Alg) matrix for immobilizing the TiO_2 photocatalyst (PAT-12 M). This polymer composite exhibited significantly higher stability and adsorption capacity for pollutant molecules compared to its individual constituents. The hydrophobic nature of Polysulfone (PSF) facilitated the adsorption of nonpolar organic contaminants on the composite's surface, where photocatalysts were anchored. Conversely, the hydrophilic nature of alginate contributed to excellent adsorption capacity, thanks to its abundance of oxygen-containing functional groups. The synergy between these two polymers with complementary properties resulted in an efficient composite material capable of attracting both polar and nonpolar organic pollutants while immobilizing TiO_2. The high porosity (4–8 µm pores) and surface area (7.9 m^2 g^{-1}) of the PAT-12 M beads further ensured a high adsorption capacity, reaching 60% removal efficiency in just 90 min. The optimized chemical composition of these beads exhibited remarkably high photocatalytic activity when exposed to **triclosan** (**TCS**) and **diclofenac**

(**DCF**) pollutants (both at 20 mg L^{-1}). Indeed, under UV irradiation, these composite beads exhibited outstanding performance, achieving nearly complete removal of **TCS** in just 40 min and **DCF** in 120 min. This underscores their remarkable effectiveness in the degradation of these pollutants. The degradation activities of these composite beads are comparable to those observed with TiO_2 powder. In addition, the durability of the porous polymer beads was studied. They can undergo at least 25 cycles under batch mode and for 30 days in continuous mode, achieving over 99% degradation of **methylene blue** (**MB**). Due to their large size (3 mm) and excellent mechanical stability, these beads can be effortlessly dispersed in polluted solutions, either suspended or floating, and can be easily recovered without any loss of photocatalytic activity. In a subsequent study, the same authors introduced a modified composite known as PSF/Alg/TiO_2/Ag_3PO_4 (PATAg) beads [56]. These beads were developed by immobilizing TiO_2/Ag_3PO_4 within the PSF/Alg matrix, enabling photocatalysis under visible-light irradiation as opposed to UV-light irradiation, which was used in their earlier work [55]. The PATAg bead composites exhibited a sponge-like structure with macrosize pores of ovoidal shape (macrovoid pores) ranging from 30 to 90 nm and a specific surface area of 5.4 m^2 g^{-1}. Notably, these beads demonstrated exceptional thermal stability, maintaining their integrity up to temperatures of 450–500 °C. The authors emphasized the synergistic interactions between the catalysts and the immobilization material. In both cases, PAT-12 M and PATAg, the combination of high porosity and thermal stability in the beads ensured a high adsorption capacity for pollutants (59% removal in 6 h), contributing to the overall efficiency of the photocatalytic degradation process. PATAg beads can also be employed and recycled in either suspended or buoyant forms interchangeably for multiple cycles without experiencing any significant loss in photoactivity.

In another study, Du et al. [58] introduced hydrogel beads (5 mm) also based on a polymer composite approach as they are composed of poly(vinyl alcohol) (PVA)/sodium alginate (SA). These beads were synthesized using a chemical crosslinking method with $FeCl_3$ and boric acid serving as crosslinking agents. The resulting composite beads displayed a porous structure with a pore size of approximately 1.16 µm, which proved advantageous for the adsorption of the **TC** pollutant. Notably, these beads exhibited excellent stability against mechanical stresses, making them suitable for practical applications. The adsorption equilibrium for **TC** was achieved within 120 min, demonstrating the effectiveness of these hydrogel beads in capturing the pollutant.The authors explored the photo-Fenton performance of the photocatalyst for degrading **TC** pollutant (20 mg L^{-1}) under visible-light irradiation. This process primarily relies on the generation and utilization of hydroxyl ($^{\cdot}OH$) radicals as the oxidizing agent. The photocatalytic experiment, conducted under optimized conditions (with the addition of 6 mM H_2O_2), achieved an impressive **TC** removal rate of *ca* 91% within just 60 min of visible-light irradiation. The hydrogel beads, PVA/SA-$FeCl_3$, predominantly contained Fe^{3+} in the form of $[Fe(OH)]^{2+}$. When exposed to visible light, $[Fe(OH)]^{2+}$ underwent metal charge transfer excitation, producing Fe^{2+} ions that catalyzed the photolysis of H_2O_2. This photolysis process generated additional $^{\cdot}OH$ radicals, significantly increasing the oxidation rate of organic pollutants. Moreover, the study demonstrated the mineralisation of **TC**, leading to the formation of CO_2, H_2O, and other molecules, with a remarkable removal rate of *ca* 29%. In addition to the involvement of $^{\cdot}OH$ radicals, free-radical and hole trapping experiments revealed that h^+ (holes) played a primary role in the degradation process, while $^{\cdot}OH$ and $O_2^{\cdot-}$ radicals also contributed to the degradation of **TC**.

Furthermore, Kumar et al. [57] presented an example of a calcium alginate composite known as Ag@$Bi_4O_5I_2$/SPION@calcium alginate (ABSA). In this case, the robust calcium alginate structure, reminiscent of an egg-box model, provided a 3D network with high-strength binding capabilities for Bi^{3+} ions within the biopolymer. This material exhibited a remarkable capacity for adsorption, facilitating the effective binding of pollutants and photocatalysts. The high surface area, measuring 44.3 m^2 g^{-1}, of ABSA ensured a high functionality rate of the calcium alginate polymer, resulting in a rapid adsorption rate for **azythomycin** (**AZY**) pollutants. ABSA demonstrated an impressive adsorption potential, achieving a 48% removal of **AZY** in just 30 min. In addition, this superparamagnetic photocatalyst could be magnetically separated using a strong NdFeB magnet (Neodymium Iron Boron) closely positioned to the beaker. The photocatalyst ABSA could be recycled for at least five times, achieving complete **AZY** removal without any loss of photocatalytic activity after repeated use.

In line with the previous example, but taking advantages of biopolymers, in a recent study, Roy et al. [59] introduced a hybrid biopolymer matrix that combined Alginate and Chitosan. They synthesized the Fe_3O_4–ZnO–Chitosan/Alginate Nanocomposite by immobilizing nano-ZnO NPs and Fe_3O_4 NPs in chitosan/alginate polymer beads, using the SA/CS (sodium alginate/chitosan) matrix to create the nanocomposite structure. This hybrid matrix took advantage of the exceptional adsorption performances offered by both Chitosan and Alginate matrices. The electrostatic interactions between the carboxylate groups of SA and the amine groups from CS enhanced the adsorption activity of the nanocomposite. The study focused on the removal of **CIP** and **SMX** pollutants, which was achieved through the electrophilic nature of the nanocomposite, resulting in a remarkable adsorption rate of 94%. However, it is worth noting that the surface area of the nanocomposite decreased

from 1.08 $m^2\ g^{-1}$ (initial nanocomposite) to 0.8 $m^2\ g^{-1}$ after adsorption of pollutants, accompanied by a reduction in pore volume from 1.9×10^{-2} to 3.5×10^{-3} $cm^3\ g^{-1}$. This change led to a decrease in the diffusion of reagent molecules within the pores, subsequently affecting the photocatalytic activity rate of the composite.

3.1.2 Improving photocatalytic efficiency in alginate-based materials

As outlined previously, the photocatalytic activity of catalyst as well as their action mechanisms rely on their chemical structures. Among photocatalytic materials, TiO_2 has undergone extensive investigation due to its well-documented characteristics. With its relatively wide band gap of approximately 3.2 eV and a propensity for high-charge recombination rates, TiO_2 primarily exhibits activity in the UV-light spectrum. Consequently, there has been a concerted endeavor to enhance its performance in visible light. Photocatalysts with broader spectral responsiveness, coupled with improved charge separation and transfer capabilities, have piqued the interest of researchers for a myriad of photo-oxidative and reductive applications. This pursuit has led to the adoption of various strategies, including the functionalization of TiO_2 with photosensitizers, doping with both metallic and non-metallic elements, and the fabrication of composites incorporating polymers, metal oxides, or compounds designed to narrow the band gap. In this framework, in recent studies, researchers have investigated the efficacy of tungsten, bismuth, zinc, silver, or iron derivatives, whether coupled with TiO_2 or not. These photocatalysts exhibit enhanced spectral responsiveness and charge separation, thereby enhancing their performance in photo-oxidative or reductive applications.

In the case of the PATAg system, the authors [56] explored the performance of this modified composite PSF/Alg/TiO_2/Ag_3PO_4 compared to the previous one they studied (PAT-12 M, [55]) by incorporating Ag_3PO_4. Ag_3PO_4 possesses a narrow bandgap and in combination with TiO_2 effectively separates electron–hole pairs in TiO_2, creating a visible-light-responsive photocatalyst. The effectiveness of these PATAg beads under visible light was evaluated using **TCS** (kinetic constant k of 0.052 min^{-1}) and **DCF** (kinetic constant $k = 0.018$ min^{-1}) as target pollutants. Remarkably, the PATAg beads demonstrated a very high visible-light photocatalytic activity, achieving 100% removal of **TCS** in just 80 min. Further investigations into the photocatalytic degradation mechanism involved scavenging experiments for reactive oxygen species (ROS). The results indicated that $^{\cdot}OH$ radicals and h^+ are the primary reactive oxygen species responsible for the photodegradation process. Moreover, the authors highlighted the effectiveness of this photocatalytic process in bacterial inactivation and the degradation of acyl-homoserine lactones (AHLs). This aspect holds promise for applications in wastewater disinfection and biofilm retardation, showcasing the multifaceted potential of these PATAg beads.

Kumar et al. [57] also used Ag in their study focused on bismuth-based oxyhalides, specifically BiOX (where X can be Cl, Br, or I), known for their highly efficient visible-light activity and unique layered crystalline structure. Indeed, among these, $Bi_4O_5I_2$ stands out due to its elevated valence band (VB) edge, enhancing its oxidative capabilities, and a suitably positioned conduction band (CB), making it an excellent candidate for photocatalysis. This material exhibits high-performance photocatalytic capabilities not only under UV but also visible, near-infrared (NIR), and sunlight. In the composite, the incorporation of superparamagnetic iron oxide nanoparticles (SPIONs) and silver (Ag) dopants further improves its visible-light activity. Moreover, the redox mediation via the I^{3-}/I^- couple enhances charge flow, while Ag generates 'hot electrons' through the surface plasmon resonance (SPR) effect. In addition, built-in redox couples, such as Fe^{2+}/Fe^{3+}, and I^{3-}/I^-, act as electron shuttles, effectively reducing charge carrier recombination and facilitating electron transfer within the catalyst. The photocatalyst demonstrated remarkable performance, achieving a *ca* 98% degradation of **AZY** (10 mg L^{-1}) within just 90 min under visible light. Its efficacy extended to UV, NIR, and sunlight conditions. Notably, the apparent rate constant for the ABSA catalyst was approximately 8 times higher than that of bare $Bi_4O_5I_2$. $O_2^{\cdot-}$ radicals emerged as the primary active species responsible for **AZY** degradation, as validated by scavenging experiments and electron spin resonance (ESR) probes. The degradation pathways of **AZY** led to the formation of low molecular weight fragments. Over a more extended period, continued oxidation and degradation eventually resulted in mineralisation, as indicated by a high total organic carbon (TOC) removal rate of around 90% under UV irradiation.

Also, in their system S–TiO_2/WS_2/alginate-adsorbent photocatalyst, Kumar et al. [12], demonstrated high visible-light absorption and a reduced charge recombination rate thanks to the combination of S-TiO_2 and WS_2. The research focused on the catalytic decomposition of **OTC** (10 mg L^{-1}) in natural sunlight, achieving a maximum decomposition of *ca* 93% at pH = 6 within 240 min under solar light irradiation. Notably, OTC exists in a negatively charged molecular form (**OTC**$^-$) and zwitterionic form (**OTC**$^{+/-}$) in both basic and neutral media, which facilitates better interaction between OTC and the photocatalyst. A proposed photodegradation mechanism considered (i) the valence bands and conduction band energies of WS_2 and S-TiO_2 and (ii) quenching experiments with scavengers to identify the oxidizing radical species involved. The study concluded that photogenerated species such as h^+, $O_2^{\cdot-}$, and $^{\cdot}OH$ played vital roles in the degradation of **OTC**.

In their study, Nawaz et al. [13], in addition to introduce reduced graphene oxide for improving adsorption, has evidenced that graphene oxide (GO) played a crucial role in enhancing charge partitioning by facilitating the transport of photogenerated electrons. This efficient electron transfer effectively suppressed the recombination of charge carriers, leading to the high photocatalytic activity exhibited by the RGOT/SA aerogel. Under UV-A light irradiation, the RGOT/SA aerogel demonstrated exceptional performance, with over 99% removal of **SMX** (10 mg L^{-1}) achieved within 45–90 min. This removal rate surpassed that of bare TiO_2, where a constant rate of $k = 0.022$ min^{-1} was observed compared to 0.108 min^{-1} for RGOT/SA. The dominant role of $^{\cdot}OH$ radicals in the degradation of **SMX** was identified. Moreover, the mineralisation of SMX was significantly more effective with the RGOT/SA aerogel than with bare TiO_2 NPs. The RGOT/SA aerogel efficiently degraded **SMX** into its transformation products, which eventually mineralized into simpler substances, including CO_2, H_2O, and other inorganic ions. This was evident in the reduction of TOC by 74% for RGOT/SA, whereas it was 59% for bare TiO_2.

Other authors [59], reported a Fe_3O_4-ZnO-CS/SA nanocomposite with the ability to efficiently degrade **CIP** by around 95% and **SMX** by around 93%, both at a concentration of 10 mg L^{-1}, under UV-C light irradiation. This remarkable performance was achieved within a timeframe of 180 min, and the pH of the solution was maintained at 4.0 throughout the experiment. Zinc oxide (ZnO), known for its semiconducting properties, chemical and thermal stability, as well as its affinity for harmful ions in polluted water, was employed as the photocatalyst in this nanocomposite. Complementing ZnO, Fe_3O_4 NPs were chosen for their minimal toxicity and catalytic activity. The study proposed that the enhanced photocatalytic activity of the nanocomposite could be attributed to several factors, including its excellent absorbability, improved light-harvesting properties, reduced charge recombination, and synergistic effects resulting from co-loading chitosan (CS) and sodium alginate (SA) with nano-Fe and ZnO. Furthermore, trapping experiments elucidated that $O_2^{\cdot -}$ and $^{\cdot}OH$ radicals played a significant role in the photodegradation process. Importantly, mineralisation studies revealed that the residual TOC removal rate exceeded 80% for both antibiotics, underscoring the effectiveness of the nanocomposite in breaking down these pollutants.

3.2 Chitosan matrix

In terms of biopolymers used as supporting material for photodegradation of antibiotics, chitosan is indeed more and more used. Chitosan (CS) is a natural functional biopolymer with diverse applications, particularly as a biosorbent for metals, dyes, organic compounds, and more. It is obtained by deacetylation of chitin, a polysaccharide found in the structural components of marine organisms like crabs and shrimps. Chitosan is known for its non-toxic, biocompatible, and biodegradable properties. It contains amino ($–NH_2$) and hydroxyl (–OH) groups that enhance its adsorption capabilities and offer potential sites for chemical modification. Because of these attributes, chitosan is an excellent candidate for use as a support material for photocatalysts in the degradation of pollutants. In the upcoming sections, we will explore recent developments in utilizing chitosan as a biopolymer matrix for immobilizing photocatalysts. The following sections are summarized in Table 6.

3.2.1 Adsorption role in efficiency

TiO_2(P25) is widely used as a photocatalyst in wastewater treatment. However, its removal from the treated water generates high operating costs and induces secondary pollution. Therefore, immobilizing TiO_2(P25) or other photocatalysts on various substrates is an effective strategy. Immobilization on the biopolymer chitosan (CS) is reported since several years. Recently, Ikhlef-Taguelmimt et al. [14], dealt with the immobilization of TiO_2(P25) in chitosan film by using the cross-linking method by using NaOH (2 M). The ratio CS/TiO_2 was fixed to 2. They showed that this immobilization did not change the chemical structure of TiO_2(P25) which stayed uniformly dispersed in the composite. Adsorption of pollutant was then conducted at $T = 25$ °C at pH = 4 but results showed an absence of adsorption of **TC** on the film which was attributed to the neutral form of **TC** at pH = 4 whereas point of zero charge (pH_{pzc}) of TiO_2(P25)/chitosan film is 8.3. Thus, no direct photolysis can be performed. However, they achieved an 87% removal efficiency of **TC** under UV-light irradiation. It is also the case for other multicomponent photocatalysts. For example, a $FeNi_3$/chitosan/bismuth (III) oxyiodide (BiOI) photocatalytic nanocomposite has been prepared following a multi-step process starting with the formation of $FeNi_3$ NPs followed by their coating with chitosan and then impregnation with BiOI [64]. FESEM images evidenced that the surface of the composite consisted of small particles with irregular shapes and is a rough and highly porous medium which is known to favor pollutants degradation. However, CS hydrogels/beads, when used alone as a support, have several limitations (poor stability in relation to pH and low mechanical resistance). Consequently, much research focuses on combining CS with other polymers (such as PVA, alginate and others) to overcome these limitations. Consequently, various composites have been prepared as followed. In a study [60], the authors discussed biocompatible and structurally stable TiO_2/PVA-CS composite beads with sizes ranging from 1.5 to 3 mm. The combination of polyvinyl alcohol and chitosan (PVA-CS) was found to enhance the hydrophilicity, mechanical properties, and biocompatibility of the composite compared to the

Table 6 Summary of Chitosan based photocatalysts regarding their structural properties, photodegradation efficiency and reusability

References	Photocatalyst material Irradiation power	Photodegradation ROS and holes mineralisation	Recycling/activity/method
[14]	TiO_2(P25) UV-light irradiation film	87% deg. **TC**	52% to 58% **TC** deg. after the fourth cycle (by washing the film with a 1 M NaOH solution before each cycle)
[60]	TiO_2/PVA Beads (1.5 to 3 mm) UV-C irradiation	100%, 54% and 89% deg. **MNZ**, **CEF**, and **TC** (10 mg L^{-1}) $^{\cdot}OH$ radicals 31%, 66%, and 76% mineralisation	Three cycles of recycling
[61]	Ag/TiO_2 3D printed scaffolds UV–Vis light irradiation	100% deg. **AMX** (0.1 mM) in 90 min	80% **AMX** deg. after three cycles
[62]	TiO_2/GO UV-A irradiation conditions (60W)	95% deg. **CFX** in 1 h	95% deg. **CFX** after four cycles
[63]	Chitosan-TiO_2–ZnO over graphene UV-light irradiation	97% deg. **TC** in 3 h (20 mgL^{-1}) $^{\cdot}OH$ radicals	No
[64]	$FeNi_3$/chitosan/BiOI simulated sunlight generated by a xenon lamp (500 W)	100% deg. **MNZ** in 200 min (20 mgL^{-1}) h^+ and $^{\cdot}OH$ radicals mineralized by-products	Reused six times (magnetic separation)
[65]	Ag_3PO_4-$FeTiO_3$/glycol chitosan composite visible-light irradiation (Xe lamp, 400W)	99% deg. **MNZ** in 25 min (30 mg L^{-1}) $^{\cdot}OH$ radicals	89% deg. after five cycles
[66]	Phytochemically stabilized chitosan encapsulated Cu and Ag nanocomposites UV-light irradiation (high-pressure mercury lamp, 250 W)	84% in 70 min (Cu) and 97% in 40 min (Ag) deg. **CXM** (50 mg L^{-1}); antibacterial action $^{\cdot}OH$ radicals	No
[67]	$ZnFe_2O_4$@Chitosan solar simulator (LSO1O6, 150W Xe light source)	100%, 94% and 83% deg. **CIP**, **AMP**, and **ERY** (5 mg L^{-1}) $^{\cdot}OH$ radicals	> 90% after 15 cycles (magnetic separation)

individual components. The study demonstrated that TiO_2/PVA-CS composite beads exhibited a maximum adsorption capacity for various antibiotics, reaching up to 75% in the best case. The authors suggested that pollutant adsorption on the composite was primarily driven by chemisorption due to the relatively low porosity of the composite. Specifically, the pH at the point of zero charge (pH_{zpc}) for the composite was measured at 5.82, which was similar to the pH at which pollutants are considered to be in their neutral form (operating pH of 6–7). Under these conditions, chemical adsorption is favored. In addition, the hydroxyl groups of PVA and the amino/hydroxyl groups from CS contributed to the chemisorption of pollutants.

An alternative strategy to enhance the adsorption properties of chitosan-based materials is to incorporate graphene into the composite ZnO-TiO_2-CS. Graphene is known for its large surface area, theoretically approximately 2600 m^2 g^{-1}. For instance, in a study by M. Fattahi et al. [63], it was demonstrated that the use of chitosan alone resulted in a 10% increase in the degradation efficiency of tetracycline. However, when 10 wt.% of the entire composite, which includes graphene, was added, the efficiency in the degradation of tetracycline improved by an additional 10%. This enhancement was attributed to the higher adsorption surface area provided by the graphene sheets, as evidenced by N_2 adsorption experiments using the BET (Brunauer–Emmett–Teller) and BJH (Barrett–Joyner–Halenda) methods.

Furthermore, an innovative composite material composed of Chitosan/Ag/TiO_2 and 3D printed scaffolds was described in a study [61] for enhancing the adsorption of drugs on the photocatalyst. The use of 3D printing technology offers the advantage of obtaining materials with well-defined geometries and eliminates the need for a cross-linking agent (Fig. 6). The study demonstrated that chitosan hydrogel can be effectively 3D printed into a stable form. This printed hydrogel was then used as a support for the Ag/TiO_2 photocatalyst. Scanning electron microscopy (SEM) images confirmed the 3D structure of the material, which consisted of a regular lattice with filaments approximately 100 nm in thickness.

3.2.2 Improving photocatalytic efficiency in chitosan-based materials

Bergamonti et al. [61] reported an interesting approach to reduce the band gap of TiO_2 photocatalyst was explored,

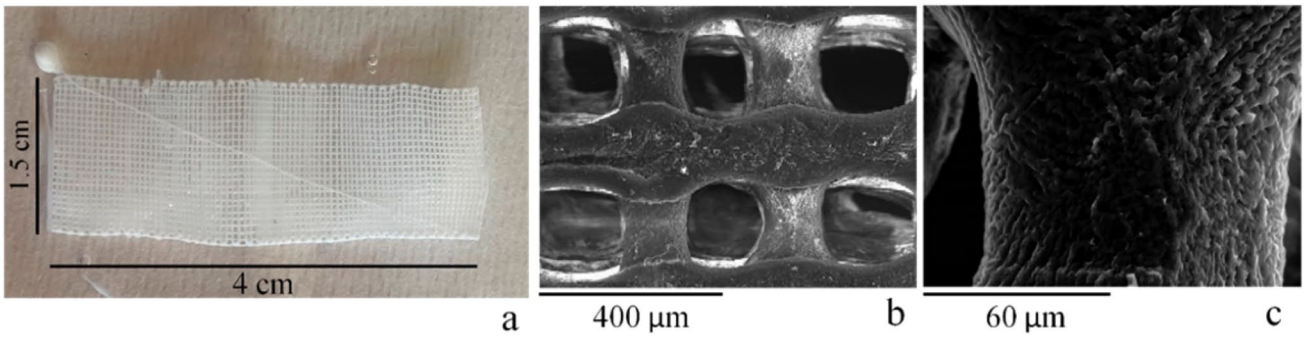

Fig. 6 Chitosan 3D printed scaffold: **a** picture; **b** SEM image; **c** SEM image of a filament (1000×). Reproduced from [61], under the terms and conditions of the Creative Commons Attribution (CC BY) license

with the introduction of Ag NPs onto a TiO_2/chitosan scaffold. Notably, the Ag NPs not only contributed to the photocatalytic activity but also improved the mechanical properties of the chitosan matrix. The chitosan/Ag/TiO_2 3D printed scaffolds were specifically designed for the photocatalytic degradation of **AMX** under UV–Vis light irradiation. Remarkably, this antibiotic was completely removed within just 90 min of irradiation. It was observed that the photocatalytic activity achieved with this composite was comparable to that of pure TiO_2, indicating its potential for efficient photocatalytic degradation applications. In fact, throughout the literature, TiO_2 is commonly used as the principal semiconductor compound for photocatalysis, and there is ongoing research to reduce the band gap of TiO_2 to enhance photocatalytic efficiency. For instance, Erim et al. [62], reported the development of a TiO_2/GO/chitosan composite. This composite was prepared by impregnating doped graphene oxide (GO) into a TiO_2 solution and chitosan biopolymer matrix. The researchers applied this composite for the degradation of **cefixime trihydrate** (**CFX**) under high UV-A irradiation conditions (60W, four lamps). The experimental results demonstrated that the TiO_2/GO/chitosan composite exhibited impressive degradation efficiency, achieving a removal rate of *ca* 95% within just 60 min under optimized conditions. This highlights the potential of the composite for efficiently degradation of **CFX** when exposed to high-intensity UV-A irradiation. Following the same strategy, graphene has also been added to TiO_2–ZnO/CS composites [63]. After optimizing conditions (testing different pH, initial **TC** concentration, catalyst dosage), the best material led to 97% in the degradation of tetracycline under UV light after 3 h at pH = 4 with a tetracycline concentration of 20 mg L^{-1} and catalyst dosage of 0.5 g L^{-1}. It is among the best results by comparison with other previously reported works dedicated to **TC** degradation with various photocatalysts.

Other authors [60] studied a PVA–CS–TiO_2 polymer blend for the removal of three model antibiotics (**metronidazole** (**MNZ**), **ceftiofur** (**CEF**), and **TC**) through both photocatalytic and adsorptive processes (Fig. 7). They conducted these removal experiments using a UV reactor system with 32 W UV-C power. They observed that the hydrophilic antibiotic **MNZ** was degraded more rapidly compared to the hydrophobic **CEF** and **TC** drugs. The maximum removal rates achieved for **MNZ**, **CEF**, and **TC** at 10 mg L^{-1} concentrations were almost 100%, *ca* 54%, and 89%, respectively. This difference in activity is attributed to the reactivity of $OH^{\cdot}$ radicals, which react more rapidly with electron-rich carbon–carbon double and triple bonds compared to aliphatic compounds. The authors also noted that mineralisation improved gradually with the recycling of the composite, although the polymer partially decomposed as well. Specifically, they found TOC removal rates of 31% for **CEF**, 66% for **TC**, and 76% for **MNZ** after three cycles of recycling.

Moreover, in the case of the $FeNi_3$/chitosan/BiOI nanocomposite reported by Arghavan et al., the authors showed it was an efficient photocatalyst for **MNZ** degradation under simulated sunlight after studying degradation kinetics and effects of physicochemical parameters [64]. Its use with a dose of 0.04 g L^{-1} led to 100% degradation for a 20 mg L^{-1} **MNZ** solution at pH 7 in 200 min and the final by-products were mineralized products. It has been demonstrated that $FeNi_3$ particles located in the nanocomposite core do not contribute to the photocatalytic activity, only BiOI with its characteristic narrow bandgap does. The mechanistic studies of **MNZ** photocatalytic degradation evidenced the formation of highly oxidizing radicals and involves sequential transformation into the following four compounds: 2-(4-ethyl-2-hydroxy-1*H*-imidazol-1-yl) propionic acid, (2-oxopyrrolidin-1-yl) acetic acid, 2-methyl-2-pentenal, and 3-methyl-1- butanol, ultimately followed by complete mineralisation [64].

Chitosan has also been conjugated with a hydrophilic ethylene glycol function to provide Glycol Chitosan (GC) as a new matrix with a better solubility in water which can improve the separation of photocarriers and the photocatalytic stability [65]. For example, Ag_3PO_4-$FeTiO_3$/glycol

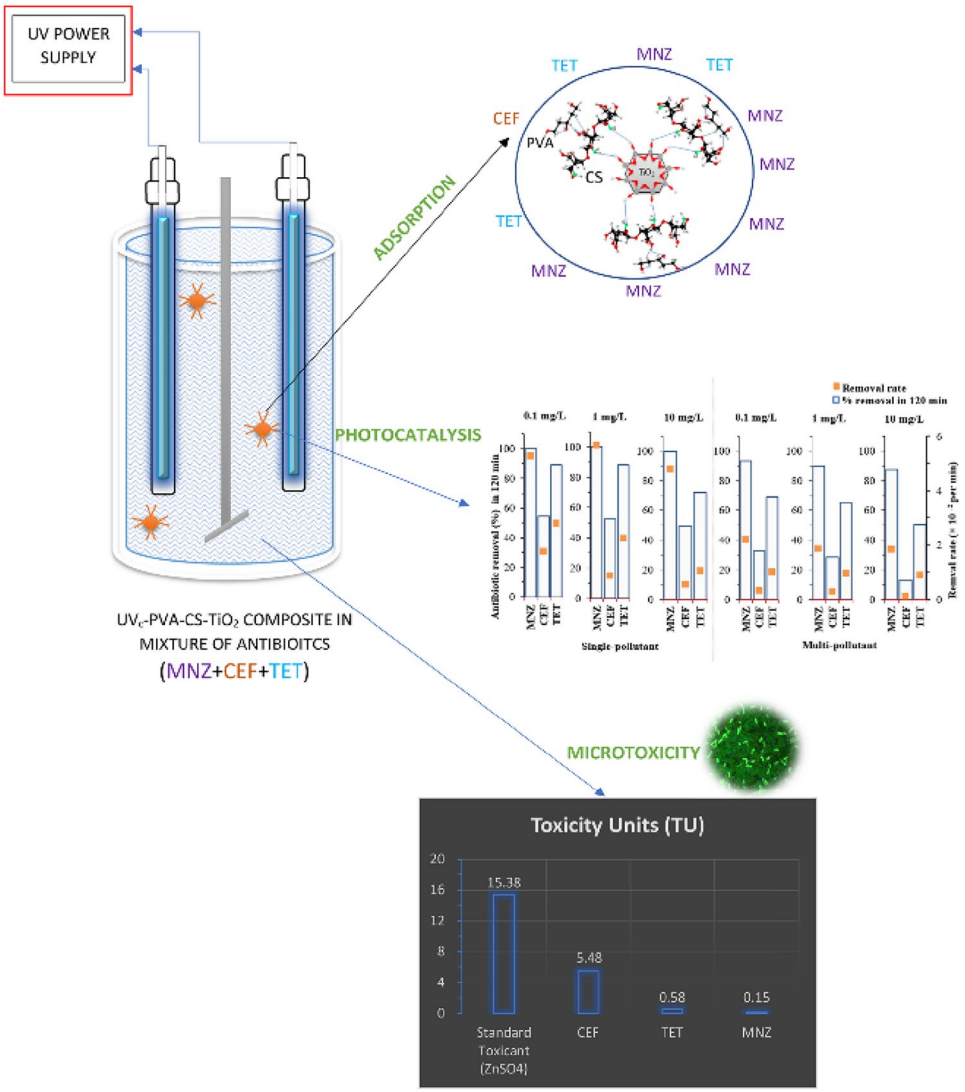

Fig. 7 Photodegradation system of three antibiotics (**MNZ**, **CEF** and **TZ**), as explored by [60]. Reproduced under the terms and conditions of the Creative Commons Attribution (CC BY) license

chitosan has been prepared using pyrolysis method to afford uniformly dispersed nanocomposites due to electrostatic interaction between GC and Ag_3PO_4-$FeTiO_3$ according to FESEM images, with a crystal size of 55.59 nm [65]. The Ag_3PO_4-$FeTiO_3$/glycol chitosan composite can degrade **MNZ** under visible-light irradiation in 25 min with 99% efficiency due to its strong ability to separate e^-/h^+ pairs. It is significantly more efficient than Ag_3PO_4-$FeTiO_3$ and $FeTiO_3$ materials which display respectively 72% and 35% photodegradation percentages in the same conditions. The antimicrobial and antifungal properties of the Ag_3PO_4-$FeTiO_3$/glycol chitosan composite have also been demonstrated.

Introducing some additives to the formulation of the photocatalytic composite has also been investigated to improve the photocatalytic properties. For example, R. Sharma et al. have added extracts of the *Potentilla astrosanguinea* plant when preparing chitosan encapsulated Cu and Ag nanocomposites [66]. The size of the NPs depends on the concentration of the plant extracts and the presence of different types of polyphenolic phytochemicals lead to the bio-reduction of Cu and Ag ions to Cu and Ag NPs, which may explain their higher activity. Advantages of such a formulation is that it is fast, energy-efficient, inexpensive, and environmentally benign. Thus, the silver and copper-based materials can degrade **cefuroxime axetil** (**CXM**) under UV-light exposure with degradation percentages of 97% and 84% within 40 and 70 min, respectively. These nanocomposites display also antibacterial action against Gram-positive, Gram-negative, and fungal pathogens in addition to photocatalytic activity.

3.2.3 Recovery and reusability

Again, in an industrial context, the durability, stability, and recyclability of photocatalysts are crucial factors for their practical application. As one example, the Ag_3PO_4-$FeTiO_3$/

glycol chitosan composite can degrade **MNZ** under visible-light irradiation in 25 min with *ca* 99% efficiency even after five times thanks to its great structure that can resist photo-corrosion [65]. For instance, Ikhlef-Taguelmimt [14], subjected the chitosan/TiO_2(P25) film to four cycles of use under UV irradiation. Before each cycle, the film was washed with a 1 M NaOH solution. This washing step prevented the saturation of the film by degradation products and also improved photocatalytic performance. As a result, the removal of **TC** increased from 52 to 58% after the fourth cycle. In another study, authors reported the outstanding recycling performance of the TiO_2/GO/chitosan composite [62] under UV-A irradiation. Interestingly, there was no loss of photocatalytic activity even after four cycles of use. For the Chitosan/Ag/TiO_2 3D printed scaffolds [61], they were reused three times. Between two cycles, the scaffold was washed with distilled water. Remarkably, the best composite CS/Ag100/TiO_2 still achieved a photodegradation rate of up to 80% for **AMX** after three cycles. This demonstrates the recyclability and durability of these materials for multiple applications. The preparation of $ZnFe_2O_4$@Chitosan with a crystallite size of 35.14 nm has also been reported for the recycling of the photocatalyst by magnetic separation [67]. Ferrites enables photocatalysis in the visible-light region because of their relatively narrow bandgap while displaying magnetic properties and the use of chitosan helps reduces particles aggregation and thus their recovery from solution. Zinc ferrite immobilized on chitosan was used for the photodegradation of **CIP**, **AMP** and **erythromycin** (**ERY**) in aqueous solution with respective efficiencies of around 100%, 94%, 83% and displayed high stability since no significant capacity loss was observed even at the 15th regeneration cycle. Between each cycle, the photocatalyst was regenerated by washing it with a mixture of ethanol and 0.1 M HCl (3:2) [67]. Following the same strategy, $FeNi_3$/chitosan/BiOI nanocomposite has been successfully recycled for six consecutive photocatalytic cycles and there was only a 7% reduction in **MNZ** removal efficiency at the end of the cycles [64].

3.3 Cellulose and biopolymers extracted from plants as matrices

3.3.1 Cellulose based hybrid photocatalysts

Chitosan could be also coupled with oxidized cellulose to form composite material. For example, Honarmand et al. obtained chitosan NPs after deproteination, demineralisation and deacetylation of shrimp wastes and microcrystalline cellulose aldehyde by sodium periodate oxidation of the 1,2-diol groups of cellulose extracted from barely wastes [68]. The two polymers were then covalently linked by a condensation reaction and Ni/NiO NPs from *Calotropis procera* wood powder were incorporated to prepare Chit-Cell@Ni/NiO bio-nanocomposite. Incorporating of Ni/NiO into the chitosan/cellulose matrix increased the specific surface area and pore size of catalyst. The catalytic performance of the Chit-Cell@Ni/NiO was evaluated in the aqueous photodegradation of **CIP** under direct sunlight. After 20 min, *ca* 92% of **CIP** was degraded at pH 6 and in presence of 0.2 g L^{-1} Chit-Cell@Ni/NiO. In the same time, the degradation efficiency for the Ni/NiO was 59% only, underlined once again the synergy existing between the photocatalyst and the supporting matrix. Radical experiments indicated that h^+ was the main active species, followed by $^{\cdot}OH$ radical, and then $O_2^{\cdot -}$ radical. Moreover, the catalyst could be reused at least 2 times and based on LC–MS result the pathways of the **CIP** degradation using Chit-Cell@Ni/NiO was proposed.

To remove **CIP** from water, Huang et al. reported another system, based on the preparation of an alkali-cooking modified rice straw fibers (AMSF) [69]. At 35 °C and pH 6, this biosorbent has a maximum adsorption capacity of 93.5 mg g^{-1}. To develop photocatalyst able to degrade the adsorbed **CIP**, TiO_2 hydrogel layer was coated on the surface of AMSF (TiO_2@AMSF). At 35 °C, pH 6 and with a **CIP** concentration of 50 mg L^{-1}, **CIP** degradation was of 61% and 45% after 450 min under UV irradiation and natural light, respectively. In the presence of others fluoroquinolone, **moxifloxacin hydrochloride** and **levofloxacin hydrochloride** (the pure S-isomer of **OFX**), TiO_2@AMSF was half as active after 1 h of reaction under natural light and the quantity of degraded **CIP** remains at approximately 48 mg g^{-1} thereafter. Authors observed that the number of TiO_2-gel layers coated had not influence on **CIP** removal under natural light, but the recyclability of TiO_2@AMSF was closely connected with this parameter. Indeed, after regeneration of the catalyst by UV irradiation at the end of each cycle, the amount of **CIP** removal quantity by TiO_2@AMSF decreases by around 64% after three cycles when the catalyst contains one TiO_2-gel layer, whereas the loss of activity is only 29% when TiO_2@AMSF has three TiO_2-gel layers. One can reasonably rely this on the faster saturation of the system in the case of one TiO_2-gel layer, in the same line with was underlined in the biochar section.

In another way, Zeghioud et al. impregnated a mixture of SiO_2 and TiO_2 NPs on cellulosic paper to realize the photocatalytic degradation of three quinolone antibiotics, **flumequine** (**FLU**), **oxolinic acid** (**OXA**) and **nalidixic acid** (**NXA**) under UV-light irradiation (365 nm) in mono-, binary and ternary compound systems [70]. All the tests were performed in a closed-loop step photo-reactor at pH 7 in the presence of 2.6 g L^{-1} catalyst dosage. In the mono-compound system, all the antibiotics were completely degraded after 4 h. However, the degradation of **FLU** was much faster, followed by that of NA, while **OA** degradation was the slowest. The authors explained this result by the fact

that **OA** has a major hemolytic effect and is more photostable than **FLU** and **NA**. The mineralisation of **OA**, **FLU** and **NA** achieved 65%, 57% and 43% after 6 h, respectively, with a pseudo first order kinetics. The rate of degradation of all pollutants decreased when photodegradation was carried out in binary or ternary compounds system, which was due by the competitive adsorption of antibiotics on the available reactive sites of photocatalyst surface. Except for **FLU**, **OXA + FLU** and **NXA + FLU** systems in which h^+ was predominant, the $^{\cdot}OH$ radical is the most species involved in the photodegradation of antibiotics.

If cellulosic paper is a very convenient form to recover the photocatalyst system, cellulose acetate (CA) could also be used to develop composite membranes (Fig. 8) used to aqueous photodegradation of **sulfadiazine** (**SUL**) and **CIP** [71]. Thus, CA was mixed with Fe-complex in a weight ratio of *ca* 12% to obtain a photo-Fenton catalyst (Fe-complex/CA) using casting method. Under visible-light irradiation (400–780 nm) and in presence of low of hydrogen peroxide concentration (0.039 mol L^{-1}), a 96% photodegradation of **SUL** was reached after 1 h, with first order kinetic ($k = 0.053$ min^{-1}). Tests carried out on methylene blue showed that the photocatalyst can reused four cycles with a slight decrease in activity.

Other authors also used casting method to immobilize bismuth oxybromide (BiOBr) particles inside the CA polymer matrix [72]. The efficiency of the BiOBr/cellulose acetate (BCA) composite films in photodegradation of **CIP** was evaluated using compact fluorescent light (400–750 nm). The effect of various operational parameters such as BiOBr loading (10, 20 30 and 40 wt%), film size (1 × 2–4 × 4 cm), and pH (3–11) have been studied. Using BCA-30 composite film with a size of 3 × 3 cm^2, **CIP** was degraded at 71% after 360 min at pH 7.1 and 25 °C, with h^+ and $O_2^{\cdot -}$ radical were the main species driving the photodegradation. Reaction rate was found to be of pseudo first order with $k = 0.00274$ min^{-1} and the efficiency of BCA-30 composite film decreased from 70.9 to 59% after the first cycle. The authors attributed this deactivation to the presence of traces of **CIP** or its intermediaries on the active sites of BCA-30 composite film. However, the activity of the membrane stayed stable between the third and tenth cycles. This study, as the previous ones underlined the process ability of the systems based on cellulose derivatives coupled with good efficiency, however, avoiding the saturation of active sites remained a challenge for applied solution development. Using $BiVO_4$ as the catalyst, Gao et al. impregnated $BiVO_4$/polyaniline (PANI)/Ag on 3D lignosulfonate composited poly(vinyl

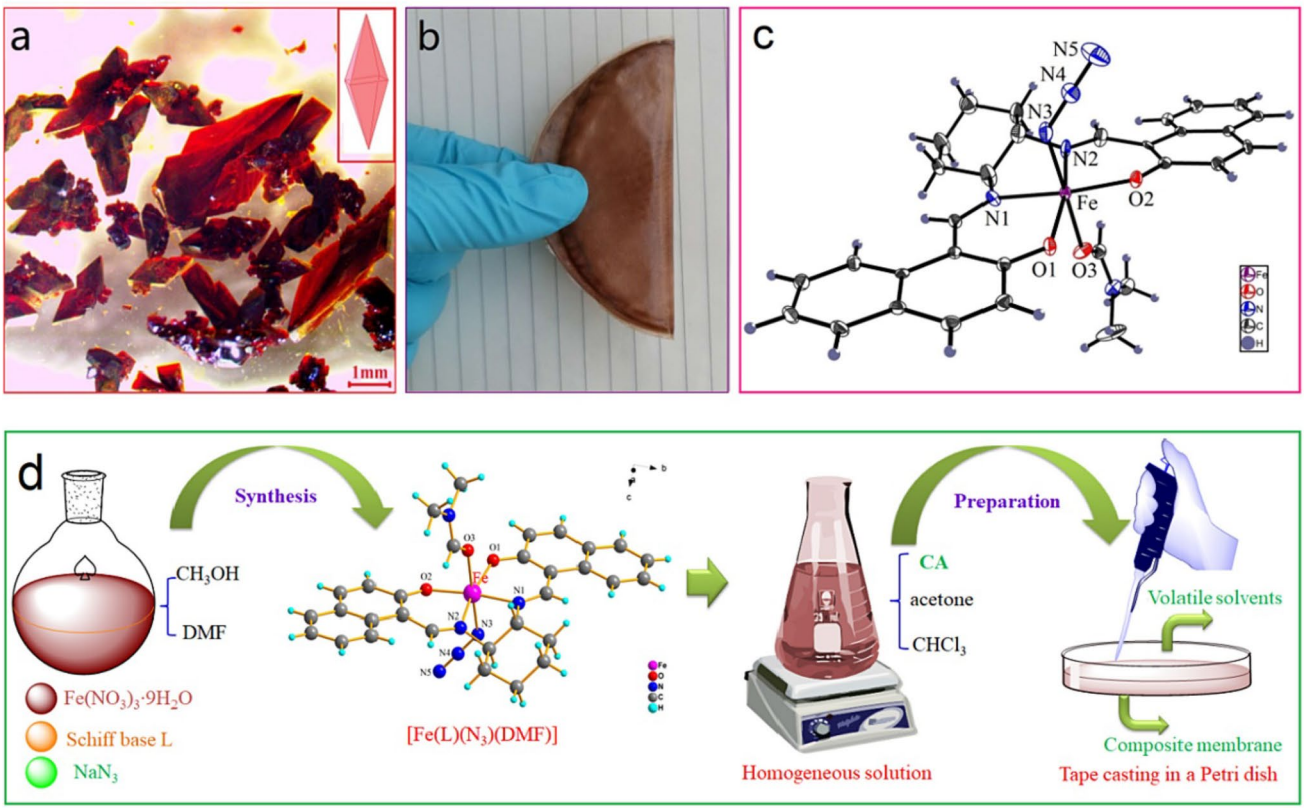

Fig. 8 Preparation (**a**, **b**, **d**) and crystal structure (**c**) of the photocatalyst system applied to cellulose acetate [71]. Reproduced with permission from the journal

formal) (PVF) sponge. Incorporating of lignosulfonate in PVF sponge increase its specific surface area of material, without changed the stability [73]. Moreover, the presence of oxygenated functional groups in the lignosulfonate structure improved the capacity of PVF sponges to absorb organic contaminants such as fluoroquinolone antibiotics (FQs). The photocatalyst PLS/$BiVO_4$-PANI-Ag was then used to adsorption-photodegradation of five FQs under visible light, using **norfloxacin** (**NOR**) like model molecule. In batch treatment system, At pH 6, PLS/$BiVO_4$-PANI-Ag obtained with a mas ratio of $BIVO_4$:PANI:Ag of 1/0.025/0.013 the photodegradation of NOR reached 95% after 120 min, with mineralisation efficiency of 55% and a first order kinetic ($k = 0.0190$ min^{-1}). In the same conditions, the others FQs studied (**OFX**, **fleroxacin** (**FLE**), **ERF** and **CIP**) were eliminated by over 91%. The h^+ species were found to be the main driving force for the **NOR** photodegradation and the degradation pathways included defluorination, decarboxylation and destruction of piperazine ring. Furthermore, the adsorption and photodegradation efficiencies of PLS/$BiVO_4$-PANI-Ag photocatalysts decreased slightly during the four reutilisations. In addition to the experiences in batch system, the authors realized a number of **NOR** degradation tests in a continuous dynamic processing system. With this system, when the initial concentration of **NOR** was 0.1 mg L^{-1}, the rate of degradation was 80% after 5 h. At **NOR** concentrations of 0.2 and 0.3 mg L^{-1}, the PLS/$BiVO_4$-PANI-Ag activity decreases to 60% and 70%, respectively.

For the same semiconductor system ($BiVO_4$), different weight ratio (1%, 5% 10% and 15%) of cellulose fibers obtained from bamboo was added during the preparation under ultrasound of bismuth vanadium oxide quantum dots ($BiVO_4$ QDs) [74]. The presence of cellulose fibers in structure of $BiVO_4$ QDs increase their stability and the electron transfer, and therefore the photocatalytic activity, because chemical bonds was formed between $BiVO_4$ QDs and cellulose fibers. During the degradation of **TC** under visible light irradiation, all composite materials was more active than pure $BiVO_4$ QDs, evidencing once again the synergy arising from co-used of semiconductor photocatalyst and biopolymer. Under visible light, the best result was obtained with 5 wt% cellulose fibers (BCF-3), with an approximately 67% photodegradation after 90 min, and a rate constant (pseudo-first order kinetic) was 11.3 times higher than pure $BiVO_4$ QDs. BCF-3 was recycled two times without loss of efficiency and the active species trapping tests were indicated the h^+ was the major species involved in the photodegradation.

In another example, Nahi et al. incorporated zinc oxide (ZnO) with nanocellulose (NC) obtained from sugarcane bagasse [75]. The photocatalyst ZnO/NC was used to degrade **ERF** under the visible light. The authors underlined the importance of the modification of ZnO's band gap to explain their results. However, they did not explain that fact. One can hypothesize that the preparation allowed new interactions and a synergy between ZnO and NC. Indeed, the preparation of this composite implied sonication and heat (100 °C during 1 h) that changed the morphology of the composite relative to each moity as its FTIR spectrum and the material showed an improved efficiency in the **ERF** degradation by comparison of both moieties taken apart. At pH 5, with a ZnO/NC concentration of 0,20 g L^{-1}, the equilibrium was attained at 120 min and a maximum degradation efficiency of 97% was observed. In parallel, the activity of NC and pristine ZnO was inferior under the same conditions.

To summarize, cellulose based matrix has been successfully used to improve photocatalyst efficiency, notably by increasing the specific surface area and pore size of catalyst, their adsorption capacity and in several cases allowing a synergy between support material and photocatalyst. The systems and their main results discussed above together with those of the next sections are summarized in Table 7. However, in equilibrium has to be found between drug removal thanks to adsorption (as the adsorption capacity decrease in time because of active site saturation) and to photodegradation as this last mechanism also need interaction between antibiotic and photocatalyst system to be efficient. Thanks to their chemical structure, biopolymer-based matrix allows such interaction but can also, as evidenced in the last study reported here, increase the electron transfer, and therefore the photocatalytic activity thanks to chemical bonds.

3.3.2 Cellulose doped semiconductors photocatalysts

To improve the photocatalytic activity, enhancing to visible region the band gap of the semiconductor is also of upmost importance.To dope the photocatalyst, as outlined for alginate-based systems, is to couple it with reduced graphite oxide (rGO) [76]. The superior electrically conductive of rGO can function as an electron collector and transporter to lengthen the charge-carrier lifetime, leading to improvements in the photocatalytic performance. Thus, Thanh Nhi et al. combined copper oxide NPs (Cu_2O) with rGO and Vietnamese traditional paper (VTP) to develop a flexible, highly porous and floatable photocatalyst. Catalyst membrane Cu_2O/rGO/VTP was then used in the photocatalytic p degradation of **CIP** under solar light irradiation. The VTP support facilitates the approach of the **CIP** to the catalyst's active sites because it is composed of microfibrillated cellulose. Moreover, the functional groups of cellulose and rGo increased the **CIP** adsorption. A **CIP** degradation of about 82% was observed at pH 7, with a pseudo first order kinetics ($k = 1.16873$ min^{-1}). The photocatalyst was also reused 5 times with ~ 20% activity loss, after the last cycle. Among the several strategies developed to improve the TiO_2 photocatalytic efficiency, especially for allowing utilization of

Table 7 Selected examples of the application of cellulose-based photocatalysts, summarizing some operational features

Reference	Matrix	Maximal removal efficiency							Recyclability	
		Photo catalyst (PC)	[PC] (g L^{-1})	Antibiotic (AB)	[AB] (mg L^{-1})	Irradiation	Time (min)	AB removal (%)	Nb of cycle	Final efficiency (%)
[68]	Chitosan/cellulose	Ni/NiO	0.20	**CIP**	10	Sunlight (260–280 Klux)	20	92	3	85
[69]	AMSF	TiO_2	0.20	**CIP**	50	UV	450	61	N S	N S
						Natural light		45	3	32
[70]	Cellulosic paper	TiO_2	2.60	**FLU**	5	UV (365 nm)	240	100 (57)[a]	N S	N S
				OA				100 (65)[a]	N S	N S
				NA				100 (43)[a]	N S	N S
[71]	Cellulose acetate	Fe-complex	0.50	**SUL**	10	Visible light (400–780 nm)	60	95.70[b]	4[c]	86.50[c]
[72]	Cellulose acetate	BiOBr	N S	**CIP**	20	Visible light (400–750 nm)	360	70.90	10	59
[73]	PLS/PANI	$BiVO_4$	0.67[d]	**NOR**[d]	8,0	Visible light ($\lambda > 420$ nm)	120	95 (55)[a]	5	80
				OFX[d]	9.0			92	N S	N S
				FLE[d]	9.2			92	N S	N S
				ENR[d]	9.0			95	N S	N S
				CIP[d]	8.2			98	NS	NS
			N S	**NOR**[e]	0.1	LED light	1800	80	N S	N S
[74]	Cellulose fibers	$BIVO_4$	0.20	**TC**	10	Visible light ($\lambda > 420$ nm)	90	~67	3	~66
[75]	Cellulose	ZnO	0.20	**ERF**	7	Sunlight	120	97	N S	N S
[76]	Vietnamese traditional paper	Cu_2O/rGO	2	**CIP**	10	Solar light	90	~82	5	~62
[77]	Cellulose acetate	Au Ag/TiO_2	N S	**TC**	5	Visible light ($\lambda > 420$ nm)	120	77[d]	N S	N S
								89[e]		

NS: not specified

[a]() antibiotic mineralisation in %

[b]Test carried out with a hydrogen peroxide concentration of 0.039 mol L^{-1}

[c]Tests carried out with methylene blue. During the first cycle the degradation was 93%

[d]Photodegradation realized in batch system

[e]Photodegradation performed in dynamic system (with 0.5 g of photocatalyst for reference [67])

visible light by this oxide, the deposition of noble metal noble metals (such as Au and Ag) NPs on TiO_2 materials will enhance the possibility to use visible light [78]. Thanks to their strong surface plasmon resonance (SPR) generated by the collective oscillation of conductive electrons, Au NPs will allow a photoactivation of the process in the visible range and will inhibit the recombination of photogenerated electrons and holes, thus increasing the efficiency of the photocatalyst. In this framework, the work of Li et al. [77] can be cited. Indeed, the authors described a bimetallic Au/Ag decorated TiO_2 nanorods incorporated into a cellulose acetate membrane as photocatalyst support. They underlined that the material with the following stoichiometry $Au_{0.1}Ag_{0.9}/TiO_2$ nanorods and a loading weight percentage of 1.5% on cellulose acetate membrane, so called $Au_{0.1}Ag_{0.9}/TiO_2$/CA-1.5, was the most efficient to degrade **TC** (more than the analog systems involving only one noble metal, Au or Ag), with a degradation rate up to 90% in the presence of 20 mg mL^{-1} of tetracycline, under visible light irradiation for 120 min. Increasing the loading amount decreased the efficiency, this being be probably due to a non-optimum dispersion of the photocatalysts in the cellulose acetate matrix. In addition, they have shown that porosity and pore radius were higher than in pure cellulose acetate membrane, this evidencing that hybridization could facilitate water permeation and thus dynamic adsorption of **TC**. The importance of the contact between the antibiotic and the catalyst was moreover evidencing when the $Au_{0.1}Ag_{0.9}/TiO_2$/CA-1.5 system was investigated under dynamic continuous conditions, for which the **TC** degradation rate was much higher than that in the static degradation system, this increment being attributed to the increased contact between **TC** and catalyst in the continuous degradation experiment. Moreover, this system, thanks to Ag NPs, possess also good antibacterial activity against *E. coli*, due to the intrinsic antibacterial property of silver but, also, to ROS generation as the viability of *E. coli* was even decreased to 1.5% when $Au_{0.1}Ag_{0.9}/TiO_2$/CA-1.5 membrane was exposed to visible light for 30 min.

3.3.3 Oxidized cellulose

In another system, Au and TiO_2 and cellulose were also associated, without any Ag involvement, with also a good efficiency toward **tylosin** (**TYL**) degradation [79]. In this study, carboxylated cellulose beads embedded with Au-doped TiO_2 NPs (Au/TiO_2-CCBs) were used. The cellulose was oxidized into carboxylated cellulose thanks to a 2,2,6,6-tetramethylpiperidin-1-yl)oxidanyl (TEMPO) mediated oxidation. The authors anticipated that the presence of carboxyl groups on cellulose will allow the formation of hydrogen bond between the cellulose and hydroxyl groups, formed by the dissociation of water molecule on the surface of TiO_2 in Au-doped TiO_2 NPs. In addition, as in neutral pH solution, **TYL** is mainly positively charged while the carboxyl group are negatively charged, this should also improve the adsorption of the antibiotic in water solutions through electrostatic interaction, and thus the photocatalytic efficiency of the composite catalyst. As expected, if pure carboxylated cellulose exhibited poor photocatalytic activity for **TYL** degradation under visible light irradiation for 180 min, the studied system has a removal rate up to 92%, this percentage being almost 2.4 times higher than that of bare TiO_2, in the same conditions in presence of Au/TiO_2-CCBs with Au (0.75%) doping (rate constant $k = 0.01382$ min^{-1}). This 0.75% doping amount was optimal, as, by increasing it (up to 1%), the degradation rate decreased to *ca* 53%. The possible formation of recombination center of electron–hole pairs under an excessive Au concentration was hypothesized to explain this.

Increasing the interaction between the photocatalyst and the support matrix trough TEMPO mediated oxidation of cellulose was also used recently for other photocatalytic semiconductors systems, such as bismuth-based ones. Bismuth oxyhalides composites, BiOX/BiOY (X, Y = Cl, Br, I), for example, have been associated with TEMPO-oxidized cellulose nanofiber, to degrade tetracycline hydrochloride under visible-light irradiation [80]. This association took advantage of very good photocatalytic activities of bismuth oxyhalides composites, even better than those of BiOX alone, and the easier separation and recovering of the photocatalyst by cellulose support. The best system, according to photocatalyst process efficiency (up to 91% of **TC** degradation after 60 min of visible-light irradiation), was the system BiOBr/BiOI in modified cellulose with a molar ratio of Br to I of 9:1. The high photocatalytic activity of BiOBr/BiOI/cellulose composites toward **TC** was attributed to the broad visible-light absorption, high migration efficiency of the electron–holes, short charge transfer distance and interfacial interaction of the system. Regarding this last point, the authors evidenced that interlaced BiOBr and BiOI nanoplates were inserted on the surface of the oxidized cellulose. Also, they underlined a shift of the O–H stretching absorption peaks in FTIR spectrum of the composite in comparison with the one of pristine oxidized cellulose, characteristic of a strong interaction between the hydroxyl groups of oxidized cellulose, BiOBr or BiOI particles through a hydrogen bond.

TEMPO-oxidized cellulose, under nanocrystal forms, was also used in CdS/MoS_2/Montmorillonite (Mt) hybrid in polyacrylamide-based hydrogel (PAM, * MERGEFORMAT Fig. 9), for **TC** photodegradation, in another recent study reported by Yue et al., in 2022 [15]. According to the authors, the oxidizing the cellulose will not only improve the dispersibility of the catalysts and the adsorption capacity of the hydrogel, thanks to its numerous negatively charged -COOH groups, but also enhance its mechanical properties. In the same way, the lamellar structure of Mt,

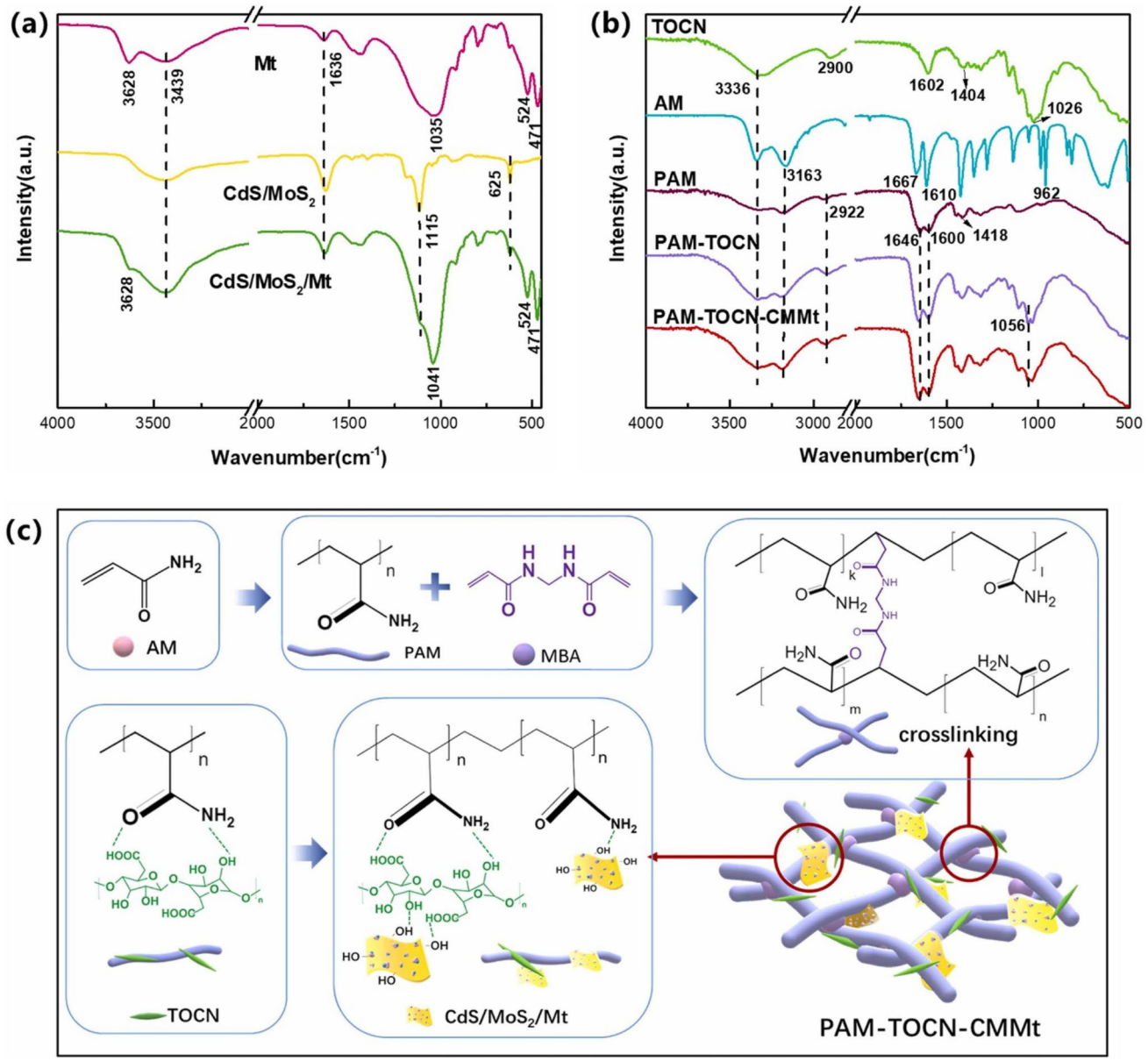

Fig. 9 Characterization (**a**, **b**) and preparation of the oxidized cellulose composite, prepared by Yue and collaborators [15]. Reproduced with permission from the journal

which contains a large number of hydroxyl groups, has the potential to become a bridge between the catalysts and hydrogels, underlying the importance of molecular interactions permitted by supporting materials in photocatalyst systems to enhance the photocatalytic efficiency. It was also evidenced that the whole system has the largest adsorption capacity, by comparison to other prepared hydrogel, this being explained, once again, by the formation of extra hydrogen bonds between oxygen atoms on Mt and hydrogen of hydroxyl group of the oxidized cellulose. Photoactivation of this system for 120 min under visible-light irradiation, allowed to remove up to 90% of **TC**.

However, TEMPO is not the only one oxidant used in this cellulose supported photocatalyst improvement domain. Indeed, sodium periodate ($NaIO_4$) mediated oxidation allow to form cellulose aldehyde. In this case, more than reinforcement of interaction of cellulose matrix with antibiotic or the photocatalyst, the main goal is to achieve the covalent attachment of the different moieties. For example, in 2022, Naeimi et al. [81], investigated a bentonite/cellulose/lead oxide system for photocatalytic degradation of **CIP** under sunlight at neutral pH. In this system, cellulose and bentonite were covalently attached through the formation of Schiff base ligand, thanks to prior oxidation by $NaIO_4$

into aldehyde of hydroxyl groups on the glucose units. This bentonite surface modification will, once again, enhance the interaction the support and active species as well as increase the adsorption capacity of bentonite, thanks to OH and CH groups bearing by the cellulosic polymer. The degradation of **CIP** reached for this system (with a concentration of 0.5 g L^{-1}), after 30 min of irradiation, *ca* 98% (rate constant $k = 0.1309\ min^{-1}$), compared to almost 82% (rate constant $k = 0.0569\ min^{-1}$) for bare PbO NPs in the same conditions i.e., ca. 2.3 times higher for the former than for the later. However, the concentration of the antibiotic seemed to be an important parameter as the degradation efficiency of **CIP** decreased for starting concentration equal or above 100 mg L^{-1}, this could be due to the high concentration of antibiotic in the solution that prevented sunlight from reaching to photocatalyst surface or a saturation of the actives sites at the surface of the photocatalyst system by the intermediate produced that will compete with **CIP**. The systems and their main results discussed in this section are summarized in Table 8.

3.3.4 Cellulose and metal organic frameworks

As it has been already underlined, a major problem with metallic semiconductor photocatalysts is that they have a large band gap and, hence, can be used only with ultraviolet irradiation. To decrease this band gap and use such photocatalyst under visible irradiation, another solution is the utilization of metal organic frameworks (MOFs). Indeed, in addition to their excellent properties, such as high porosity and high surface area, their absorption bands can be adjusted to the visible light as a large number of organic linkers are involved in their composition. In addition, a composite of adsorption-enrichment and in situ photocatalytic degradation of MOFs may greatly improve the pollutant removal performance [82]. The following section is summarized in Table 9.

For example, Xu et al. [83], loaded very recently cellulose flakes with Bi_2MoO_6 NPs prepared from a Bi-MOF (namely CAU-17 prepared by the reaction of 1,3,5-benzenetricarboxylic acid (H_3BTC) and $Bi(NO_3)_3.5H_2O$) and $(NH_4)_6Mo_7O_{24}.4H_2O$ with a Bi:Mo molar ratio of 2. This system (Mo-Bi-MOF), after 120 min of visible-light irradiation, degraded up to 86% of **TC** and 62% of **CIP** i.e., 1.2 and 1.8 times higher than the equivalent system without any MOF. This was even higher when the photocatalyst system was loaded on cellulose. Indeed, the photodegradation of **TC** by Mo-Bi-MOF loaded on cellulose (the weight percentage of cellulose to Mo-Bi-MOF being 10%) was equal to *ca* 89% just after 30 min and 72% after 90 min for **CIP**, the kinetic *k* values being 1.9 and 1.3 times higher, respectively, than those obtained for unanchored Mo-Bi-MOF. In addition, the 10% weight percentage of cellulose was found to be optimal

Table 8 Selected examples of the application of oxidized cellulose-based photocatalysts, summarizing some operational features

References	Matrix	Maximal removal efficiency				Irradiation	Time (min)	AB removal (%)	Recyclability	
		Photo catalyst (PC)	[PC] (g L^{-1})	Antibiotic (AB)	[AB] (mg L^{-1})				Nb of cycle	Final efficiency (%)
[79]	TEMPO-oxidized cellulose	TiO_2	50	**TYL**	20	Visible light ($\lambda > 420$ nm)	180	92	5	~92
[80]	TEMPO-oxidized cellulose	TiO_2	0.4	**TC**	20	Visible light ($\lambda \geq 420$ nm)	60	91	4	~86
[15]	TEMPO-oxidized cellulose	CdS/MoS_2/Mt	40	**TC**	20	Visible light	120	90	5	70.5
[81]	Oxidized cellulose/bentonite	PbO	1	**CIP**	10	Sunlight (260–280 Klux)	30	100	3	~96

Table 9 Selected examples of the application of MOF cellulose-based photocatalysts, summarizing some operational features

References	Matrix	Maximal removal efficiency							Recyclability	
		Photo catalyst (PC)	[PC] (g L^{-1})	Antibiotic (AB)	[AB] (mg L^{-1})	Irradiation	Time (min)	AB removal (%)	Nb of cycle	Final efficiency (%)
[83]	Cellulose	Bi_2MoO_6	1	**TC**	10	Visible light ($\lambda > 420$ nm)	180	89	4	83
				CIP				72		57
[84]	Cellulose	ZIF-67	0.6	**TC**	30	N S	30	~ 88	3	~ 82
[82]	CMC/β-CDP	MIL-101(Fe)	0.1	**TC**	50	Visible light	30	~85	3	N S

NS: not specified

as with the augmentation of the cellulose weight ratio above induced a decrease of the degradation efficiency, this indicating that too high quantities of cellulose probably interfere with the exposure of the photocatalyst to visible light.

However, cellulose, in the good proportion, enhanced the efficiency, once again, thanks to its hydroxyl groups acting as active adsorption sites. It was also underlined that cellulose improved the specific surface area, the dispersity of the semiconductor and facilitated charge transfer as the recovering of the systems after treatment by a simple sieving method.

Similar results have been obtained with a cellulose aerogel loaded with zeolitic imidazolate framework-67 (ZIF-67), ZIF-67 allowing to activate in presence of peroxymonosulfate (PMS that will generate, after interaction with irradiated ZIF-67, $SO_4^{\bullet -}$, one of radical species responsible for the degradation process) efficiently and degrade **TC** with degradation rate up to 80% within only 20 min [84]. In this study, the authors emphasized the role of the cellulose aerogel to shape MOFs and promote recycle efficiency after water treatment. This novel doping method increased the loading and dispersibility of ZIF-67, the porosity of the material being increased from 46% (pure cellulose aerogel) to 87%.

TC can be also efficiently degraded, under visible-light irradiation by a hydrogel associating carboxymethylcellulose (CMC), an iron-based MOF (namely MIL-101(Fe)) and poly(β-cyclodextrin) β-cyclodextrin (β-CDP) [82]. Here, because of its hydrophobic cavity, β-cyclodextrin (β-CD) can allow formation of inclusion complexes with a wide range of hydrophobic molecules (Fig. 10) and poly(β-cyclodextrin) (β-CDP) with high specific surface areas can be obtained by reacting β-CD with epichlorohydrin (EPI) in an alkaline medium. If, about 40% **TC** can be degraded by composite hydrogel of CMC/MIL-101(Fe)/β-CD after 30 min under visible light, approximatively 85% of **TC** was degraded by the CMC/MIL-101(Fe)/β-CDP composite hydrogel, this result being undoubtedly owed to the hydrophobic inner cavity of β-CDP and the acceleration of the charge transfer rate from MIL-101(Fe) to the electron acceptors. Also, the high photocatalytic performance of composite hydrogel could be attributed to the high surface area, absorption capability, and separation efficiency of photoinduced charge carriers as the hydroxyl and carboxymethyl of β-CDP and CMC could trap the photogenerated holes resulting in the lower e^-/h^+ recombination.

3.3.5 Magnetic nano bio-composites

Iron can also be involved in magnetic nano-photocatalyst. This kind of material has been developed specially to enhance the retrievement of it after treatment by simple magnetic sorting. Nasiri et al. have developed several composites in this framework, taking advantage in addition

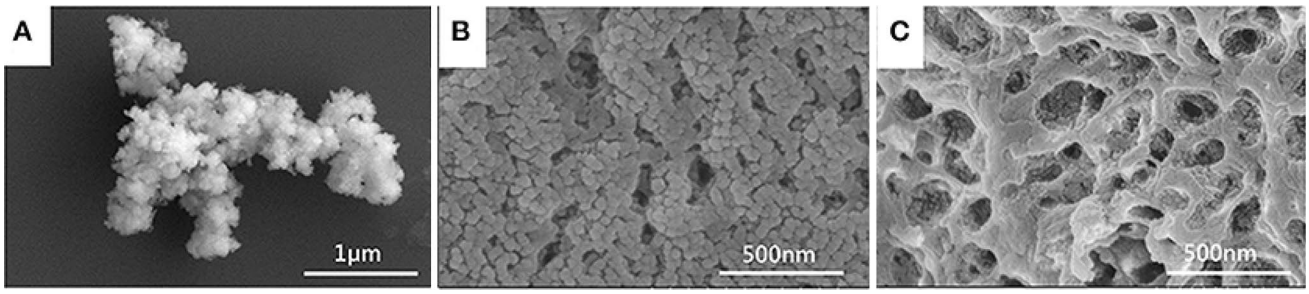

Fig. 10 SEM images of MIL-101(Fe) (**a**) and CMC/MIL-101(Fe) composite hydrogels with β-CD (**b**) and β-CDP (**c**), as prepared by Zhang and collaborators [82]. The formation of inclusions due to the presence of β-CD can be appreciated, specially at panel (**c**). Reproduced under the terms and conditions of the Creative Commons Attribution (CC BY) license

of cellulose-based matrix to support the photocatalyst (Table 10) [85–89]. Indeed, the authors underlined that both carboxymethyl or methylcellulose matrix enhanced antibiotics removal efficiency of the photocatalyst, under UV-C irradiation, by increasing the specific surface area together with the interaction with the pollutant (and thus triggering more electron–hole pairs) and a decrease in observed photocatalyst NPs aggregation.

Finally, concerning systems using a cellulose-based matrix, Fang et al. [90], investigated a more original system, without any semiconductor photocatalyst, still based on matrix extracted from plants. Indeed, they exploited the role of whewellite biomineral for binding lignin and cellulose to from film from red maple dead leaves. Owing to its intense optical absorption spanning the full solar spectrum and the heterogeneous architecture for effective charge separation, the authors has shown that this material was able to efficiently degrade tetracycline thanks to 120 min of irradiation under a simulated sunlight (97%, rate constant of 0.028 min^{-1}) or visible light (93%, rate constant of 0.021 min^{-1}).

4 Hybrid systems based on g-C_3N_4

Graphitic carbon nitride (g-C_3N_4) is a two-dimensional polymer whose structure can be seen as an association of heptazines linked to nitrogen atoms. Terminal functions are primary or secondary amines that can be functionalized to modify the polymer physicochemical properties (Fig. 11). It is generally synthesized by thermal polymerization from urea, melamine, dicyandiamide, and several other nitrogen-rich precursors by heating at around 550 °C in air or under inert atmosphere, although a large variety of methods were developed, such as microwave irradiation, ionic liquid strategy or ionothermal synthesis [91]. The resulting material has demonstrated excellent thermal and chemical stability [92], and has expressed no activity against HeLa cells after 48 h at concentrations up to 600 µg mL^{-1} [93], showing its very low toxicity for the aqueous ecosystems.

g-C_3N_4 based materials have gained a great interest the last 12 years mostly for their photocatalytic properties. Indeed, besides its easy synthesis, abundant source materials, and low toxicity, this purely organic polymer presents some significant advantages. Due to its particular band-gap structure, with a value of 2.7 eV, it both can absorb in UV/visible light, and can exhibit a strong reduction activity, making of g-C_3N_4 a powerful photocatalyst for a wide variety of applications, often better than a lot of metal oxides [94]. Its weaknesses, such as high surface inertness, small specific surface areas, or fast charge recombination can be compensated by varying the synthesis methodology, by doping with heteroatoms (B, P, metals, etc.), by varying the morphology [95], by adding electron transfer accelerators such as graphene oxide (GO) or polypyrroles (PPy), and/or by elaborating composites or nanocomposites material.

Also, biopolymers can be used as eco-compatible matrices in the conception of photocatalytic composites to enhance the g-C_3N_4 performances, notably by increasing the pollutant adsorption rate onto the catalyst. Generally, nanoparticular metallic semiconductors are used in addition to g-C_3N_4. These metal-based NPs can easily be subjected to environmental oxidation, impeding their photocatalytic performances. The use of biopolymers enables to stabilize these NPs, and thus increases the photocatalytic performances. Alhokbany et al. have associated g-C_3N_4 and Ag_3PO_4 NPs in a chitosan-based matrix and tested the resulting composite against **CIP** [96]. Under visible-light irradiation, *ca* 90% of the antibiotic was removed after 60 min, with a clear synergistic effect between g-C_3N_4 and Ag_3PO_4 NPs, but a 11% loss of activity occurred after 6 cycles in the reusability assays. Interestingly, the presence of some anions such as HCO_3^- or Cl^- seemed to impact the **CIP** photodegradation rate, with the former one probably playing the role of trapping agent of ·OH radicals. Qarajehdaghi et al. also worked on the photodegradation of **CIP** using a g-C_3N_4 nanocomposite [97]. They

Table 10 Main results obtained by Nasiri et al. with cellulose-based matrix and different photocatalyst for removing **CIP** or **MNZ** as described in [80–84]

References	Matrix	Photo catalyst (PC)	Antibiotic (AB)	pH	Irradiation duration (min)	Maximal removal efficiency	Removal mechanisms (%)		Recyclability	
							Adsorption	Photolysis	Nb of cycle	Final efficiency (%)
[85]	Carboxy methyl	$ZnFe_2O_4$ (0.3 g)	**CIP** (5 mg L^{-1})	7	100	87% (72% without matrix; 79% in waste water) $k = 0.43\ min^{-1}$ TOC: 75%	12	27	5	80
[87]	Methyl	$ZnFe_2O_4$ (0.3 g)	**MNZ** (5 mg L^{-1})	7	120	94% (80% without matrix; 71.1% in waste water) $k = 0.023\ min^{-1}$ TOC: 77.8%	0	Low	6	86
[86, 89]	Methyl	$CoFe_2O_4$ (0.2 g)	**MNZ** (5 mg L^{-1})	11	120	85% (55% without matrix) $k = 0.0087\ min^{-1}$	24	17	4	78
[88]	Methyl	$CuFe_2O_4$ (0.2 g)	**CIP** (3 mg L^{-1})	7	90	81% (51% without matrix)	18	10	4	74

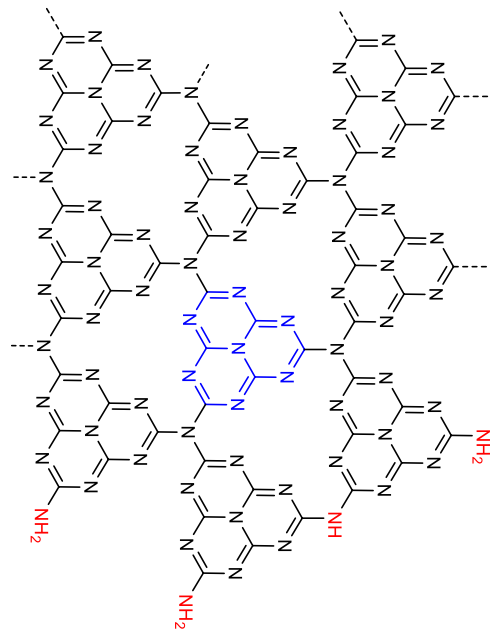

Fig. 11 Molecular structure of g-C_3N_4. In blue is shown a heptazine unit, and in red terminal amine functions

associated the photocatalyst with CdS NPs and reduced GO (rGO) and deposited this mixture on carboxymethyl cellulose to form a quaternary biocomposite. Photocatalytic performances on the **CIP** photodegradation were interesting, with 82% of degradation after only 35 min, with a significant mineralisation reaching 69% of the TOC. As previously, a 29% loss of activity was observed after only 3 cycles.

Gemifloxacin mesylate (GEM), another quinolone antibiotic, was photodegraded using a g-C_3N_4 ternary composite. Faisal et al. have enriched g-C_3N_4 with chitosan, forming a nanostructured composite in which platinum NPs (PtNPs) were incorporated. The authors explained the photodegradation increase from *ca* 70% for pure g-C_3N_4 to 93% in only 25 min by both the plasmonic effect of PtNPs and an enhanced adsorption onto the photocatalysts thanks to chitosan surface functions [98].

But metal-based NPs are not required to produce an efficient g-C_3N_4 based photocatalyst composite, although potentially hindering the performances. Wang et al. have developed an agar hydrogel with trapped g-C_3N_4 nanosheets in its 3D structure. This hydrogel showed good performances in the photodegradation of **TC**, with 85% of degradation efficiency after 120 min, and a result 1.4 times better than pure g-C_3N_4 nanosheets [99].

Main drawbacks of these strategies are the complex recyclability of the powdered composites, often showing a loss in the catalytic rate due to material loss or difficult washing of the active sites. Some studies used centrifugation to recover the photocatalyst, but in most of them the retrieval method is not described. One of the solutions is to incorporate the catalyst into macroscopic object, e.g., fabrics, films, or membranes, easily isolable from the aqueous media.

4.1 Fixation on fabrics

Biopolymers were used to fix g-C_3N_4 on fabrics to favor its use in wastewater treatment without loss of the photocatalyst nor filtration step. Zhou et al. used carboxymethylated lignocellulosic fibers of *Juncus effusus* electrostatically coated with a mix of g-C_3N_4 and GO, and woven into a flexible textile [100]. The resulting photocatalytic fabric showed promising results both under artificial and natural light irradiation, with a removal rate of **TC** reaching *ca* 87% after 180 min, and even better results on other types of contaminants (dyes, heavy metals, etc.), and a recyclability stable over time. The porous 3D structure of the *Juncus effusus* fibers played a critical role in the performances of the photocatalyst by favoring the transmittance of the light, preventing the agglomeration of on g-C_3N_4 and GO which were evenly distributed on the fibers, and allowing a better adsorption of the pollutant onto the photocatalysts.

Huo et al. applied a different strategy to build fabrics bearing g-C_3N_4 [101]. In this study, sodium alginate was meant to be used as a coating agent linked covalently to both g-C_3N_4 by dehydration between amine and carboxylate functions, and to polyester/viscose fibers. Even if evidences of covalent bonding are inconclusive, the photocatalyst still was homogeneously distributed on the surface of the fibers and grafted strongly enough to not leak between successive cycles, proving its reusability. The non-woven fabric proved to be efficient in the photodegradation of **TC**, with a removal of *ca* 98% of the antibiotic after 60 min of irradiation. Despite yielding no improvement in the photocatalytic rate compared to pure g-C_3N_4, its recyclability and its self-cleaning capacity were key successes in the development of photocatalytic fabrics.

4.2 Coupling with other water purification techniques

Photocatalysis with g-C_3N_4 was also successfully coupled with other purification techniques: filtration, electrocatalysis, and sonocatalysis. To associate photodegradation and filtration techniques, Pan et al. have developed a mixed cellulose esters (MCE) membrane supporting a first layer of GO nanosheets and a second layer of metal doped g-C_3N_4 nanosheets [102]. This MCE/GO/g-C_3N_4 membrane was tested with rhodamine B as a model compound, as well as multiple antibiotics such as **OFX**, **NOR**, **SMX**, **ERY**, and **roxithromycin (ROX)**. Compared to an MCE membrane bearing only GO or g-C_3N_4, or to an MCE/GO/g-C_3N_4 membrane without irradiation, the permeability was enhanced under light irradiation, indicating a net contribution of the photodegradation processes in the filtration system (Fig. 12). Under the right pressure, the contaminants were readily adsorbed on the membrane surface, favoring the destruction by direct contact, and preventing filter plugging. The hybrid photocatalytic membrane performances remained consistent over time, with a degradation rate always over 88% for Rhodamine B. It is important to note that the antibiotic

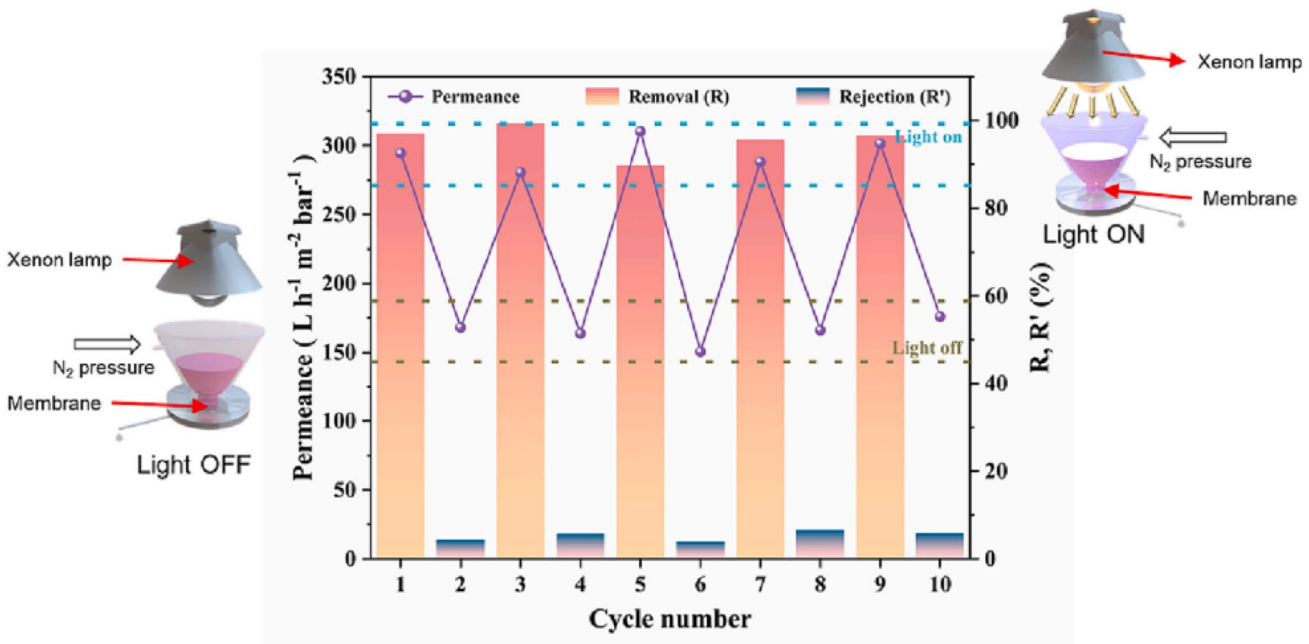

Fig. 12 System developed by Pan and collaborators [102], where coupling filtration and irradiation lead to the photodegradation of several antibiotics. Reproduced with permission from the journal

photodegradation was incomplete, leading to smaller products that more easily passed the filter mesh.

Zhou et al. have associated photocatalysis to electrocatalysis by fabricating a bacterial cellulose (BC) membrane bearing g-C_3N_4 and PPy [103]. Not only a small voltage was enough to increase antibiotic photodegradation rate, but also the electrocatalysis and the photocatalysis acted synergistically, with a degradation rate of photoelectrocatalysis 1.82 times that of the sum of photocatalysis and electrocatalysis rates. With this system, 64% of the target antibiotic, **TC**, was efficiently degraded under low irradiation and low voltage. PPy was shown to significantly improve the antibiotic photodegradation, with a rate 5.27 times higher than the same system without PPy. Moreover, the membrane showed a good recyclability, with performance still 80% of the original rate after 10 cycles. However, no evidence of mineralisation was given.

Finally, sonocatalysis was applied in combination of photocatalysis on a microfibrillated carboxymethyl cellulose film bearing metal oxides and g-C_3N_4. Sonocatalysis is an activation technique based on the property of ultrasound to form microbubbles by cavitation, which can collapse to generate supercritical conditions of high temperature and high pressure, as high as 5000 K and 1000 atm respectively. Under these conditions, H_2O can be dissociated in $^{\cdot}OH$ radicals, and the appropriate semiconductor can generate electron/hole pairs, eventually generating different ROS. Moreover, sonoluminescence can also occur during the bubble collapse, meaning a photocatalyst can as well be activated by ultrasonic irradiation [104]. Gholami et al. have used a sonophotocatalytic composite formed by Zn–Cu–Mg-mixed metal hydroxides as semiconductors and g-C_3N_4 as the photocatalyst, both included in a carboxymethyl cellulose hydrogel as a carrier to avoid their powdered form and to increase the potency of the catalysts [105]. Tested on **SUL**, the resulting film showed very promising photodegradation results with a synergetic effect between sonocatalysis, photocatalysis and the catalysts stabilization on the biopolymer, leading to up to 93% of **SUL** removal. The recyclability of the sonophotocatalyst was maintained through 10 cycles, and 83% of the antibiotic was mineralized after 200 min of irradiation.

5 Organic photocatalysts

In the previous sections we have thoroughly described the most recent contributions of hybrid materials for the photodegradation of antimicrobial drugs. In the following section we will focus on the use of organic molecules as photocatalysts, a topic which was partially recently reviewed by the authors [106].

In contrast with materials based on semiconductors catalysts, light absorption is not limited to the UV region. This is an important limitation for semiconductor materials, as sunlight, the cheapest and most abundant light source available, only comprises between 3 and 5% of UV light [107]. Then, several efforts have been made to develop new materials with a wide action spectrum in the visible light range.

Due to a recent increased interest of PhotoDynamic Therapy (PDT) and its related applications, several molecules have arisen as photosensitizers, molecules which together with light and oxygen, are capable to produce ROS [108] as consequence of an electron (Type-I) or an energy (Type-II) photoinduced transfer. These ROS have been used for several biomedical applications (i.e., antimicrobial, anti-tumor activity, and even as treatment for rheumatoid arthritis), which have been recently reviewed elsewhere [109–112]. Besides their already explored biomedical applications, their strong oxidant activity could be interesting for photocatalytical purposes. Some remarkable examples are already available in the literature, which will be further detailed (Fig. 13).

5.1 Organic photocatalysts associated to an inorganic system

Porphyrins are macrocycles containing four pyrrolic units, with elaborated π-conjugation pathways, which result in strong absorption bands, with a characteristic major band at ~ 400 nm and other absorption bands at higher wavelengths, depending on their coordination state. Their synthesis and photophysical properties (i.e., absorption coefficients, triplet state quantum yield, fluorescence quantum yield, singlet oxygen quantum yield) are well described elsewhere, as well as their potential biomedical applications [113]. Remarkably, their photophysical properties are only slightly affected when they are associated to a substrate, which has proven useful when developing heterogenous systems, and they are able to easily form metal complexes. As a remarkable example, tetrakis(4-carboxyphenyl)-porphyrin (TCPP) was used as a photocatalyst for the degradation of **TC**. TCPP was adsorbed into two different bismuth-based microspheres, based in Bi_2MoO_6 [114] or in $Bi_{12}O_{17}Cl_2$ [115], respectively. Then, the photodegradation of **TC** was explored under visible light (300 W Xenon lamp, with an UV-cut off filter at 420 nm), with formulations containing different concentrations of TCPP. In both cases, it was observed a synergistic effect, as similar concentrations of non-associated TCPP and the microspheres yielded lower degradation rates (Table 11). In both cases, they found that increasing the concentration of TCPP in the system did not lead to an improved efficiency, due to a decrease in the adsorption capacity of the systems. In both cases, the mechanism of degradation involves the production of $^{\cdot}O_2^-$ radicals, with secondary roles of $^{\cdot}OH$ and h^+, as demonstrated

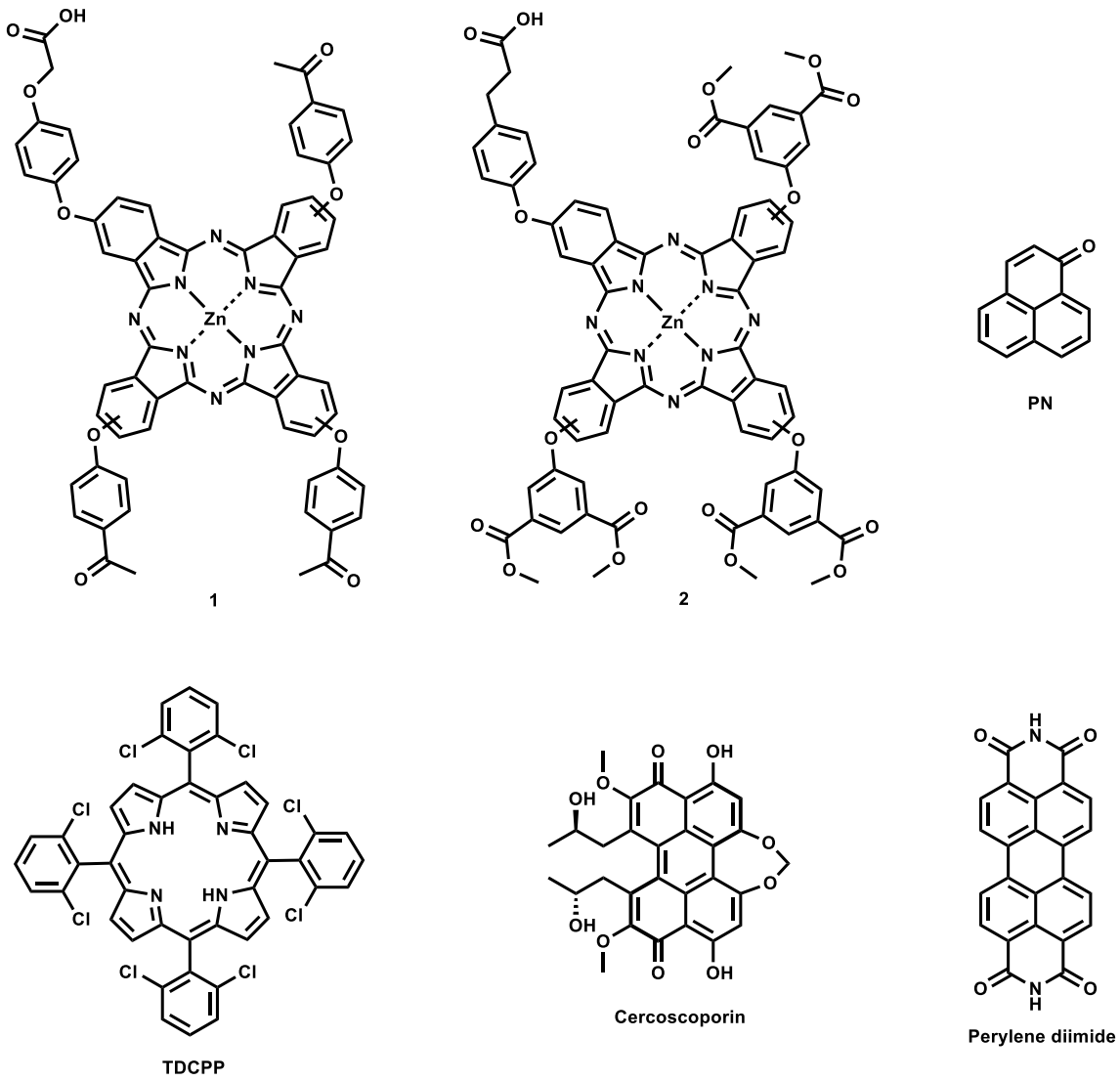

Fig. 13 Some examples of organic photosensitizers described in the literature, used for the degradation of antimicrobials

Table 11 TCPP adsorbed into bismuth-based hybrid systems

References	Hybrid system	TCPP concentration	Irradiation time (min)	% TC degradation (%)	Degradation rate (min^{-1})
[114]	Bi_2MoO_6	0%	60	~55	0.0129
		0.125%	60	~70	0.0183
		0.25%	60	~90	0.0278
		0.5%	60	~80	0.0194
		Mixture	60	~60	0.0154
[115]	$Bi_{12}O_{17}Cl_2$	0%	80	~40	0.0048
		0.25%	80	~75	0.0119
		0.5%	80	~80	0.0125
		1%	80	~65	0.0109
		Mixture	80	~50	0.0056

through scavenging tests. The explored evidence suggests that TCPP facilitates the photo-creation and dissolution of charge carriers, and it is observed that once the heteroconjunction of TCPP and their hybrid system is formed, the charge-transport resistance is significantly decreased. Interestingly, no involvement of singlet oxygen ($^1O_2$) produced by TCPP is suggested at either report.

Also, studies using phthalocyanines are reported. Phthalocyanines are compounds with an intense blue-green color, due the delocalization of their 18 π electrons. Not surprisingly, earlier applications use them as dyes and colorants, but quickly the actual potential of phthalocyanines was brought to the light [116]. Taking advantage of their well-known electrochemical, photochemical and thermal stability, Mgidlana et al. [117] used two asymmetrical phtahlocyanines (**1**, mono (3(4–oxy)phenoxy)acetic acid) tris (4-acetophenoxy) phthalocyanato zinc (II), and **2**, mono 2(-4-phenoxy)-propionic acid) tris [(dimethyl-5-phenoxy)isophthalate] phthalocyaninato zinc) to decorate different materials, namely $NiWO_4$, Ag_2Wo_4, Ag-Fe_3O_4 and $CoWO_4$. The characterization of the conjugates focused on the photophysical and physical properties of the phthalocyanines, thus their fluorescent, triplet state and singlet oxygen quantum yields are reported. Notably, the association between **2** and $CoWO_4$ has a positive effect on the triplet state quantum yield (from 0.46 to 0.72, once conjugated) and consequently in their singlet oxygen quantum yield (0.31 to 0.61, once conjugated). These conjugates were used to degrade **TC** at different concentrations (14.5–66.2 μM), obtaining k_{obs} values of around 0.00031 and 0.00353 min^{-1}, with 2-$CoWo_4$ and **TC** at 14.5 μM having the best rate observed (0.00353 min^{-1}). Remarkably, the conjugates were able to be reused at least once, without observing affectation of the photophysical properties of 2. Further work is needed before obtaining the degradation rates of inorganic materials, nevertheless, these results are encouraging for the use of a hybrid material in association with a photosensitizer.

Evidently, the association of a photosensitizer and a hybrid material will be influenced by the quantum efficiency of the envisioned photosensitizer. In this sense, phenalenone is a well-known photosensitizer with a singlet oxygen quantum yield of 1, with strong light absorption around 390 nm [118]. Taking advantage of their remarkable photophysical characteristics, together with its stability and easiness of synthesis, Godard and collaborators recently grafted phenalenone to sand (PN-Sand) and used this organic/inorganic material as a photocatalyst for the degradation of **tebuconazole** (**TBZ**), a recalcitrant antifungal, assessing its efficiency at laboratory scale [119] and at a fluidized bed pilot unit [120]. Researchers focused on the effect of the rate photocatalyst/antibiotics to test the efficiency of their system, and they found that at a rate of 76% the system achieves their maximum efficiency (78% of **TBZ** degradation), and higher rates produce a shield effect that decreases the degradation efficiency. This is relevant, as the sorption process contributes up to 49% to the total degradation process, clearly identified in the first 100 min. When evaluating the efficiency of different light sources, UV light appeared to be the most efficient, with a degradation rate of 0.0023 min^{-1}, compared with a degradation rate of 0.0012 min^{-1} when using visible light. This was taken in account for further experiments, as the scaled-up fluidized bed reactor only uses violet (380–440 nm) and blue (435–465 nm) LED light strips as light source. Furthermore, the radicals involved in the process were identified, with singlet oxygen being the lead radical involved, suggesting a Type-II photodynamic process.

5.2 Organic photocatalysts associated to an organic matrix

In some cases, researchers have looked for antibiotics degradation without using a hybrid material. As an example, Piccirillo and collaborators [2] loaded acetylated lignin NPs with 5,10,15,20-tetrakis(2,6-dichlorophenyl)porphyrin (TDCPP), yielding a nanoscale formulation (TDCPP@AcL) that was used for the degradation of **trimetroprim (TMP)** and **SMX**, individually and as a drug cocktail, under a mercury lamp light source irradiation. Researchers found remarkable degradation results, obtaining 99% of **TMP** degradation after 4 h of irradiation, 98% of **SMX** degradation after 0.3 h of irradiation and 99% of the cocktail degradation after 2 h of irradiation. Furthermore, their system was found to be extremely efficient obtaining mineralisation rates above 75% after 24 h of irradiation at all conditions. In addition, authors were able to reuse the system for up to 10 times, without any loss of efficiency, demonstrating outstanding performance of an organic photocatalyst, without the need of a hybrid system or an additional oxidative agent.

In another example, Amaly and collaborators [121] developed a microcrystalline cellulose aerogel, doped with both montomorillonite and methylene blue as a photocatalysts. In an interesting setup, **TC** spiked water was filtered through the aerogel, being adsorbed into the material and enabling its photodegradation, under UV-A (365 nm) or red (660 nm) light. The results found showed that the aerogel was able to degrade up to 95% of **TC**, when the aerogel was loaded with up to 500 mgL^{-1} of methylene blue. Interestingly, their results show that increasing the concentration of methylene blue indeed increased the photodegradation efficiency, a remarkable difference with some of the previous studies discussed along this review.

Finally, in a last example, Wu and collaborators [122] chose cercoscoporin, a photosensitizer produced by the fungi *Cercospora sp.*, as the photocatalyst for several macroporous resins. These commercially available resins are well-studied and have been previously characterized for different

applications. Researchers found that the combination cercosporin and polymethacrylate (CP/MMA) yielded the best results for the photodegradation of **CIP** under artificial light and sunlight. At best, **CIP** was found to be degraded down to 99.8%, after 3 h of irradiation (0.035 min^{-1}), mainly through the participation of singlet oxygen, $^{\cdot}O_2^-$ and h^+ oxidative agents. Similar results were found for different fluoroquinolones, and with demonstrated stability and reusability potential.

5.3 Porous organic polymer and other organic polymers

Perylene diimide is a well-known class of organic dyes with interesting chemical, thermal and photochemical stability, properties that have attracted attention in the last few years for them to be used as biosensors, components in organic light emitting diodes and photosensitizers [123]. In a recent example, Zhang and collaborators [124] developed a system using perylene diimide and imidazole, yielding a three-dimensional structure (3D-PDI) that was used to degrade several antibiotics (**TC**, **chlortetracycline** (**CTC**), **OTC** and **CIP**). Remarkably, when comparing the efficiency of 3D-PDI, it was more performant that some hybrid materials (i.e., Bi_2WO_6 and g-C_3N_4), under visible-light irradiation. Although **TC** was used as the main model along the whole work, the degradation rates for **TC**, **CTC**, **OTC** and **CIP** were measured (0.443, 0.403, 0.419 and ~ 0.05 h^{-1}), obtaining deficient results for **CIP** degradation and considered negligible. Furthermore, the authors achieved a TOC removal of 80% after five h of irradiation, with important contributions from the porosity of the material to adsorb the antibiotics, and with a principal contribution from $^{\cdot}OH$ and h^+ species.

6 Conclusion

The present review attempted to present the photocatalytic efforts to degrade antimicrobials reported in some of the most recent publications. The lack of representativity of non-antibacterial antimicrobials in this review, reflects the lack of examples found in the literature, representing an area of opportunity for further research approaches. However, from the analysis of the literature herein reviewed, it is obviously that the scientific community has been committed in finding more sustainable and alternative catalytic processes for the degradation of antibiotics in the environment, attempting to diminish the increase of multi resistant bacteria. In addition, by the use of bio-based materials, new systems have been developed, evidencing very often a synergetic effect with the semiconductors. Also, smart strategies have been investigated to improve the photocatalytic system, relying on its optical properties as well as its recyclability and its recovery. In this framework, all organic systems are very promising. Indeed, they are polyvalent and able to both degrade antibiotic and eradicate bacteria thanks to photodynamic process, that is a great asset in the necessary upstream approach, where antibiotic misuse ought to end, as well as in a downstream strategy, by developing alternative degradation processes.

Declarations

Conflict of interest On behalf of all authors, the corresponding author states that there is no conflict of interest.

References

1. Calvete, M. J. F., Piccirillo, G., Vinagreiro, C. S., & Pereira, M. M. (2019). Hybrid materials for heterogeneous photocatalytic degradation of antibiotics. *Coordination Chemistry Reviews, 395*, 63–85. https://doi.org/10.1016/j.ccr.2019.05.004
2. Piccirillo, G., Maldonado-Carmona, N., Marques, D. L., Villandier, N., Calliste, C. A., Leroy-Lhez, S., Eusébio, M. E. S., Calvete, M. J. F., & Pereira, M. M. (2022). Porphyrin@Lignin nanoparticles: Reusable photocatalysts for effective aqueous degradation of antibiotics. *Catalysis Today*. https://doi.org/10.1016/j.cattod.2022.09.009
3. Aarestrup, F. M., Kruse, H., Tast, E., Hammerum, A. M., & Jensen, L. B. (2000). Associations between the use of antimicrobial agents for growth promotion and the occurrence of resistance among Enterococcus faecium from broilers and pigs in Denmark, Finland, and Norway. *Microbial Drug Resistance, 6*, 63–70. https://doi.org/10.1089/mdr.2000.6.63
4. Ventola, C. L. (2015). The antibiotic resistance crisis: Part 1: Causes and threats. *Pharmacy & Therapeutics., 40*(4), 277–283.
5. Blaser, M. J. (2016). Antibiotic use and its consequences for the normal microbiome. *Science, 352*, 544–545. https://doi.org/10.1126/science.aad9358
6. Aydin, S., Ince, B., & Ince, O. (2016). Assessment of anaerobic bacterial diversity and its effects on anaerobic system stability and the occurrence of antibiotic resistance genes. *Bioresource Technology, 207*, 332–338. https://doi.org/10.1016/j.biortech.2016.01.080
7. Brown, E. D., & Wright, G. D. (2016). Antibacterial drug discovery in the resistance era. *Nature, 529*, 336–343. https://doi.org/10.1038/nature17042
8. Bérdy, J. (2012). Thoughts and facts about antibiotics: Where we are now and where we are heading. *Journal of Antibiotics, 65*, 385–395. https://doi.org/10.1038/ja.2012.27
9. Van Boeckel, T. P., Brower, C., Gilbert, M., Grenfell, B. T., Levin, S. A., Robinson, T. P., Teillant, A., & Laxminarayan, R. (2015). Global trends in antimicrobial use in food animals. *Proceedings of the National academy of Sciences of the United States of America, 112*, 5649–5654. https://doi.org/10.1073/pnas.1503141112
10. Review on Antimicrobial Resistance. (2014). *Antimicrobial resistance: Tackling a crisis for the health and wealth of nations*. https://amr-review.org/Publications.html
11. Bastard, J., Nhung, N. T., Hien, V. B., Kiet, B. T., Temime, L., Opatowski, L., Carrique-Mas, J., & Choisy, M. (2022). Modelling the impact of antimicrobial use and external introductions on commensal *E. coli* colistin resistance in small-scale chicken farms of the Mekong delta of Vietnam. *Transboundary and*

Emerging Diseases, 69, e2185–e2194. https://doi.org/10.1111/tbed.14558
12. Kumar, R., Ansari, M. O., Taleb, M. A., Oves, M., Barakat, M. A., Alghamdi, M. A., & Al Makishah, N. H. (2022). Integrated adsorption-photocatalytic decontamination of oxytetracycline from wastewater using S-doped TiO_2/WS2/calcium alginate beads. *Catalysts, 12*, 1676. https://doi.org/10.3390/catal12121676
13. Nawaz, M., Khan, A. A., Hussain, A., Jang, J., Jung, H.-Y., & Lee, D. S. (2020). Reduced graphene oxide−TiO_2/sodium alginate 3-dimensional structure aerogel for enhanced photocatalytic degradation of ibuprofen and sulfamethoxazole. *Chemosphere, 261*, 127702. https://doi.org/10.1016/j.chemosphere.2020.127702
14. Ikhlef-Taguelmimt, T., Hamiche, A., Yahiaoui, I., Bendellali, T., Lebik-Elhadi, H., Ait-Amar, H., & Aissani-Benissad, F. (2020). Tetracycline hydrochloride degradation by heterogeneous photocatalysis using TiO_2(P25) immobilized in biopolymer (chitosan) under UV irradiation. *Water Science and Technology, 82*, 1570–1578. https://doi.org/10.2166/wst.2020.432
15. Yue, Y., Shen, S., Cheng, W., Han, G., Wu, Q., & Jiang, J. (2022). Construction of mechanically robust and recyclable photocatalytic hydrogel based on nanocellulose-supported CdS/MoS2/Montmorillonite hybrid for antibiotic degradation. *Colloids and Surfaces A: Physicochemical and Engineering Aspects, 636*, 128035. https://doi.org/10.1016/j.colsurfa.2021.128035
16. Zekri, M. E. M., & Colbeau-Justin, C. (2013). A mathematical model to describe the photocatalytic reality: What is the probability that a photon does its job? *Chemical Engineering Journal, 225*, 547–557. https://doi.org/10.1016/j.cej.2013.03.129
17. Lee, J., & Lee, M. (2017). Improved light harvest in diffraction grating-embedded TiO_2 nanoparticle film. *Applied Physics A, 123*, 737. https://doi.org/10.1007/s00339-017-1368-5
18. Homem, V., & Santos, L. (2011). Degradation and removal methods of antibiotics from aqueous matrices—A review. *Journal of Environmental Management, 92*, 2304–2347. https://doi.org/10.1016/j.jenvman.2011.05.023
19. Andreozzi, R. (1999). Advanced oxidation processes (AOP) for water purification and recovery. *Catalysis Today, 53*, 51–59. https://doi.org/10.1016/S0920-5861(99)00102-9
20. Bartolomeu, M., Neves, M. G. P. M. S., Faustino, M. A. F., & Almeida, A. (2018). Wastewater chemical contaminants: Remediation by advanced oxidation processes. *Photochemical & Photobiological Sciences, 17*, 1573–1598. https://doi.org/10.1039/C8PP00249E
21. Norvill, Z. N., Shilton, A., & Guieysse, B. (2016). Emerging contaminant degradation and removal in algal wastewater treatment ponds: Identifying the research gaps. *Journal of Hazardous Materials, 313*, 291–309. https://doi.org/10.1016/j.jhazmat.2016.03.085
22. Crombie, K., Mašek, O., Sohi, S. P., Brownsort, P., & Cross, A. (2013). The effect of pyrolysis conditions on biochar stability as determined by three methods. *GCB Bioenergy, 5*, 122–131. https://doi.org/10.1111/gcbb.12030
23. Ambaye, T. G., Vaccari, M., Van Hullebusch, E. D., Amrane, A., & Rtimi, S. (2021). Mechanisms and adsorption capacities of biochar for the removal of organic and inorganic pollutants from industrial wastewater. *International Journal of Environmental Science and Technology, 18*, 3273–3294. https://doi.org/10.1007/s13762-020-03060-w
24. Kim, J. R., & Kan, E. (2016). Heterogeneous photocatalytic degradation of sulfamethoxazole in water using a biochar-supported TiO_2 photocatalyst. *Journal of Environmental Management, 180*, 94–101. https://doi.org/10.1016/j.jenvman.2016.05.016
25. Zhang, H., Wang, Z., Li, R., Guo, J., Li, Y., Zhu, J., & Xie, X. (2017). TiO_2 supported on reed straw biochar as an adsorptive and photocatalytic composite for the efficient degradation of sulfamethoxazole in aqueous matrices. *Chemosphere, 185*, 351–360. https://doi.org/10.1016/j.chemosphere.2017.07.025
26. Xie, X., Li, S., Zhang, H., Wang, Z., & Huang, H. (2019). Promoting charge separation of biochar-based Zn-TiO_2/pBC in the presence of ZnO for efficient sulfamethoxazole photodegradation under visible light irradiation. *Science of The Total Environment, 659*, 529–539. https://doi.org/10.1016/j.scitotenv.2018.12.401
27. Jin, Y., Tang, W., Wang, J., Chen, Z., Ren, F., Sun, Z., Wang, F., & Ren, P. (2022). High photocatalytic activity of spent coffee grounds derived activated carbon-supported Ag/TiO_2 catalyst for degradation of organic dyes and antibiotics. *Colloids and Surfaces A: Physicochemical and Engineering Aspects, 655*, 130316. https://doi.org/10.1016/j.colsurfa.2022.130316
28. Wang, W., Zhang, J., Chen, T., Sun, J., Ma, X., Wang, Y., Wang, J., & Xie, Z. (2020). Preparation of TiO_2-modified biochar and its characteristics of photo-catalysis degradation for enrofloxacin. *Science and Reports, 10*, 6588. https://doi.org/10.1038/s41598-020-62791-5
29. Asgharzadeh, F., Kalantary, R. R., Gholami, M., Jafari, A. J., Kermani, M., & Asgharnia, H. (2023). TiO_2-decorated magnetic biochar mediated heterogeneous photocatalytic degradation of tetracycline and evaluation of antibacterial activity. *Biomass Conversion and Biorefinery, 13*, 8949–8959. https://doi.org/10.1007/s13399-021-01685-6
30. Asgharzadeh, F., Gholami, M., Jonidi Jafari, A., Kermani, M., Asgharnia, H., & Kalantary, R. R. (2020). Heterogeneous photocatalytic degradation of metronidazole from aqueous solutions using Fe_3O_4/TiO_2 supported on biochar. *DWT, 175*, 304–315. https://doi.org/10.5004/dwt.2020.24789
31. Zhang, Z., Liang, J., Zhang, W., Zhou, M., Zhu, X., Liu, Z., Li, Y., Guan, Z., Lee, C.-S., Wong, P. K., Li, H., & Jiang, Z. (2023). Modified-pollen confined hybrid system: A promising union for visible-light-driven photocatalytic antibiotic degradation. *Applied Catalysis B: Environmental, 330*, 122621. https://doi.org/10.1016/j.apcatb.2023.122621
32. Gholami, P., Khataee, A., Soltani, R. D. C., Dinpazhoh, L., & Bhatnagar, A. (2020). Photocatalytic degradation of gemifloxacin antibiotic using Zn-Co-LDH@biochar nanocomposite. *Journal of Hazardous Materials, 382*, 121070. https://doi.org/10.1016/j.jhazmat.2019.121070
33. Mohd Azan, N. A. A., Sagadevan, S., Mohamed, A. R., Nor Azazi, A. H., Suah, F. B. M., Kobayashi, T., Adnan, R., & Mohd Kaus, N. H. (2022). Solar light-induced photocatalytic degradation of ciprofloxacin antibiotic using biochar supported nano bismuth ferrite composite. *Catalysts, 12*, 1269. https://doi.org/10.3390/catal12101269
34. Wang, T., Dissanayake, P. D., Sun, M., Tao, Z., Han, W., An, N., Gu, Q., Xia, D., Tian, B., Ok, Y. S., & Shang, J. (2021). Adsorption and visible-light photocatalytic degradation of organic pollutants by functionalized biochar: Role of iodine doping and reactive species. *Environmental Research, 197*, 111026. https://doi.org/10.1016/j.envres.2021.111026
35. Li, Q., Liu, S., Zhang, X., Hu, G., & Xia, H. (2022). High-efficiency sulfur-doped carbon photocatalysts synthesized by carbonization of lignosulfonate at low temperature. *Materials Today Communications, 33*, 104448. https://doi.org/10.1016/j.mtcomm.2022.104448
36. Nguyen, L. T., Nguyen, H. T., Nguyen, K. M., Pham, T. T., & Bruggen, B. V. D. (2021). Combined adsorption and photocatalytic degradation for ciprofloxacin removal using sugarcane bagasse/N, S-TiO_2 powder composite. *Water, 13*, 2300. https://doi.org/10.3390/w13162300
37. Alghamdi, Y. G., Krishnakumar, B., Malik, M. A., & Alhayyani, S. (2022). Design and preparation of biomass-derived activated carbon loaded TiO_2 photocatalyst for photocatalytic degradation

of reactive red 120 and ofloxacin. *Polymers, 14*, 880. https://doi.org/10.3390/polym14050880
38. Zhang, G., Zhang, T., Li, B., Jiang, S., Zhang, X., Hai, L., Wu, W., & Chen, X. (2018). Tubular structure TiO_2/C/TiO_2 hybrid derived from the waste of the fluff of chinar tree. *Journal of Alloys and Compounds, 737*, 774–789. https://doi.org/10.1016/j.jallcom.2017.12.182
39. Li, H., Hu, J., Wang, X., & An, L. (2019). Development of a bio-inspired photo-recyclable feather carbon adsorbent towards removal of amoxicillin residue in aqueous solutions. *Chemical Engineering Journal, 373*, 1380–1388. https://doi.org/10.1016/j.cej.2019.03.160
40. Alfred, M. O., Omorogie, M. O., Bodede, O., Moodley, R., Ogunlaja, A., Adeyemi, O. G., Günter, C., Taubert, A., Iermak, I., Eckert, H., Silva, I. D. A., De Camargo, A. S. S., De Jesus, M. A., Clarke, S. M., & Unuabonah, E. I. (2020). Solar-active clay-TiO_2 nanocomposites prepared via biomass assisted synthesis: Efficient removal of ampicillin, sulfamethoxazole and artemether from water. *Chemical Engineering Journal, 398*, 125544. https://doi.org/10.1016/j.cej.2020.125544
41. Isa, E. D. M., Shameli, K., Ch'ng, H. J., Che Jusoh, N. W., & Hazan, R. (2021). Photocatalytic degradation of selected pharmaceuticals using green fabricated zinc oxide nanoparticles. *Advanced Powder Technology, 32*, 2398–2409. https://doi.org/10.1016/j.apt.2021.05.021
42. Yahia, B., Faouzi, S., Ahmed, C., Lounis, S., & Mohamed, T. (2022). A new hybrid process for Amoxicillin elimination by combination of adsorption and photocatalysis on (CuO/AC) under solar irradiation. *Journal of Molecular Structure, 1261*, 132769. https://doi.org/10.1016/j.molstruc.2022.132769
43. Singh, P., Priya, B., Shandilya, P., Raizada, P., Singh, N., Pare, B., & Jonnalagadda, S. B. (2019). Photocatalytic mineralization of antibiotics using 60%WO3/BiOCl stacked to graphene sand composite and chitosan. *Arabian Journal of Chemistry, 12*, 4627–4645. https://doi.org/10.1016/j.arabjc.2016.08.005
44. Li, Y., Fu, Y., & Zhu, M. (2020). Green synthesis of 3D tripyramid TiO_2 architectures with assistance of aloe extracts for highly efficient photocatalytic degradation of antibiotic ciprofloxacin. *Applied Catalysis B: Environmental, 260*, 118149. https://doi.org/10.1016/j.apcatb.2019.118149
45. Wang, T., Liu, X., Xu, T., Wei, M., Ma, C., Huo, P., & Yan, Y. (2020). Lignin-controlled photocatalyst of porous BiVO4-C nanocomposite for enhancing photocatalytic activity toward pollutant under visible-light. *Applied Surface Science, 523*, 146401. https://doi.org/10.1016/j.apsusc.2020.146401
46. Shi, L., Zou, X., Wang, T., Wang, D., Fan, M., & Gong, Z. (2022). Sunlight photocatalytic degradation of ofloxacin using UiO-66/wood composite photocatalysts. *Chinese Chemical Letters, 33*, 442–446. https://doi.org/10.1016/j.cclet.2021.06.048
47. Gonçalves, M. G., Da Silva Veiga, P. A., Fornari, M. R., Peralta-Zamora, P., Mangrich, A. S., & Silvestri, S. (2020). Relationship of the physicochemical properties of novel ZnO/biochar composites to their efficiencies in the degradation of sulfamethoxazole and methyl orange. *Science of The Total Environment, 748*, 141381. https://doi.org/10.1016/j.scitotenv.2020.141381
48. Vaya, D., & Surolia, P. K. (2020). Semiconductor based photocatalytic degradation of pesticides: An overview. *Environmental Technology & Innovation, 20*, 101128. https://doi.org/10.1016/j.eti.2020.101128
49. Anto, S., Sudhakar, M. P., Shan Ahamed, T., Samuel, M. S., Mathimani, T., Brindhadevi, K., & Pugazhendhi, A. (2021). Activation strategies for biochar to use as an efficient catalyst in various applications. *Fuel, 285*, 119205. https://doi.org/10.1016/j.fuel.2020.119205
50. Gusain, R., Gupta, K., Joshi, P., & Khatri, O. P. (2019). Adsorptive removal and photocatalytic degradation of organic pollutants using metal oxides and their composites: A comprehensive review. *Advances in Colloid and Interface Science, 272*, 102009. https://doi.org/10.1016/j.cis.2019.102009
51. Bruckmann, F. S., Schnorr, C., Oviedo, L. R., Knani, S., Silva, L. F. O., Silva, W. L., Dotto, G. L., & Bohn Rhoden, C. R. (2022). Adsorption and photocatalytic degradation of pesticides into nanocomposites: A review. *Molecules, 27*, 6261. https://doi.org/10.3390/molecules27196261
52. Pastre, M. M. G., Cunha, D. L., & Marques, M. (2022). Design of biomass-based composite photocatalysts for wastewater treatment: A review over the past decade and future prospects. *Environmental Science and Pollution Research, 30*, 9103–9126. https://doi.org/10.1007/s11356-022-24089-z
53. Dahlan, R., Mcdonald, C., & Sunderland, V. B. (2011). Solubilities and intrinsic dissolution rates of sulphamethoxazole and trimethoprim. *Journal of Pharmacy and Pharmacology, 39*, 246–251. https://doi.org/10.1111/j.2042-7158.1987.tb06261.x
54. Unutkan, T., Bakırdere, S., & Keyf, S. (2018). Development of an analytical method for the determination of amoxicillin in commercial drugs and wastewater samples, and assessing its stability in simulated gastric digestion. *Journal of Chromatographic Science, 56*, 36–40. https://doi.org/10.1093/chromsci/bmx078
55. Mehmood, Ch. T., Zhong, Z., Zhou, H., & Xiao, Y. (2020). Constructing porous beads with modified polysulfone-alginate and TiO_2 as a robust and recyclable photocatalyst for wastewater treatment. *Journal of Water Process Engineering, 38*, 101601. https://doi.org/10.1016/j.jwpe.2020.101601
56. Mehmood, Ch. T., Zhong, Z., Zhou, H., Zhang, C., & Xiao, Y. (2020). Immobilizing a visible light-responsive photocatalyst on a recyclable polymeric composite for floating and suspended applications in water treatment. *RSC Advances, 10*, 36349–36362. https://doi.org/10.1039/D0RA06864K
57. Kumar, A., Rana, A., Guo, C., Sharma, G., Katubi, K. M., Alzahrani, F. M., Naushad, M., Sillanpää, M., Dhiman, P., & Stadler, F. J. (2021). Acceleration of photo-reduction and oxidation capabilities of Bi_4O5I2/SPION@calcium alginate by metallic Ag: Wide spectral removal of nitrate and azithromycin. *Chemical Engineering Journal, 423*, 130173. https://doi.org/10.1016/j.cej.2021.130173
58. Du, Z., Liu, F., Xiao, C., Dan, Y., & Jiang, L. (2021). Fabrication of poly(vinyl alcohol)/sodium alginate hydrogel beads and its application in photo-Fenton degradation of tetracycline. *Journal of Materials Science, 56*, 913–926. https://doi.org/10.1007/s10853-020-05299-7
59. Roy, N., Kannabiran, K., & Mukherjee, A. (2022). Studies on photocatalytic removal of antibiotics, ciprofloxacin and sulfamethoxazole, by Fe_3O_4–ZnO-Chitosan/Alginate nanocomposite in aqueous systems. *Advanced Powder Technology, 33*, 103691. https://doi.org/10.1016/j.apt.2022.103691
60. Kumar, M. (2022). Photocatalytic and adsorptive performance of polyvinyl alcohol/chitosan/TiO_2 composite for antibiotics removal: single- and multi-pollutant conditions. *Water Science and Technology, 86*, 800–813. https://doi.org/10.2166/wst.2022.243
61. Bergamonti, L., Graiff, C., Bergonzi, C., Potenza, M., Reverberi, C., Ossiprandi, M. C., Lottici, P. P., Bettini, R., & Elviri, L. (2022). Photodegradation of pharmaceutical pollutants: New photocatalytic systems based on 3D printed scaffold-supported Ag/TiO_2 nanocomposite. *Catalysts, 12*, 580. https://doi.org/10.3390/catal12060580
62. Erim, B., Ciğeroğlu, Z., & Bayramoğlu, M. (2021). Green synthesis of TiO_2/GO/chitosan by using leaf extract of Olea europaea as a highly efficient photocatalyst for the degradation of cefixime trihydrate under UV-A radiation exposure: An optimization study with d-optimal design. *Journal of Molecular Structure, 1234*, 130194. https://doi.org/10.1016/j.molstruc.2021.130194

63. Asadzadeh Patehkhor, H., Fattahi, M., & Khosravi-Nikou, M. (2021). Synthesis and characterization of ternary chitosan–TiO_2–ZnO over graphene for photocatalytic degradation of tetracycline from pharmaceutical wastewater. *Science and Reports, 11*, 24177. https://doi.org/10.1038/s41598-021-03492-5
64. Arghavan, F. S., Al-Musawi, T. J., Rumman, G. A., Pelalak, R., Khataee, A., & Nasseh, N. (2021). Photocatalytic performance of a nickel ferrite/chitosan/bismuth(III) oxyiodide nanocomposite for metronidazole degradation under simulated sunlight illumination. *Journal of Environmental Chemical Engineering, 9*, 105619. https://doi.org/10.1016/j.jece.2021.105619
65. Ashraf, M. A., Li, C., Zhang, D., Zhao, L., & Fakhri, A. (2021). Fabrication of silver phosphate-ilmenite nanocomposites supported on glycol chitosan for visible light-driven degradation, and antimicrobial activities. *International Journal of Biological Macromolecules, 169*, 436–442. https://doi.org/10.1016/j.ijbiomac.2020.12.049
66. Bhatia, N., Kumari, A., Thakur, N., Sharma, G., Singh, R. R., & Sharma, R. (2022). Phytochemically stabilized chitosan encapsulated Cu and Ag nanocomposites to remove cefuroxime axetil and pathogens from the environment. *International Journal of Biological Macromolecules, 212*, 451–464. https://doi.org/10.1016/j.ijbiomac.2022.05.143
67. Hassan Mohamed, N. A., Shamma, R. N., Elagroudy, S., & Adewuyi, A. (2022). Visible light-driven photocatalytic degradation of ciprofloxacin, ampicillin and erythromycin by zinc ferrite immobilized on chitosan. *Resources, 11*, 81. https://doi.org/10.3390/resources11100081
68. Honarmand, M., Naeimi, A., Rezakhani, M. S., & Chaji, M. A. (2022). Ni/NiO doped chitosan-cellulose based on the wastes of barley and shrimp for degradation of ciprofloxacin antibiotic. *Journal of Materials Research and Technology, 18*, 4060–4074. https://doi.org/10.1016/j.jmrt.2022.04.046
69. Huang, X., Wu, S., Tang, S., Huang, L., Zhu, D., & Hu, Q. (2020). Photocatalytic hydrogel layer supported on alkali modified straw fibers for ciprofloxacin removal from water. *Journal of Molecular Liquids, 317*, 113961. https://doi.org/10.1016/j.molliq.2020.113961
70. Zeghioud, H., Kamagate, M., Coulibaly, L. S., Rtimi, S., & Assadi, A. A. (2019). Photocatalytic degradation of binary and ternary mixtures of antibiotics: Reactive species investigation in pilot scale. *Chemical Engineering Research and Design, 144*, 300–309. https://doi.org/10.1016/j.cherd.2019.02.015
71. Wang, D., Yang, J., Yang, H., Zhao, P., & Shi, Z. (2022). Fe-complex modified cellulose acetate composite membrane with excellent photo-Fenton catalytic activity. *Carbohydrate Polymers, 296*, 119960. https://doi.org/10.1016/j.carbpol.2022.119960
72. Imam, S. S., Adnan, R., & Mohd Kaus, N. H. (2020). Immobilization of BiOBr into cellulose acetate matrix as hybrid film photocatalyst for facile and multicycle degradation of ciprofloxacin. *Journal of Alloys and Compounds, 843*, 155990. https://doi.org/10.1016/j.jallcom.2020.155990
73. Gao, B., Tao, K., Xi, Z., El-Sayed, M. M. H., Shoeib, T., & Yang, H. (2022). Fabrication of 3D lignosulfonate composited sponges impregnated by $BiVO_4$/polyaniline/Ag ternary photocatalyst for synergistic adsorption-photodegradation of fluoroquinolones in water. *Chemical Engineering Journal, 446*, 137282. https://doi.org/10.1016/j.cej.2022.137282
74. Wang, T., Liu, X., Han, D., Sun, Y., Ma, C., Liu, Y., Huo, P., & Yan, Y. (2019). In-situ synthesis of $BiVO_4$ QDs/cellulose fibers composite for photocatalytic application. *International Journal of Hydrogen Energy, 44*, 31969–31978. https://doi.org/10.1016/j.ijhydene.2019.10.096
75. Nahi, J., Radhakrishnan, A., & Beena, B. (2021). Green synthesis of zinc oxide incorporated nanocellulose with visible light photocatalytic activity and application for the removal of antibiotic enrofloxacin from aqueousmedia. *Materials Today: Proceedings, 41*, 583–589. https://doi.org/10.1016/j.matpr.2020.05.253
76. Thi Thanh Nhi, L., Van Thuan, L., My Uyen, D., Nguyen, M. H., Thu, V. T., Khieu, D. Q., & Sinh, L. H. (2020). Facile fabrication of highly flexible and floatable Cu_2O/rGO on Vietnamese traditional paper toward high-performance solar-light-driven photocatalytic degradation of ciprofloxacin antibiotic. *RSC Advances, 10*, 16330–16338. https://doi.org/10.1039/D0RA01854F
77. Li, W., Li, B., Meng, M., Cui, Y., Wu, Y., Zhang, Y., Dong, H., & Feng, Y. (2019). Bimetallic Au/Ag decorated TiO_2 nanocomposite membrane for enhanced photocatalytic degradation of tetracycline and bactericidal efficiency. *Applied Surface Science, 487*, 1008–1017. https://doi.org/10.1016/j.apsusc.2019.05.162
78. Wang, G., Wang, X., Liu, J., & Sun, X. (2012). Mesoporous Au/TiO_2 nanocomposite microspheres for visible-light photocatalysis. *Chemistry—A European Journal, 18*, 5361–5366. https://doi.org/10.1002/chem.201101410
79. Zhao, P., Yang, Y., Pei, Y., & Luo, X. (2023). TEMPO-oxidized cellulose beads embedded with Au-doped TiO_2 nanoparticles for photocatalytic degradation of Tylosin. *Cellulose, 30*, 1133–1147. https://doi.org/10.1007/s10570-022-04935-6
80. Du, M., Du, Y., Feng, Y., Li, Z., Wang, J., Jiang, N., & Liu, Y. (2019). Advanced photocatalytic performance of novel BiOBr/BiOI/cellulose composites for the removal of organic pollutant. *Cellulose, 26*, 5543–5557. https://doi.org/10.1007/s10570-019-02474-1
81. Naeimi, A., Honarmand, M., Ali Chaji, M., & Khosravi, S. (2022). Green synthesis of bentonite/cellulose@lead oxide bionanocomposite with assistance of Pistacia Atlantica extract for efficient photocatalytic degradation of ciprofloxacin. *Advanced Powder Technology, 33*, 103441. https://doi.org/10.1016/j.apt.2022.103441
82. Zhang, H., Zhou, L., Li, J., Rong, S., Jiang, J., & Liu, S. (2021). Photocatalytic degradation of tetracycline by a novel (CMC)/MIL-101(Fe)/β-CDP composite hydrogel. *Frontiers in Chemistry, 8*, 593730. https://doi.org/10.3389/fchem.2020.593730
83. Xu, M., Deng, Y., Li, S., Zheng, J., Liu, J., Tremblay, P.-L., & Zhang, T. (2023). Bacterial cellulose flakes loaded with Bi_2MoO6 nanoparticles and quantum dots for the photodegradation of antibiotic and dye pollutants. *Chemosphere, 312*, 137249. https://doi.org/10.1016/j.chemosphere.2022.137249
84. Wu, Y., Ren, W., Li, Y., Gao, J., Yang, X., & Yao, J. (2020). Zeolitic Imidazolate Framework-67@Cellulose aerogel for rapid and efficient degradation of organic pollutants. *Journal of Solid State Chemistry, 291*, 121621. https://doi.org/10.1016/j.jssc.2020.121621
85. Malakootian, M., Nasiri, A., Asadipour, A., & Kargar, E. (2019). Facile and green synthesis of $ZnFe_2O_4$@CMC as a new magnetic nanophotocatalyst for ciprofloxacin degradation from aqueous media. *Process Safety and Environmental Protection, 129*, 138–151. https://doi.org/10.1016/j.psep.2019.06.022
86. Nasiri, A., Tamaddon, F., Mosslemin, M. H., Gharaghani, M. A., & Asadipour, A. (2019). New magnetic nanobiocomposite $CoFe_2O_4$@methycellulose: Facile synthesis, characterization, and photocatalytic degradation of metronidazole. *Journal of Materials Science: Materials in Electronics, 30*, 8595–8610. https://doi.org/10.1007/s10854-019-01182-7
87. Tamaddon, F., Mosslemin, M. H., Asadipour, A., Gharaghani, M. A., & Nasiri, A. (2020). Microwave-assisted preparation of $ZnFe_2O_4$@methyl cellulose as a new nano-biomagnetic photocatalyst for photodegradation of metronidazole. *International Journal of Biological Macromolecules, 154*, 1036–1049. https://doi.org/10.1016/j.ijbiomac.2020.03.069
88. Tamaddon, F., Nasiri, A., & Yazdanpanah, G. (2020). Photocatalytic degradation of ciprofloxacin using $CuFe_2O_4$@methyl

cellulose based magnetic nanobiocomposite. *MethodsX, 7*, 100764. https://doi.org/10.1016/j.mex.2019.12.005
89. Nasiri, A., Tamaddon, F., Mosslemin, M. H., & Faraji, M. (2019). A microwave assisted method to synthesize nano$CoFe_2O_4$@methyl cellulose as a novel metal–organic framework for antibiotic degradation. *MethodsX, 6*, 1557–1563. https://doi.org/10.1016/j.mex.2019.06.017
90. Fang, S., Lyu, X., Tong, T., Lim, A. I., Li, T., Bao, J., & Hu, Y. H. (2023). Turning dead leaves into an active multifunctional material as evaporator, photocatalyst, and bioplastic. *Nature Communications, 14*, 1203. https://doi.org/10.1038/s41467-023-36783-8
91. Ong, W.-J., Tan, L.-L., Ng, Y. H., Yong, S.-T., & Chai, S.-P. (2016). Graphitic carbon nitride (g-C_3N_4)-based photocatalysts for artificial photosynthesis and environmental remediation: Are we a step closer to achieving sustainability? *Chemical Reviews*. https://doi.org/10.1021/acs.chemrev.6b00075
92. Qamar, M. A., Javed, M., Shahid, S., Shariq, M., Fadhali, M. M., Ali, S. K., & MohdS, K. (2023). Synthesis and applications of graphitic carbon nitride (g-C_3N_4) based membranes for wastewater treatment: A critical review. *Heliyon, 9*, e12685. https://doi.org/10.1016/j.heliyon.2022.e12685
93. Zhang, X., Xie, X., Wang, H., Zhang, J., Pan, B., & Xie, Y. (2013). Enhanced photoresponsive ultrathin graphitic-phase C_3N_4 nanosheets for bioimaging. *Journal of the American Chemical Society, 135*, 18–21. https://doi.org/10.1021/ja308249k
94. Wen, J., Xie, J., Chen, X., & Li, X. (2017). A review on g-C_3N_4-based photocatalysts. *Applied Surface Science, 391*, 72–123. https://doi.org/10.1016/j.apsusc.2016.07.030
95. Ismael, M., & Wu, Y. (2019). A mini-review on the synthesis and structural modification of g-C_3N_4-based materials, and their applications in solar energy conversion and environmental remediation. *Sustainable Energy and Fuels, 3*, 2907–2925. https://doi.org/10.1039/C9SE00422J
96. Alhokbany, N. S., Mousa, R., Naushad, M., Alshehri, S. M., & Ahamad, T. (2020). Fabrication of Z-scheme photocatalysts g-C_3N_4/Ag_3PO_4/chitosan for the photocatalytic degradation of ciprofloxacin. *International Journal of Biological Macromolecules, 164*, 3864–3872. https://doi.org/10.1016/j.ijbiomac.2020.08.133
97. Qarajehdaghi, M., Mehrizad, A., Gharbani, P., & Shahverdizadeh, G. H. (2023). Quaternary composite of CdS/g-C_3N_4/rGO/CMC as a susceptible visible-light photocatalyst for effective abatement of ciprofloxacin: Optimization and modeling of the process by RSM and ANN. *Process Safety and Environmental Protection, 169*, 352–362. https://doi.org/10.1016/j.psep.2022.11.030
98. Faisal, M., Ahmed, J., Jalalah, M., Alsareii, S. A., Alsaiari, M., & Harraz, F. A. (2023). Rapid elimination of antibiotic gemifloxacin mesylate and methylene blue over Pt nanoparticles dispersed chitosan/g-C_3N_4 ternary visible light photocatalyst. *Environmental Science and Pollution Research, 30*, 61710–61725. https://doi.org/10.1007/s11356-023-26456-w
99. Wang, J., & Wei, J. (2022). Facile preparation of graphitic carbon nitride nanosheet/agar composite hydrogels for removal of tetracycline *via* the synergy of adsorption and photocatalysis. *New Journal of Chemistry, 46*, 6977–6985. https://doi.org/10.1039/D1NJ06227A
100. Zhou, S., Zhang, C., Xia, L., Fu, Z., Zhu, N., Gong, J., Wang, X., Lyu, P., Li, L., & Xu, W. (2022). A flexible and weavable lignocellulose-based photocatalyst supported by natural three-dimensional porous *Juncus effusus* for highly efficient degradation of environmental contaminants. *ACS Applied Materials and Interfaces, 14*, 27955–27967. https://doi.org/10.1021/acsami.2c06207
101. Huo, K., Wang, J., Zhuang, T., Zhao, Y., Gao, B., Dou, M., Wang, X., Fu, Y., Wang, D., & Ci, L. (2021). Facile fabrication of recyclable and macroscopic D-g-C_3N_4/sodium alginates/non-woven fabric immobilized photocatalysts with enhanced photocatalytic activity and antibacterial performance. *Journal of Materials Science, 56*, 17584–17600. https://doi.org/10.1007/s10853-021-06454-4
102. Pan, J., Hua, D., Hong, Y., Cheng, X., Guo, F., Bing Tan, K., Zhong, Z., & Zhan, G. (2023). Design of hybrid g-C_3N_4/GO/MCE photocatalytic membranes with enhanced separation performance under visible-light irradiation. *Chemical Engineering Journal, 466*, 143164. https://doi.org/10.1016/j.cej.2023.143164
103. Zhou, T., Zhao, L., Wu, D., Feng, Q., & Zhao, B. (2022). Uniformly assembled polypyrrole-covered bacterial cellulose/g-C_3N_4 flexible nanofiber membrane for catalytic degradation of tetracycline hydrochloride. *Journal of Water Process Engineering, 47*, 102775. https://doi.org/10.1016/j.jwpe.2022.102775
104. Joseph, C. G., Li Puma, G., Bono, A., & Krishnaiah, D. (2009). Sonophotocatalysis in advanced oxidation process: A short review. *Ultrasonics Sonochemistry, 16*, 583–589. https://doi.org/10.1016/j.ultsonch.2009.02.002
105. Gholami, P., Khataee, A., Vahid, B., Karimi, A., Golizadeh, M., & Ritala, M. (2020). Sonophotocatalytic degradation of sulfadiazine by integration of microfibrillated carboxymethyl cellulose with Zn–Cu–Mg mixed metal hydroxide/g-C_3N_4 composite. *Separation and Purification Technology, 245*, 116866. https://doi.org/10.1016/j.seppur.2020.116866
106. Piccirillo, G., Aroso, R. T., Rodrigues, F. M. S., Carrilho, R. M. B., Pinto, S. M. A., Calvete, M. J. F., & Pereira, M. M. (2021). Oxidative degradation of pharmaceuticals: The role of tetrapyrrole-based catalysts. *Catalysts, 11*, 1335. https://doi.org/10.3390/catal11111335
107. Ohtani, B. (2010). Photocatalysis A to Z—What we know and what we do not know in a scientific sense. *Journal of Photochemistry and Photobiology C: Photochemistry Reviews, 11*, 157–178. https://doi.org/10.1016/j.jphotochemrev.2011.02.001
108. Josefsen, L. B., & Boyle, R. W. (2012). Unique diagnostic and therapeutic roles of porphyrins and phthalocyanines in photodynamic therapy, imaging and theranostics. *Theranostics, 2*, 916–966. https://doi.org/10.7150/thno.4571
109. Maldonado-Carmona, N., Ouk, T.-S., & Leroy-Lhez, S. (2022). Latest trends on photodynamic disinfection of Gram-negative bacteria: Photosensitizer's structure and delivery systems. *Photochemical and Photobiological Sciences, 21*, 113–145. https://doi.org/10.1007/s43630-021-00128-5
110. Donohoe, C., Senge, M. O., Arnaut, L. G., & Gomes-da-Silva, L. C. (2019). Cell death in photodynamic therapy: From oxidative stress to anti-tumor immunity. *Biochimica et Biophysica Acta (BBA)—Reviews on Cancer, 1872*, 188308. https://doi.org/10.1016/j.bbcan.2019.07.003
111. Gierlich, P., Mata, A. I., Donohoe, C., Brito, R. M. M., Senge, M. O., & Gomes-da-Silva, L. C. (2020). Ligand-targeted delivery of photosensitizers for cancer treatment. *Molecules, 25*, 5317. https://doi.org/10.3390/molecules25225317
112. Gallardo-Villagrán, M., Leger, D. Y., Liagre, B., & Therrien, B. (2019). Photosensitizers used in the photodynamic therapy of rheumatoid arthritis. *International Journal of Molecular Sciences, 20*, 3339. https://doi.org/10.3390/ijms20133339
113. Pathak, P., Zarandi, M. A., Zhou, X., & Jayawickramarajah, J. (2021). Synthesis and applications of porphyrin-biomacromolecule conjugates. *Frontiers in Chemistry, 9*, 764137. https://doi.org/10.3389/fchem.2021.764137
114. Wang, C., Cai, M., Liu, Y., Yang, F., Zhang, H., Liu, J., & Li, S. (2022). Facile construction of novel organic–inorganic tetra (4-carboxyphenyl) porphyrin/Bi_2MoO_6 heterojunction for tetracycline degradation: Performance, degradation pathways, intermediate toxicity analysis and mechanism insight. *Journal*

of Colloid and Interface Science, 605, 727–740. https://doi.org/10.1016/j.jcis.2021.07.137
115. Wang, C., Yan, R., Cai, M., Liu, Y., & Li, S. (2023). A novel organic/inorganic S-scheme heterostructure of TCPP/$Bi1_2O17Cl2$ for boosting photodegradation of tetracycline hydrochloride: Kinetic, degradation mechanism, and toxic assessment. *Applied Surface Science, 610*, 155346. https://doi.org/10.1016/j.apsusc.2022.155346
116. Dumoulin, F., Durmuş, M., Ahsen, V., & Nyokong, T. (2010). Synthetic pathways to water-soluble phthalocyanines and close analogs. *Coordination Chemistry Reviews, 254*, 2792–2847. https://doi.org/10.1016/j.ccr.2010.05.002
117. Mgidlana, S., Openda, Y. I., & Nyokong, T. (2023). Asymmetrical zinc phthalocyanine conjugated to various nanomaterials for applications in phototransformation of organic pollutants and photoinactivation of bacteria. *Journal of Molecular Structure, 1277*, 134850. https://doi.org/10.1016/j.molstruc.2022.134850
118. Godard, J., Gibbons, D., Leroy-Lhez, S., Williams, R. M., Villandier, N., Ouk, T.-S., Brégier, F., & Sol, V. (2021). Development of phenalenone-triazolium salt derivatives for aPDT: Synthesis and antibacterial screening. *Antibiotics, 10*, 626. https://doi.org/10.3390/antibiotics10060626
119. Godard, J., Aimeur, M., Villandier, N., Zermane, F., Bregier, F., Sol, V., & Baudu, M. (2021). Photodegradation of tebuconazole mediated by a novel hybrid phenalenone based photosensitizer. *Journal of Photochemistry and Photobiology A: Chemistry, 408*, 113124. https://doi.org/10.1016/j.jphotochem.2020.113124
120. Aimeur, M., Godard, J., Baudu, M., Bregier, F., Villandier, N., & Zermane, F. (2021). Photodegradation of tebuconazole in a fluidized bed reactor mediated by phenalenone supported on sand. *Chemical Engineering Journal, 410*, 128332. https://doi.org/10.1016/j.cej.2020.128332
121. Amaly, N., EL-Moghazy, A. Y., Nitin, N., Sun, G., & Pandey, P. K. (2022). Synergistic adsorption-photocatalytic degradation of tetracycline by microcrystalline cellulose composite aerogel dopped with montmorillonite hosted methylene blue. *Chemical Engineering Journal, 430*, 133077. https://doi.org/10.1016/j.cej.2021.133077
122. Wu, Y., Lu, L., Zhang, Y., Yuan, Z., Yang, L., Wang, L., & Rao, Y. (2021). A bioinspired cercosporin/polymethylmethacrylate photocatalyst with high efficiency for decontamination of pharmaceuticals and pathogens. *Journal of Hazardous Materials, 419*, 126555. https://doi.org/10.1016/j.jhazmat.2021.126555
123. Singh, P., Sharma, P., Kaur, N., Mittal, L. S., & Kumar, K. (2020). Perylene diimides: Will they flourish as reaction-based probes? *Analytical Methods, 12*, 3560–3574. https://doi.org/10.1039/D0AY00966K
124. Zhang, Q., Jiang, L., Wang, J., Zhu, Y., Pu, Y., & Dai, W. (2020). Photocatalytic degradation of tetracycline antibiotics using three-dimensional network structure perylene diimide supramolecular organic photocatalyst under visible-light irradiation. *Applied Catalysis B: Environmental, 277*, 119122. https://doi.org/10.1016/j.apcatb.2020.119122

Authors and Affiliations

Nidia Maldonado-Carmona[1] · Giusi Piccirillo[2] · Jérémy Godard[4] · Karine Heuzé[3] · Emilie Genin[3] · Nicolas Villandier[4] · Mário J. F. Calvete[2] · Stéphanie Leroy-Lhez[4]

✉ Nidia Maldonado-Carmona
nidia.maldonado_carmona@sorbonne-universite.fr

✉ Stéphanie Leroy-Lhez
stephanie.lhez@unilim.fr

[1] Centre National de la Recherche Scientifique, Laboratoire Jean Perrin, Sorbonne Université, Paris, France

[2] Department of Chemistry, CQC-IMS, Rua Larga, University of Coimbra, 3004-535 Coimbra, Portugal

[3] Univ. Bordeaux, CNRS, Bordeaux INP, ISM, UMR 5255, 33400 Talence, France

[4] Univ. Limoges, LABCiS, UR 22722, 87000 Limoges, France